The Physical Oceanographic Processes on the Southeast African Shelf and Slope

Cristina Serena Russo
RSSCRI001

Supervisors: Dr Tarron Lamont
Prof. Isabelle Ansorge
Dr Ray Barlow

Submitted in fulfilment of the requirements for the degree of Master of Science (Physical Oceanography)

Department of Oceanography
Faculty of Science
University of Cape Town
Rondebosch
Cape Town
7701
August 2018

Plagiarism Declaration

I, Cristina Serena Russo, know that plagiarism is wrong. Plagiarism is to use another's work and pretend that it is one's own.

I have used the Harvard convention for citation and referencing. Each contribution to, and quotation in, this project from the work(s) of other people has been attributed, and has been cited and referenced.

This project is my own work.

I have not allowed, and will not allow, anyone to copy my work with the intention of passing it off as his or her own work.

Signature Signed by candidate

Date _____

Abstract

Situated between the southeast coast of South Africa and the western edge of the Agulhas Current, is the southeast African shelf. The Agulhas Current, like other western boundary currents of the world, strongly influences the oceanographic conditions of its adjacent shelf system. Limited societal drivers have resulted in the southeast African shelf being one of the least studied and under-sampled shelf systems in southern Africa. The *in situ* sample deficit has led to the majority of studies conducted in this region to be carried out using satellite data and modelling. In order to identify the physical oceanographic processes occurring on the southeast African shelf and slope, as well as the influence that the Agulhas Current has on them, this study analysed satellite data combined with high resolution *in situ* data, acquired during two hydrographic surveys of the southeast African shelf and slope, during January/February (austral summer) and July/August (austral winter) 2017. The Agulhas Current as well as a number of physical processes were observed to influence the shelf region. The snapshot of the two seasons given by the January/February and July/August *in situ* data presented indications of seasonality of temperature and salinity within the upper water masses but not within the deeper water masses. The same five water masses, Tropical Surface Water (TSW), Subtropical Surface Water (STSW), South Indian Central Water (SICW), Red Sea Water (RSW) as well as Antarctic Intermediate Water (AAIW), were observed during each cruise. As a result of the westward widening shelf from just east of East London, divergence-induced upwelling was observed between the coast and the inshore edge of the Agulhas Current, during both January/February and July/August. Ekman veering in the bottom boundary layer was observed between Port Alfred and East London during January/February as a result of the close proximity of the Agulhas Current to the slope. Altimetry data indicated the presence of a cyclonic eddy during both the January/February and July/August 2017 surveys. The presence of cold nutrient-rich SICW in the bottom layers on the shelf during January/February and July/August was as a result of the uplift caused by Ekman pumping associated with the cyclonic eddies. AAIW, usually observed along the offshore edge of the Agulhas Current, was found on the slope along the inshore edge of the Agulhas Current, as a result of the presence of cyclonic eddies. Wind-driven upwelling, induced by offshore Ekman transport and vertical mixing, resulted in the surfacing of cooler waters from below at several locations. Chlorophyll-a concentrations were found to be higher during January/February than during July/August 2017. The dissolved oxygen levels

observed on the shelf during both surveys were found to be in the range where the biological responses would be insignificant, suggesting that oxygen availability, on the southeast African shelf, adequately facilitates the survival of the existing shelf biology and that low oxygen conditions do not seem to impact the shelf. This study provides the description of the first high resolution shelf wide hydrographic surveys of the region, during the austral summer and winter (even though they are considered as snapshots) which sets a baseline of oceanographic conditions on the shelf as well as the processes affecting it. The results of this study can be used by the scientific community and governmental departments to better implement conservation regulations regarding marine protected areas in the region.

Acknowledgements

I would like to thank Tarron Lamont for her boundless guidance and infectious enthusiasm as well as for introducing me to the project, giving me the invaluable opportunity to go to sea twice and be immersed in the data collection and analysis process for this project. To Isabelle Ansorge for her valued counselling regarding the writing and style of this thesis. To Ray Barlow for his valued input regarding the shelf biology. To Marcel van den Berg for the collection and processing of the ADCP data. To Gavin Tutt, Mbulelo Makhetha and Leon Jacobs for the collection and processing of the CTD data. To Matthew Carr and Sheveenah Taukoor for their help with the collection of the nutrient samples during the two cruises. To Raymond Roman and Raquel Flynn for running the nutrient analysis using the Lachat Autoanalyzer. To Claudia and Mena Russo for their significant contribution to the manual nutrient analysis process. To Roberto Santana for showing me the efficient way of using excel. To my parents, Nino and Mena Russo, and to my Nonna, for their continued support, guidance and interest in my research. I would also like to express my gratitude towards the financial support given to me by the African Coelacanth Ecosystem Programme, the PHAKISA initiative and the Department of Environmental Affairs.

List of Figures

List of Tables

Abbreviations, Acronyms and Explanations

ADT	Absolute Dynamic Topography
ACEP	African Coelacanth Ecosystem Programme
AAIW	Antarctic Intermediate Water
AVISO	Archiving, Validation and Interpretation of Satellite Oceanographic data
BBL	Bottom Boundary Layer
CMA	Centre Multimissions Altimètre
chl-a	chlorophyll-a
CDW	Circumpolar Deep Water
CTW	Coastal-Trapped Wave
CTD	Conductivity, Temperature and Depth
CMEMS	Copernicus Marine Environment Monitoring Service
DEA	Department of Environmental Affairs
DO	Dissolved Oxygen
EAC	East Australian Current
ELD	Ekman Layer Depth
TEOS-10	International Thermodynamic Equation of Seawater 2010
KSL	Kinematic Steering Level
KZN	KwaZulu-Natal
MPA	Marine Protected Area
MATLAB®	Matrix Laboratory
MSS	Mean Sea Surface
N-NED	N-(1-Naphthyl)ethylenediamine
NCAR	National Centre for Atmospheric Research

NCEP	National Centres for Atmospheric Prediction
NADW	North Atlantic Deep Water
ODV	Ocean Data View
PAR	Photosynthetically Available Radiation
RSW	Red Sea Water
SSH	Sea Surface Height
SST	Sea Surface Temperature
S-ADCP	Shipboard-Acoustic Doppler Current Profiler
SBE	Sea-Bird Electronics
SLA	Sea Level Anomaly
STA	Short Term Averaged
SAWS	South African Weather Service
STSW	Subtropical Surface Water
TO	Temperature-Oxygen
TS	Temperature-Salinity
TSW	Tropical Surface Water
WBC	Western Boundary Current

Table of Contents

1. Introduction

1.1 Background

The physical oceanography of continental shelf systems, as well as their influencing factors varies considerably from region to region (Schaeffer and Roughan, 2015, Allen et al., 1983). In order to study the dynamics of shelf systems, Schumann (1981) suggested that certain factors be considered such as: deep ocean input, bottom topographical effects as well as potential meteorological forcing. The principal contributor to deep ocean input on the shelf systems is the shelf-adjacent current.

Shelf-adjacent currents have either some or a dominating influence on the physical oceanographic processes occurring on the shelf systems (Schaeffer et al., 2013, Allen et al., 1983, Beckley and van Ballegooyen, 1992). Some of the strongest and fastest flowing surface currents in the world are western boundary currents (WBCs) and studies have found that they significantly influence their adjacent shelf systems (Schaeffer and Roughan, 2015, Allen et al., 1983). The East Australian Current (EAC) is a WBC that exhibits this well. Studies focussing on the EAC, found that it and its associated eddy field dominate the circulation on the adjacent shelf (Schaeffer et al., 2013).

The Agulhas Current is the largest and strongest of all WBCs in the southern hemisphere (Roberts et al., 2010, Lutjeharms and Ansorge, 2001) and it is flanked, on its western edge, by the southeast African continental margin, which encompasses the continental shelf and slope. The southeast African shelf is located on the southeast coast of South Africa, between Cape St Francis and Durban (Ludwig et al., 1968) and comprises four of South Africa's thirteen coastal regions i.e. the Sunshine Coast, the Border Kei Coast, the Wild Coast and the Hibiscus Coast (see Figure 1.1). The Agulhas Current strongly influences the shelf waters where it hugs the shelf-break, which is as a result of a topographical steering and stabilising effect caused by the presence of a narrow continental shelf with a steep slope (Roberts et al., 2010). The Agulhas Current's influence on the shelf waters begins to diminish as it deviates from the coast southwest of the Kei River mouth, which is as a result of the breakdown of the steering and the stabilising effect caused by the gradual widening of continental shelf and flattening of the slope (Roberts et al., 2010). Being the largest and strongest WBC in the southern hemisphere, the influence that the Agulhas Current has on its adjacent continental shelf is of great interest.

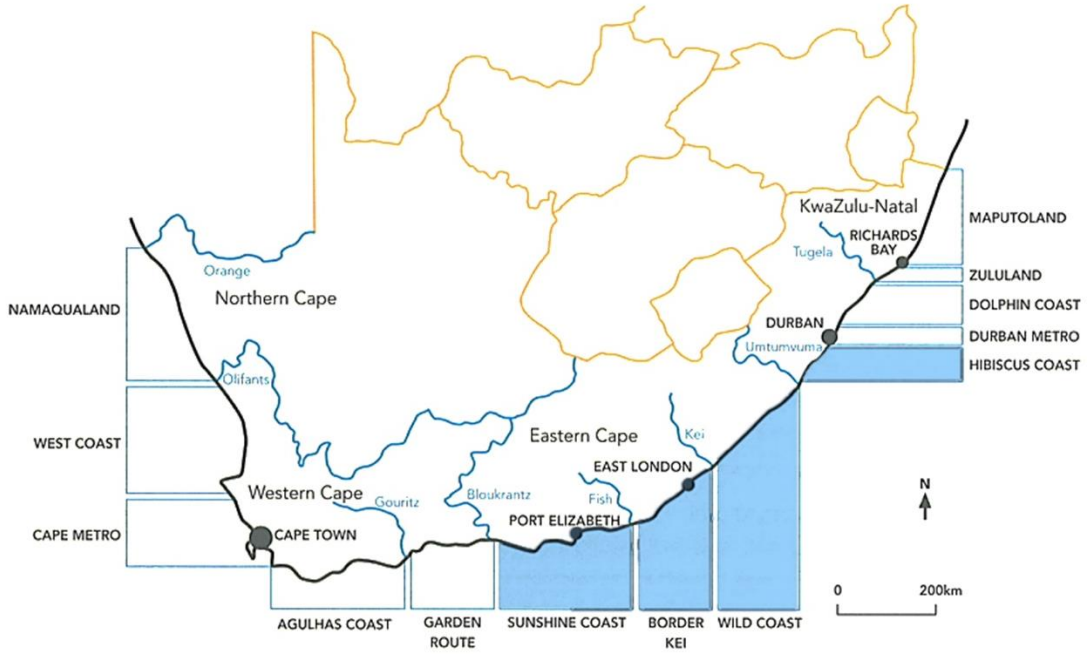

Figure 1.1 Map of South Africa's thirteen coastal regions adapted from CSIR and DEAT (2005), highlighting the four coastal regions encompass by the southeast African shelf.

As a result of limited societal drivers such as marine mining, industrial development and offshore fisheries, the southeast African shelf is one of the least studied and under-sampled shelf systems in southern Africa (Department of Environmental Affairs, 2017). The *in situ* sample-deficit has resulted in the majority of the research conducted in the area to have been carried out using satellite data and modelling (Rouault and Penven, 2011, Roberts et al., 2010, Lutjeharms et al., 2003). Few studies have used the limited available *in situ* data (Goschen et al., 2012, Roberts, 2010) and even fewer have used this data to investigate the physical processes occurring on the shelf and slope, as well as the impact of the Agulhas Current on the shelf and slope.

The southeast African shelf plays an underrated role in accommodating the annual sardine run, which sees the northward migration of sardines from the Agulhas Bank along the southeast African shelf to the sheltered KZN Bight (Lamont, 2017, van der Lingen et al., 2010, Roberts et al., 2010). The sardine run takes place during the austral winter (O'Donoghue et al., 2010) and has been found to coincide with relatively low sea surface temperatures (SSTs), as well as the presence of inshore counter currents which are associated with the passage of cyclonic eddies (Roberts et al., 2010). It has socio-economic importance, not only for fisheries but also for ecotourism (Lamont, 2017, van der Lingen et al., 2010). The southeast African shelf exists within

a mesotrophic environment thus the slightest perturbations can influence the nutrient availability and subsequent primary productivity of the shelf region (Lutjeharms et al., 2000a, Barlow et al., 2010). A better understanding of the physical oceanographic processes occurring on the shelf as well as their driving forces could not only have a positive influence on economic activity linked to both fisheries and ecotourism but it also could aid the scientific community and government departments, in the better implementation of conservation regulations regarding Marine Protected Areas (MPAs).

Since 1991, a range of MPAs have been established along the southeast coast of South Africa including Sardinia Bay, Bird Island, Amathole, Dwesa-Cwebe, Hluleka and Pondoland (see Figure 1.2a). Operation Phakisa, a fast results delivery programme implemented by the South African Government has proposed the implementation of a network of new MPAs, both additional and extensions of previously established MPAs, which includes the Addo MPA, the Amathole Expansion and Protea Banks which can be seen in Figure 1.2b (Zuma, 2014). Both the old and new MPAs seek to fulfil a conservational purpose in which marine habitats like reefs, mangroves and coastal wetlands, are protected. The implementation of these newly proposed MPAs will be both environmentally and economically beneficial as it will result in the creation of a large number of jobs in the marine industry (Fluharty et al., 2016). The implementation of these MPAs requires the establishment of an environmental conditions baseline in order to identify and understand the influences of the environment on the MPA regions. Hence this study seeks to use high resolution *in situ* data to identify and describe the physical processes occurring on the southeast African shelf.

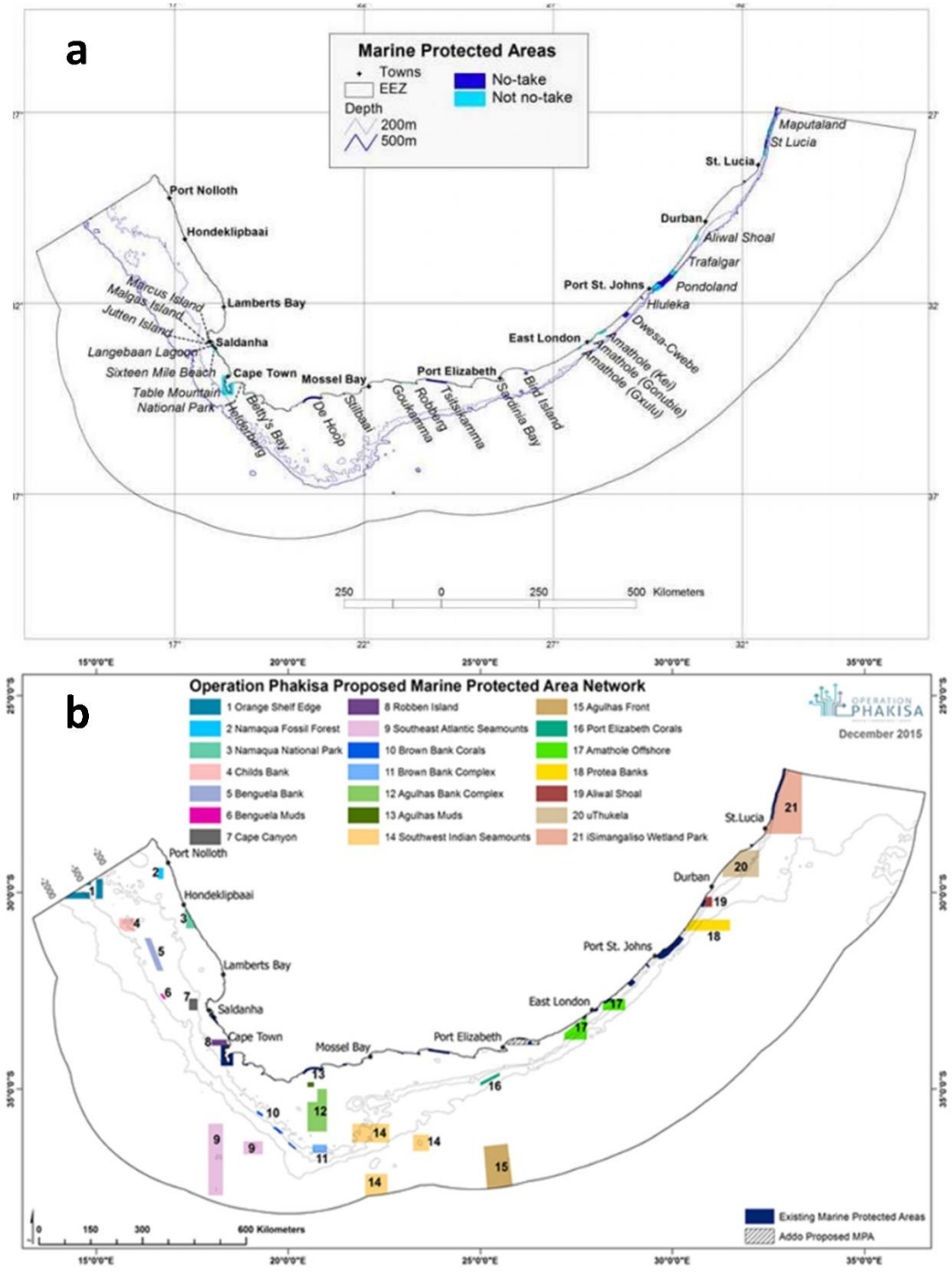

Figure 1.2 Maps of South Africa depicting a.) the existing marine protected areas after Sink et al. (2012) and b.) the Operation Phakisa proposed marine protected areas after Harris et al. (2014).

1.2 Rationale, Aim and Key Questions

Previous studies focussing on the physical oceanographic processes occurring on the southeast African shelf have either been bay-scale (Goschen et al., 2012, Roberts, 2010), which fail to identify the larger surrounding oceanographic features, or they have been too coarse resolution and large scale (Lutjeharms et al., 2010), which fail to identify the finer details of the circulation on the shelf. This study will therefore seek to identify the shelf-wide processes using high resolution hydrographic cruise data, ideally enabling the identification of both smaller and larger scale oceanographic features impacting the circulation on the shelf.

The aim of this thesis is to identify the physical oceanographic processes occurring on the southeast African shelf as well as investigate the influence that the Agulhas Current has on shelf and slope waters. In order to achieve this aim, a combination of satellite and *in situ* data collected during two hydrographic surveys of the region in 2017 were used to address the following key questions:

1. What are the physical oceanographic processes occurring in January/February and July/August 2017 on the southeast African shelf and slope and how do they differ?
2. How are the southeast African shelf and slope influenced by the adjacent Agulhas Current?
3. What water masses are present on the southeast African shelf and slope in January/February and July/August 2017 and what are their properties?

2. Literature Review

This study focusses on the southeast African shelf and slope which falls within the region of the Agulhas Current System. Although this study focusses on a particular area, it is important to take the broader surrounding region into account. In order to satisfy this study's aim, which seeks to identify the physical oceanographic processes occurring on the southeast African shelf and slope, as well as investigate the influence that the Agulhas Current has shelf and slope waters, this literature review therefore describes the oceanography of the Agulhas Current System as a whole, the local and synoptic weather patterns, as well as the local fluvial influence.

2.1 The Agulhas Current System

Western boundary currents (WBCs) are narrow, intense, persistent currents with shoreward sloping isopycnals on their landward-edge. They exist along the western boundary of the major ocean basins, forming the western limb of the wind-driven subtropical oceanic gyres (Imawaki et al., 2013, Lutjeharms, 2006a). The poleward flowing WBCs, which are induced by the zonally integrated wind stress curl of the adjacent basin, form to compensate for the equatorward flowing Sverdrup transport that takes place in the interior of the gyres (Imawaki et al., 2013, Lutjeharms, 2006a).

The Ekman pumping taking place within the Sverdrup interior of the gyres decreases the height of the water columns which, in order to conserve potential vorticity, move equatorward toward lower planetary vorticity. In order for the fluid to return to a higher latitude, relative vorticity is increased (Talley et al., 2011). This increase in relative vorticity takes place at the western boundary as a result of the friction imposed by the boundary on the fluid (Talley et al., 2011). The friction results in an offshore increase in velocity with a high horizontal shear. This horizontal shear results in the input of a high positive relative vorticity, which allows the planetary vorticity to change and the fluid to return to its original latitude (Talley et al., 2011). The shoreward inclination of the isopycnals in a western boundary current can be explained by the thermal wind equation which relates vertical gradients of velocity to horizontal gradients in density (Talley et al., 2011). As the geostrophic velocity weakens with depth, density increases and the isopycnals become tilted Talley et al., 2011). The Agulhas Current has a baroclinic structure such that it is a geostrophic flow with vertical sheer requiring sloping isopycnals.

The Agulhas Current, one of the world's major WBCs, forms the intensified western component of the wind-driven, anticyclonic subtropical south Indian Ocean gyre (Roberts et al., 2010, Lutjeharms, 2006a, Lutjeharms and Ansorge, 2001, Beckley and van Ballegooyen, 1992). The Agulhas Current encompasses the basic dynamical traits of WBCs (Lutjeharms, 2006a). Measuring the distance between the 0.5 ms^{-1} isotachs in the surface layers, the Current is between 70 and 100 km wide (Lutjeharms, 2006a). Its inshore edge, measuring in around 7 km wide, is defined by relatively high horizontal temperature (1°C/km) and velocity gradients at the surface (Lutjeharms, 2006a). It extends to a depth of approximately 2000 m, with its core velocity ranging between 1.4 $m.s^{-1}$ and 1.6 $m.s^{-1}$ (Lutjeharms and Ansorge, 2001). It is therefore estimated that the Agulhas Current has a net volume transport of approximately 70 Sv – making it the largest and strongest of the five major western boundary currents (WBCs) in the world (Roberts et al., 2010, Lutjeharms, 2006a, Bryden et al., 2005b). Unlike other WBCs, some of the Agulhas Current features are unique, such as: one of its source flows is interrupted by a land mass; it upstream flow component is stabilised by the adjacent shelf topography; and the limited poleward extent of the African continent allows for the flow of warm salty Agulhas water into the South Atlantic Ocean (Lutjeharms, 2006a, Morris et al., 2017), all of which is discussed below.

With waters originating from three major disparate source regions, depicted in Figure 2.1, the Agulhas Current establishes itself at approximately 27 °S and flows south to approximately 40 °S (Beal et al., 2006, Lutjeharms, 2006a, Gordon, 1985). These disparate source regions contributing to the overall flow, include the flow from the Mozambique Channel in the form of Mozambique Channel Eddies (~13%), the East Madagascar Current (~30%) and the re-circulation within the South West Indian Ocean sub-gyre (~57%) (Lutjeharms, 2006a, Beal et al., 2011).

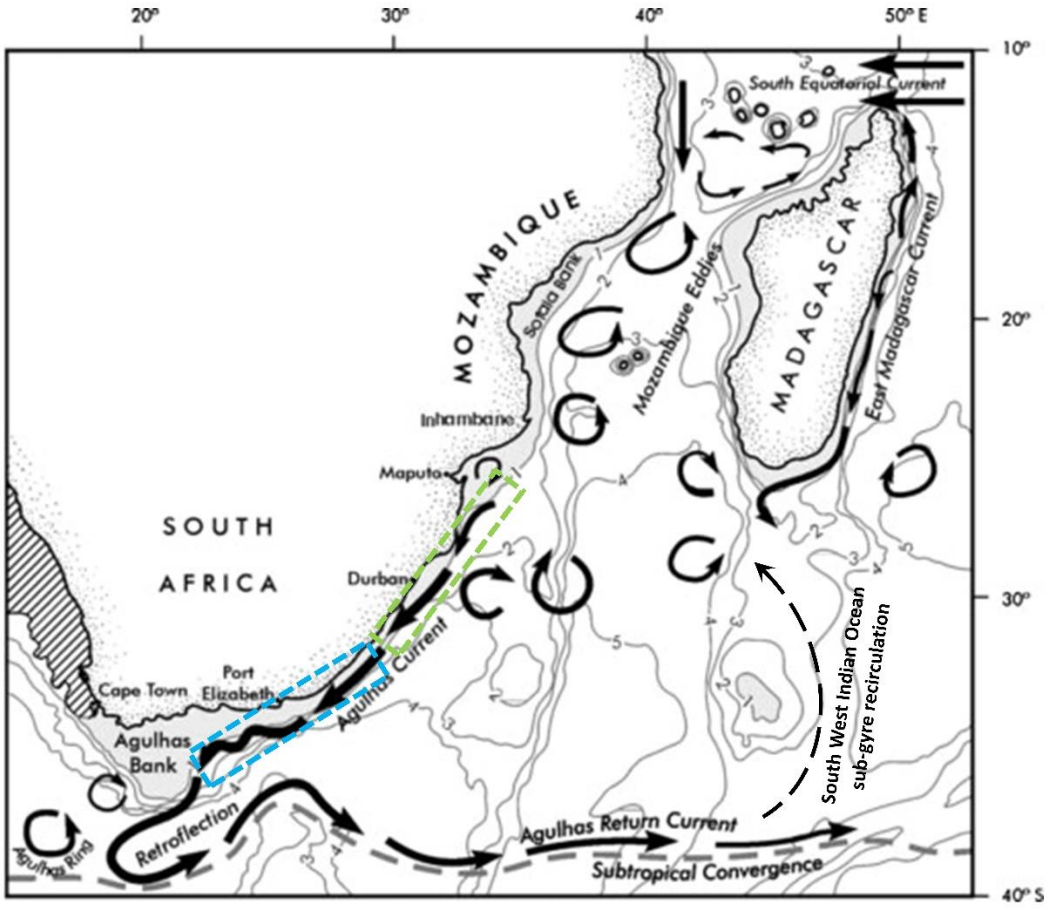

Figure 2.1 Schematic representation of the Agulhas Current System, adapted from (Lutjeharms, 2006b), illustrating the Agulhas Current's source regions and components, highlighting the Northern Agulhas Current (green) and the Southern Agulhas Current (blue).

The flow from the Mozambique Channel (Figure 2.1) has an intermittent contribution toward the overall flow of the Agulhas Current (Sætre and Da Silva, 1984). This intermittent flow occurs due to the passage of anticyclonic and cyclonic eddies through the Mozambique Channel, seen in Figure 2.1, which effectively transport tropical and subtropical surface waters as well as intermediate waters poleward (Lutjeharms, 2006a, Sætre and Da Silva, 1984). The East Madagascar Current, identified in Figure 2.1, also contributes toward the Agulhas Current's overall flow in the form of eddies and dipoles which either form due to the retroflection of the East Madagascar Current south of Madagascar or are generated further east and pass through the region (Schouten et al., 2002, Beal et al., 2011). Not only does the East Madagascar Current contribute to the overall flow in the form of eddies, it also encompasses the input from the general westward flow of the South Indian subtropical gyre (Lutjeharms, 2006a, Beal et al., 2011). The South West Indian Ocean sub-gyre, depicted in Figure 2.1, is located over the Agulhas Basin, west of 45 °E (Lutjeharms,

2006a). The recirculation within this sub-gyre is known to be the greatest contributor toward the Agulhas Current's overall flow which it continuously feeds along the Agulhas Current's entirety (Lutjeharms, 2006a).

Three components exist within the Agulhas Current System and these are the Agulhas Current, the Agulhas Retroflection and the Agulhas Return Current which can be seen in Figure 2.1. The first mentioned, Agulhas Current, is further partitioned into two components, i.e. the Northern Agulhas Current and the Southern Agulhas Current (Figure 2.1), due to differing shelf configurations and subsequently distinctively differing kinematics within each region (Lutjeharms, 2006a).

2.1.1 The Northern Agulhas Current

The Northern Agulhas Current, latitudinally bounded between 27 ^{o}S and 34 ^{o}S (Figure 2.1), constitutes the upstream component of the Agulhas Current, where surface temperatures exceed 22 °C (Lutjeharms, 2006a, Gründlingh, 1980, Lutjeharms, 2007). It is in the Northern Agulhas Current where a nearshore flowing current core has been observed with maximum velocities of 1.5 $m.s^{-1}$ (Rouault et al., 2010, Bryden et al., 2005a, van der Vaart and de Ruijter, 2001), and a volume flux of 69.7±4.3 Sv (Lutjeharms, 2007). Previous studies focussing on the seasonality of the Agulhas Current, presented opposing results with model simulations suggesting strongest transports during austral winter-spring (Matano et al., 2002) and observations suggesting strongest flows during austral summer (Krug and Tournadre, 2012). These contradictory findings suggest that a distinct seasonality in the current speeds and volume transport of the Agulhas Current is yet to be found (Lutjeharms, 2006a, Beal et al., 2015).

The defining factor allowing for the distinction of the Northern Agulhas Current from the Southern Agulhas Current (seen in Figure 2.1) is its exceptionally stable trajectory (Lutjeharms, 2006a). This stability is as a result of a steering and stabilizing effect which exists due to the presence of the steep continental slope topography as can be seen in Figure 2.2 (Roberts et al., 2010). It is this steering and stabilizing effect which results in the Agulhas Current being relatively more stable than other WBCs such as the Kuroshio Current and the Gulf Stream (Roberts, 2010, Lutjeharms, 2006a, de Ruijter et al., 1999).

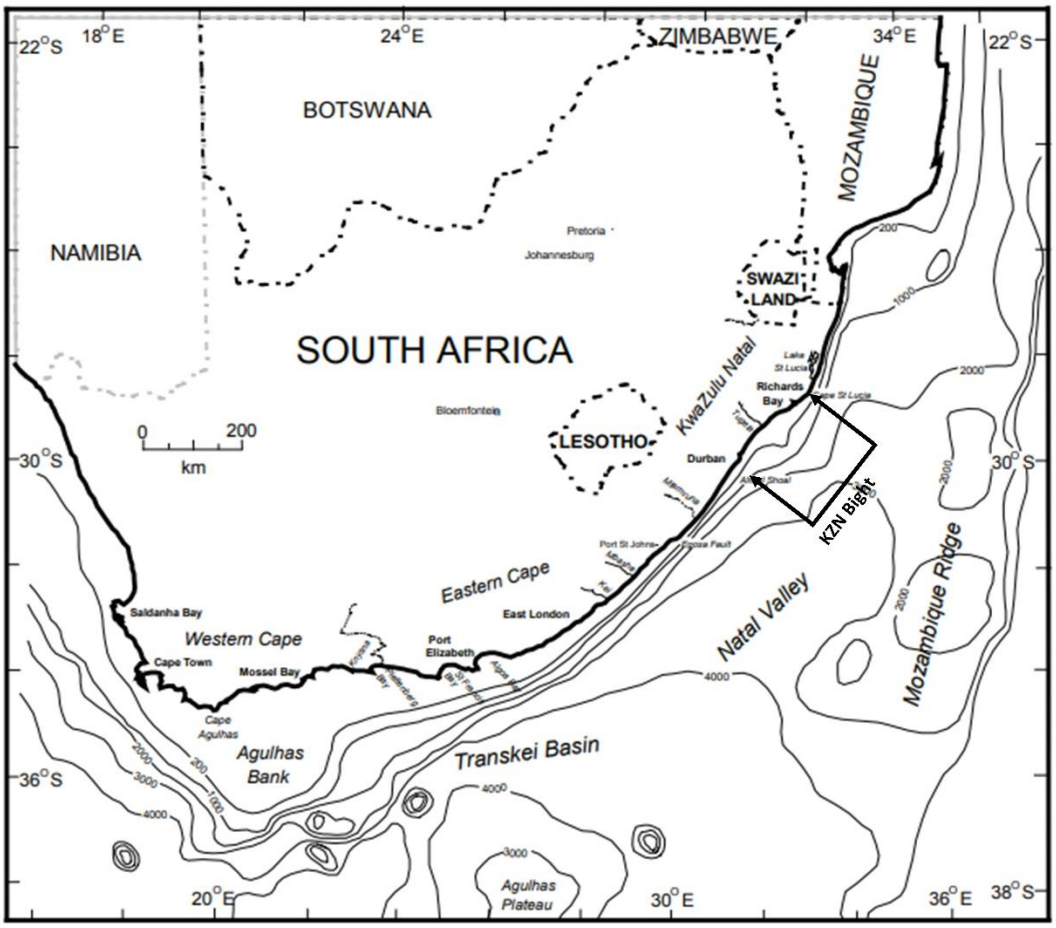

Figure 2.2 Bathymetric diagram, adapted from ASCLME (2012), illustrating the changing bathymetry along the southeast African shelf and highlighting the KZN Bight, between Cape St Lucia and Durban.

The continental shelf, flanking the Northern Agulhas Current on its western edge, is not uniform as can be seen in Figure 2.2. The majority (75%) of this continental shelf, between 27 ºS and 34 ºS, is narrow (~15 km in width) and has a steep continental slope. The direction of flow over the narrow shelf emulates that of the Northern Agulhas Current flanking it, in that it is south-westward (Lutjeharms, 2006a). The remaining 25% of the shelf is substantially wider and has been named the KwaZulu-Natal (KZN) Bight. It is near Cape St Lucia, at approximately 28.4 ºS, where the shelf begins to widen reaching a width of 40 km which thereafter begins to narrow towards Durban (~29.9 ºS), where the shelf measures 7 km in width (see Figure 2.2) (Roberts et al., 2010). The circulation on the shelf at the KZN Bight is cyclonic which is contrastingly different to that on the narrow shelf which mimics the Agulhas Current's direction of flow. That being said, the KZN Bight is known as the source region of Natal Pulses which are further discussed in section 2.3 (Lutjeharms, 2006a).

The stability of the Northern Agulhas Current is interrupted at sporadic instances by meanders known as Natal Pulses (Heileman et al., 2008). The recurring passage of these Natal Pulses is yet another feature characteristic to the Northern Agulhas Current (Lutjeharms, 2006a). A subsurface bight that exists near Durban is known as an area of cyclogenesis in which the lee-trapped cyclonic Durban Eddy forms (further discussed in section 2.3) (Roberts et al., 2010). Roberts et al. (2010) found that the presence of Natal Pulses and Durban Eddies was associated with inshore current reversals, in which a north-eastward current takes precedence over the generally present southwestwardly flowing current. Roberts et al. (2010) noted that these aforementioned features and their associated counter currents aid the northward migration of during the annual sardine run.

2.1.2 The Southern Agulhas Current

Near Port St John's at 31.62 ^{o}S (see Figure 2.2), the continental shelf begins to gradually widen in a south-westward direction, where it initially forms the southeast African shelf and ultimately forms the Agulhas Bank (Roberts et al., 2010). For the greater part, the shelf break throughout the east coast is shallow (50 m; see Figure 2.2). South of Cape St Lucia, the shelf break begins to gradually deepen and becomes defined by the 100 m depth contour until Port Alfred and thereafter by the 200 m contour (Roberts et al., 2010). The deepening shelf break, results in the existence of a more gradual continental slope which no longer has a stabilising effect on the path of the Agulhas Current (Lutjeharms, 2006a). The Southern Agulhas Current begins just south of the region where the shelf break deepens (Figure 2.1). This downstream component of the Agulhas Current has been found to have surface speeds in excess of 2 $m.s^{-1}$ with a volume flux of 126 Sv which is contrastingly larger to that of the Northern Agulhas Current (Lutjeharms, 2007). Similar to the Northern Agulhas Current, no apparent seasonal variations with regards to the current speeds and volume transport have been found to exist in the Southern Agulhas Current (Lutjeharms, 2006a, Beal et al., 2015).

As can be seen in Figure 2.1, the northern boundary of the Southern Agulhas Current is located at 34 ^{o}S, just west of Algoa Bay and terminates at the start of the Agulhas Retroflection, located between 16 ^{o}E and 20 ^{o}E (Lutjeharms, 2006a, Lutjeharms and van Ballegooyen, 1988). The greater variability in the location of the Southern Agulhas Current's path can be attributed to the presence and passage of increasingly larger meanders known as Natal Pulses (Lutjeharms, 2006a). These Natal Pulses not only result in the offshore relocation of the Southern Agulhas Current's path but are also

responsible for the presence of cyclonic motions over the shelf which like in the Northern Agulhas Current result in inshore current reversals (Rouault et al., 2010, Lutjeharms, 2006a, Schumann, 1986).

As the Southern Agulhas Current approaches the Agulhas Bank, the behaviour of its inshore edge begins to change. Lutjeharms (2006a) stated that here extensive meandering, the growth of shear-edge eddies (Lutjeharms et al., 1989b) as well as the trailing of long plumes of warm water occurs (Schumann and van Heerden, 1988). Rouault et al. (2010) found that the presence of these meanders and shear-edge eddies along the inshore edge of the current, induces upwelling and through the input of warm water in the upper layers, intensifies the thermocline on the Agulhas Bank. Surface temperatures of the Southern Agulhas Current have been found to range between 23-26 ^{o}C with a general surface salinity of 35.4 psu (Gordon et al., 1987). In comparison to its northern counterpart, the influence that the Southern Agulhas Current has on the shelf and coastal waters is very limited (Schumann, 1999).

2.1.3 The Agulhas Retroflection

After flowing past the Agulhas Bank (Figure 2.1), between 16 and 20 ^{o}E (Lutjeharms and van Ballegooyen, 1988), the Agulhas Current undergoes a direction change where it is more or less reversed and redirected towards the South Indian Ocean via the Agulhas Return Current which is further discussed in section 2.1.4 (Heileman et al., 2008). This consistent circulation feature known as the Agulhas Retroflection (Figure 2.1), is unique to the Agulhas Current in that it is located at the meridional extremity of the African continent and occurs on the border between two subtropical oceanic gyres (Lutjeharms, 2006a, Lutjeharms and Ansorge, 2001, Duncombe Rae, 1991). Here an inter-ocean exchange of water, energy as well as biota, occurs in the form of a major leakage from the Indian Ocean to the Atlantic Ocean (Beal et al., 2011, Heileman et al., 2008). This leakage consists of the detachment and drifting of surface water plumes, known as Agulhas filaments, from the Agulhas Current into the Benguela Current, as well as the shedding of eddies, known as Agulhas Rings (Figure 2.1), spawned at the Retroflection which move into the Atlantic Ocean (Lutjeharms, 2006a).

2.1.4 The Agulhas Return Current

The Agulhas Return Current consists of the eastward flowing Agulhas Current water after it has encountered the Agulhas Retroflection (Lutjeharms, 2006a, Lutjeharms

and Ansorge, 2001). As depicted in Figure 2.1, the Agulhas Return Current establishes itself east of the retroflection region, between 16 ºE and 20 ºE, and terminates between 66 ºS and 70 ºS (Lutjeharms and Ansorge, 2001). Its central location, between two oceanic gyres, results in the Agulhas Return Current linking the Atlantic Ocean, the Indian Ocean and the Southern Ocean and thus it forms part of the inter-ocean exchange (Lutjeharms and Ansorge, 2001).

2.2 Water Masses of the Agulhas Current

The water column in the world ocean comprises of different water masses. These water masses form due to climatic differences in their respective region of origin. The International Thermodynamic Equation of Seawater 2010 (TEOS-10) defines density as a function of conservative temperature, absolute salinity and sea pressure (McDougall et al., 2009). These three components, which gain their properties at their region of origin, dictate the position of water masses within the vertical structure of the water column (Bryan and Lewis, 1979). Many water masses have been identified within the water column of the Western Indian Ocean but five have been found to dominate in the Agulhas Current region. Lutjeharms (2006a) illustrates these five water masses on the Temperature-Salinity plots represented in Figure 2.3a-b.

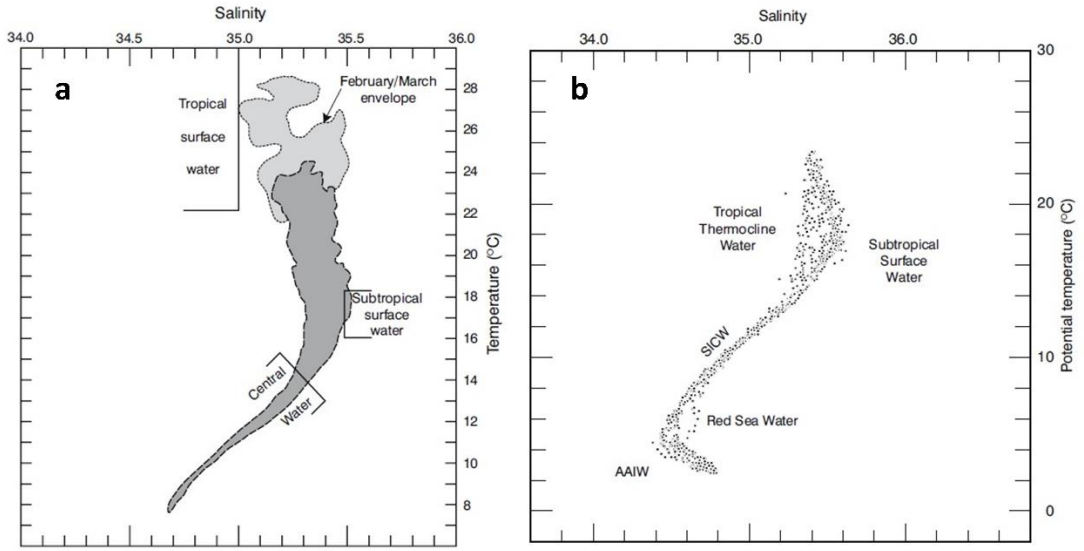

Figure 2.3 Temperature-Salinity (TS) diagram, after Lutjeharms (2006a), depicting the water masses of the Agulhas Current. a.) Envelope of 3600 measurements taken 100 km off of Durban from 1972 to 1974. b.) Measurements 450 km offshore between Durban and East London.

The upper waters of the water column within the Agulhas Current system comprise of three water masses. The upper 200 m of the water column within the Agulhas Current

system is occupied by Tropical Surface Water (TSW) and Subtropical Surface Water (STSW), both of which have their origins in the Indian Ocean (Lutjeharms, 2006a, Lutjeharms and Ansorge, 2001, Schumann, 1998) as illustrated in Figure 2.4. Due to density differences, TSW (Figure 2.3a), with a RSW <25.5 kg.m^{-3}, is located above the STSW (Figure 2.3a) which has a neutral density range of 25.5-26.4 kg.m^{-3} (see Table 2.1). The inflow of fresh water from the Pacific Ocean, as well as the surplus of precipitation over evaporation in the tropics (Figure 2.4), causes TSW to have a relatively low salt content, giving it a relatively low neutral density (Lutjeharms and Ansorge, 2001). Conversely, STSW has a higher neutral density because of its considerably higher salt content caused by the surplus of evaporation over precipitation within the anticyclonic subtropical south Indian Ocean gyre where it is formed, as represented in Figure 2.4 (Lutjeharms and Ansorge, 2001). South Indian Central Water (SICW), (Figure 2.3a-b), located beneath the TSW and STSW at 400 m and extends to a depth of 800 m (Schumann, 1998, Lutjeharms, 2006a) is formed by sinking in the subtropical convergence and falls within the neutral density range of 26.4-27.0 kg.m^{-3} (see Table 2.1).

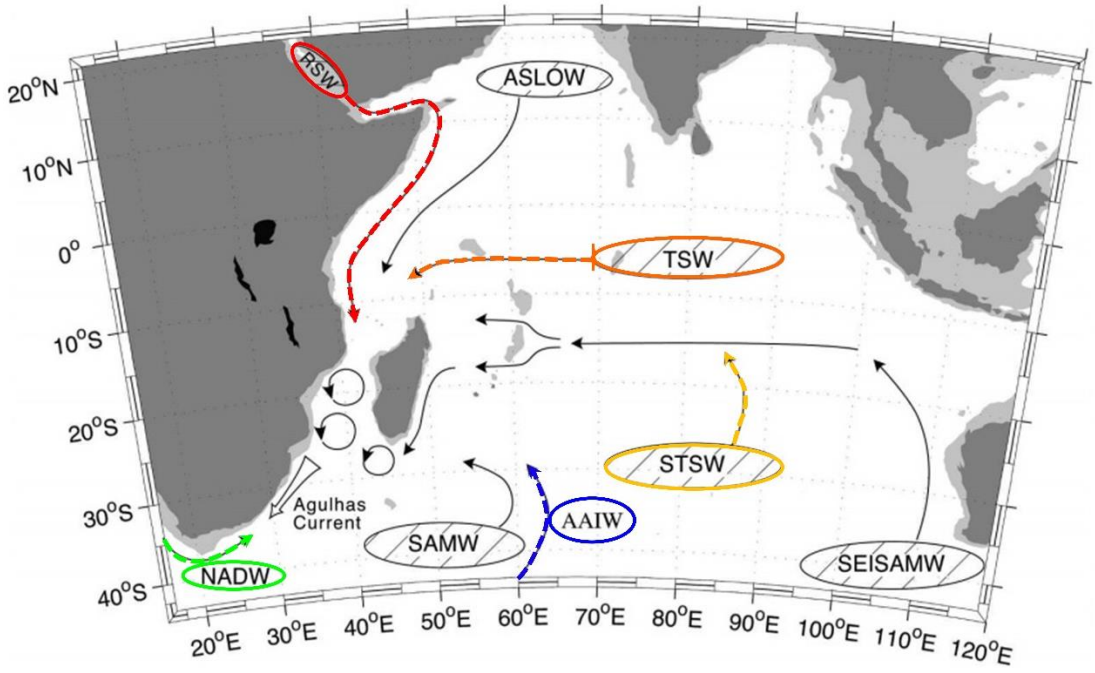

Figure 2.4 Schematic, adapted from Beal et al. (2006), highlighting the source regions and pathways of five water masses that are present in the Agulhas Current. Tropical Surface Water (TSW), Subtropical Surface Water (STSW), Red Sea Water (RSW), Antarctic Intermediate Water (AAIW) and North Atlantic Deep Water (NADW). Filled-in circles represent source regions within the Indian Ocean and empty circles represent source regions outside of the Indian Ocean.

The intermediate waters comprise of two water masses. Antarctic Intermediate Water (AAIW), is situated below the SICW at approximately 1200 m, with a neutral density range between 27.0-27.92 kg.m^{-3} (Figure 2.3b). It is formed in the Southern Ocean and enters the Agulhas Current system through the anticyclonic circulation of the southwest Indian Ocean sub-gyre (Figure 2.4) and is generally found along the seaward edge of the Agulhas Current (Lutjeharms and Ansorge, 2001, Emery and Meincke, 1986, Beal et al., 2006). Like AAIW, Red Sea Water (RSW) is occasionally found at similar depths with the same neutral density range measuring between 27.0-27.92 kg.m^{-3} (Figure 2.3b). Annually, a mean volume of 0.37 SV of RSW overflows into the Gulf of Aden and makes its way south-westward where it eventually enters the Agulhas Current system, through the Mozambique Channel (Figure 2.4), forming part of the intermediate layer along the inshore edge of the Agulhas Current (Beal et al., 2000, Lutjeharms, 2006a, Beal et al., 2006).

The deep waters comprise of two water masses – North Atlantic Deep Water (NADW) and the Circumpolar Deep Water (CDW) (Lutjeharms, 2006a, Emery and Meincke, 1986). NADW, with a neutral density of greater than 28.08 kg.m^{-3}, is located below both AAIW and RSW, while CDW, with a higher neutral density, is located below the NADW.

Table 2.1 Water masses and their respective temperature, salinity, neutral density ranges acquired from Lutjeharms (2006a), Beal et al. (2006), Lutjeharms et al. (1996) and Emery and Meincke (1986).

Water Mass Abbreviation	Temperature (°C)	Salinity (PSU)	Sources for temperature and salinity ranges	Neutral Density (kg.m^{-3}) from Beal et al. (2006)
TSW	22.00-28.00	< 35.55	Lutjeharms (2006a) and Beal et al. (2006)	<25.50
STSW	16.00-22.00	>35.55	Lutjeharms et al. (1996) and Beal et al. (2006)	25.50-26.40
SICW	6.00-14.00	34.60-35.8	Lutjeharms (2006a) and Emery and Meincke (1986)	26.40-27.00
AAIW	4.00-6.00	<34.60	Lutjeharms (2006a)	27.00-27.92
RSW	5.00-14.00	33.80-35.40	Emery and Meincke (1986)	27.00-27.92

NADW	1.50-4.00	34.80-35.00	Emery and Meincke (1986)	>28.08
CDW	1.00-2.00	34.62-34.73	Emery and Meincke (1986)	

While the water masses typically located in the water column, along the southeast African shelf, are regional in nature and thus are expected to remain similar irrespective of the season, their properties are likely to exhibit seasonality, either as a result of seasonal variations occurring in the formation region or as a result of local seasonal forcing, particularly in the upper water masses (Lamont et al., 2016, Pearce, 1977). Seasonal differences in the temperature and salinity ranges of the upper water masses have been observed by Lamont et al. (2016) and Pearce (1978) such that relatively higher temperatures and lower salinities exist during austral summer as opposed to those in the austral winter.

2.3 Upwelling and Agulhas Current Meanders

In a mesotrophic environment, like that of the southeast African shelf, upwelling events are important and have been found to have a profound effect on nutrient availability and the subsequent primary production of the region (Lutjeharms et al., 2000a). There are a number of processes that take place along the southeast African shelf which are responsible for bringing cold deep water up onto the shelf (Goschen et al., 2012). These processes essentially prime the lower levels of the continental shelf for upwelling events because this non-shelf cold water which gets brought up onto the shelf usually does not break the surface (Leber et al., 2017). The presence and passage of Natal Pulses and Durban Eddies, which are associated with Ekman pumping, as well as shelf-edge upwelling, induced by Ekman veering in the bottom boundary layer, are examples of such processes that cause the uplift and advection of cold deep nutrient-rich non-shelf waters onto the shelf (Roberts et al., 2006, Bakun, 2017, Goschen et al., 2012).

Although the Northern Agulhas Current is known for its stability, there are irregular and spasmodic perturbations that increase the variability of its trajectory (Leber and Beal, 2014, Lutjeharms, 2006a). These perturbations include the formation and passage of solitary meanders which alter the Agulhas Current's flow (Goble et al., 2014). These meanders are as a result of the formation and shedding of either, the larger Natal Pulse, or smaller Durban Eddy.

The Natal Pulse, exists as a pair of eddies which consists of an inshore cyclone and offshore anticyclone (Leber and Beal, 2014). The KZN Bight is an area where the continental shelf is noticeably wider (Figure 2.2 and Figure 2.5) and is believed to be the source region of these Natal Pulses (Lutjeharms and Roberts, 1988). These Natal Pulses are topographically induced, coastally trapped cyclonic lee eddies which have escaped from the KZN Bight due to the process of vortex shedding (Lutjeharms and Roberts, 1988). Another process found to compliment the formation of Natal Pulses is the absorption of deep-sea eddies on the seaward edge of the Agulhas Current (de Ruijter et al., 1999, Lutjeharms and Roberts, 1988). Ultimately, the meander that forms, results in the offshore relocation of both the Northern and Southern Agulhas Current's paths (Lutjeharms and Roberts, 1988). These meanders can affect the circulation on the adjacent shelf (Lutjeharms et al., 1989b), modify the coastal rainfall patterns (Lutjeharms and De Ruijter, 1996), cause the early retroflection of the Agulhas Current (Lutjeharms and van Ballegooyen, 1988), as well as promote shedding of Agulhas rings (Leeuwen et al., 2000).

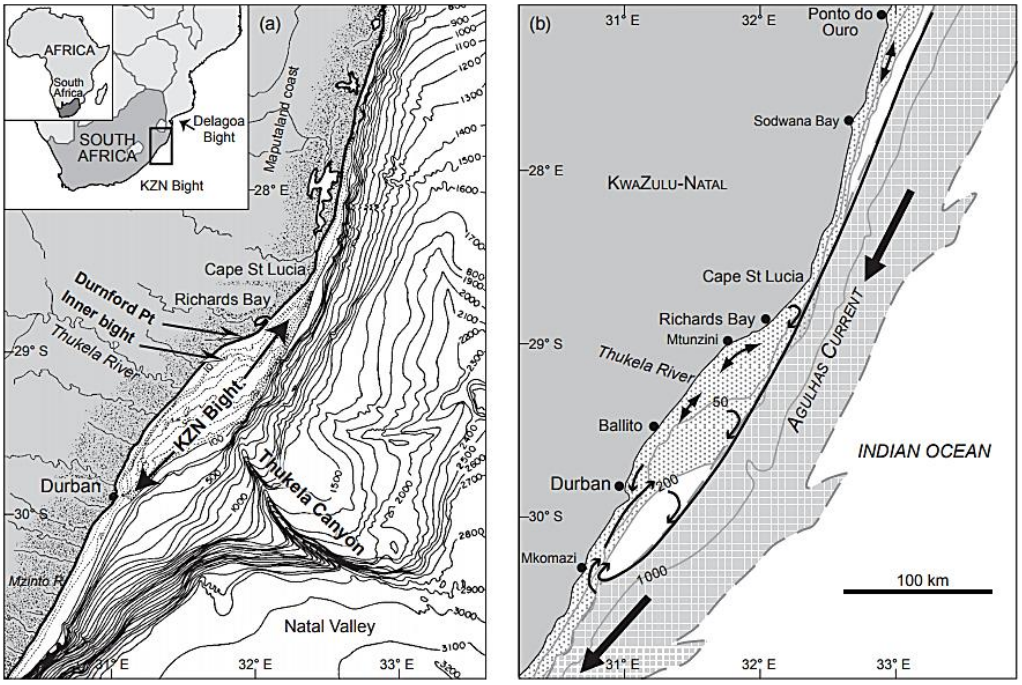

Figure 2.5 Schematic from Roberts et al. (2016) depicting (a) the bathymetry of the KZN Bight and (b) the circulation patterns within the KZN Bight.

These cyclonic eddies move downstream along the shoreward boundary of the Agulhas Current at a speed between 10-20 km.day^{-1} (de Ruijter et al., 1999, Lutjeharms and Roberts, 1988). Initially, near the KZN Bight, the cyclonic eddies are approximately 30 km wide but as they move downstream they grow, sometimes reaching widths of 200 km (Tsugawa and Hasumi, 2010, de Ruijter et al., 1999). On

average, they occur 4 to 6 times per year (Lutjeharms, 2006a), with a more recent study indicating that they occur 1.6 times a year (Rouault and Penven, 2011), with erratic intervals between pulses varying between 50 to 240 days (de Ruijter et al., 1999).

Studies have found that with the downstream advancement of the inshore cyclonic eddy, intermittent and temporary counter-currents form on their coastal edge (Lutjeharms and Roberts, 1988, Schumann, 1981) which have been proposed to assist the sardine in their annual northward migration along the southeast African shelf against the general flow of the Agulhas Current (Roberts et al., 2010). Leber and Beal (2014) found the Eulerian transport of the Agulhas current to decrease, with the development of these inshore counter-currents. The total transport of the Agulhas Current, however, is conserved due to the compensating effects of the broadening and weakening of the Agulhas Current's core (Leber and Beal, 2014).

The characteristics of cyclonic eddies are retained as long as there is an approximate balance among the dynamic forces that are involved (Bakun, 2006). The Coriolis and centrifugal forces, which are directed radially outward, are in balance with the pressure gradient force, which is directed inward toward the local 'low' pressure at the centre of the eddy (Bakun, 2006). The resultant surface divergence at the centre of the cyclonic eddy leads to the upward doming of the pycnocline and the thermocline (Figure 2.6a) (Bakun, 2006, Talley et al., 2011), which draws cold nutrient-rich water upward and facilitates enhanced primary production, seen in Figure 2.6a (Goble et al., 2014, Krug et al., 2014, Gaube et al., 2015).

Cyclonic eddies embedded with the meanders of the Brazil Current have been found to have a similar influence on the water column as that of Natal Pulses of the Agulhas Current (Campos et al., 2000). The interaction between a Natal Pulse and the shelf could result in decreased water temperatures over the shelf, which suggests the shoreward advection of the cold upwelled nutrient-rich water (Krug et al., 2014). In addition, other studies have found that the passage of these Natal Pulses is responsible for existence of central water on the shelf (Pivan et al., 2016).

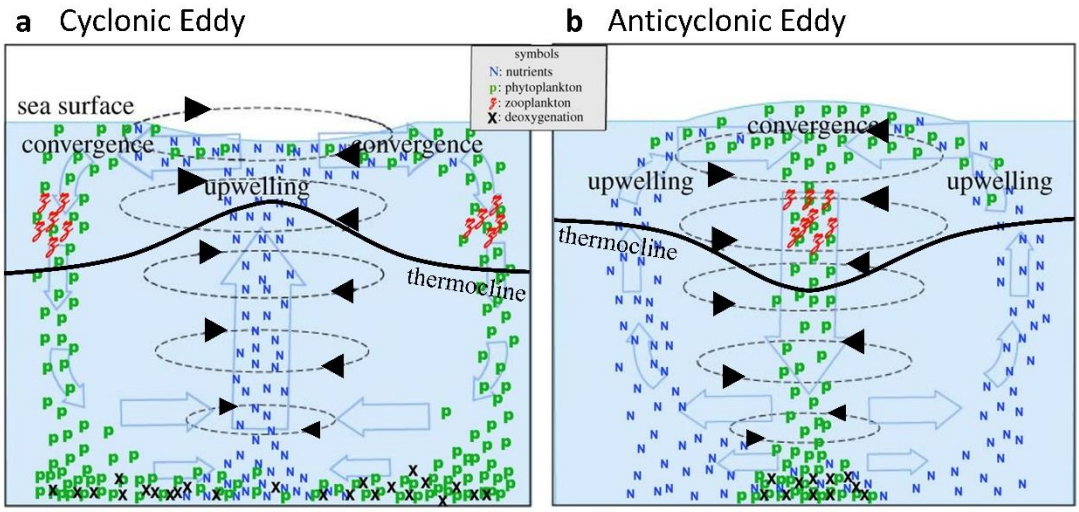

Figure 2.6 Schematic representation of the biological and physical mechanisms acting within eddies adapted from Bakun (2017) for the context of the southern hemisphere. a.) Cyclonic eddy, associated with the uplift of the thermocline and nutrients at the core. b.) Anticyclonic eddy associated with a deepening of the thermocline.

Unlike the Natal Pulse, the smaller cyclonic Durban Eddy is formed in the southern region of the KZN Bight due to the interaction of the Agulhas Current with the subsurface bight (Figure 2.5a) (Roberts et al., 2016, Roberts et al., 2010, Lutjeharms et al., 2000b). Like the Natal Pulse, the cyclonic circulation of the Durban Eddy gives rise to a semi-permanent, north-eastward flowing, counter-current located along the coast of Durban as can be seen in Figure 2.5b (Roberts et al., 2010). Durban Eddies have been found to shed approximately every 15 days and dissipate as they move downstream in a south-westward direction (Goble et al., 2014, Roberts et al., 2010).

Once detached from the Durban area, these eddies do not grow in a seaward scope but rather begin to flatten and become elongated up against the shelf, leading to the formation of lateral waves and consequent plumes on the shoreward edge of the Agulhas Current (Roberts et al., 2010). As a cyclonic eddy, the thermal structure within the core of a Durban Eddy has an upward orientated dome shape, which is associated with the upward movement of cooler, less saline, nutrient-rich water which contributes to the ecosystem functioning at the KZN Bight as well as further south along the southeast African shelf (Guastella and Roberts, 2016).

Ekman veering is current-driven shelf-edge upwelling which occurs due to the interaction between a geostrophic current and the slope topography (Leber et al., 2017). The Agulhas Current is described as being in approximate geostrophic balance as a result of the equal but opposite pressure gradient force and Coriolis force (Talley et al., 2011). When the current interacts with the sea floor, the effect of the bottom

friction breaks down the existing geostrophic balance, effectively slowing down the flow of the current (Talley et al., 2011). The resultant decrease in speed reduces the effect of the Coriolis force. The pressure gradient force then dominates over the Coriolis force, which results in an acceleration of the flow toward the region of low pressure, which in the case on the Agulhas Current means that water in the bottom boundary layer (BBL) is transported shoreward.

Roughan and Middleton (2002) discuss a few mechanisms that have been found to enhance Ekman veering in the BBL. Encroachment, defined by Roughan and Middleton (2002) as the onshore movement of a WBC at any latitude as time progresses, accentuates the alongshore current speed and uplifts the isotherms, both of which enhance Ekman veering in the BBL. Similarly, the translation of a WBC from flowing along a wider shelf to flowing along a narrower shelf, accelerates the current, and enhances Ekman veering (Roughan and Middleton, 2002).

Along the shelf break that flanks the Agulhas Current, this process is responsible for the upslope movement of deep, cold, less saline and nutrient-rich water into the lower layers of shelf and therefore, like Natal Pulses, this can give rise to the presence of central waters, uplifted by more than 130 m, on the shelf (Goschen et al., 2012, Leber et al., 2017). Studies carried out by Schumann (1986, 1987), presented evidence of the occurrence of Ekman veering in the BBL, estimated to be between 29 and 34 m thick, off Port Edward and East London, and Goschen et al. (2012) later suggested that Ekman veering occurred along the entire length of the southeast region.

2.4 Meteorological Forcing

Meteorological forcing has significant impacts on the dynamics of shallow shelf systems like that of the southeast African shelf and includes sea surface temperature (SST) differences, sea level alterations, current variations as well as increased freshwater input from river runoff (Royer, 1982, Schumann, 1981). The dominating large scale meteorological features along the southeast African shelf are the Subtropical High Pressure System (otherwise known as the Indian Ocean High) as well as passing coastal low pressure systems (Schumann, 1981).

The Subtropical High Pressure System, situated between 20 ^{o}S and 40 ^{o}S, is an atmospheric anticyclone with anticlockwise circulation (Gupta and Desa, 2001). The southeast African shelf is located within the transition zone between the trade wind belt in the north and the westerly wind belt in the south (Hutchings, 1994). Seasonally, the high pressure systems migrate by 4 ^{o} latitudinally (Taljaard, 1972). The westerly

wind belt has been found to dominate in winter due to the northward migration of the Subtropical High Pressure System, whereas in summer due to the southward position of the Subtropical High Pressure System, the trade wind belt has been found to dominate (Hutchings, 1994).

In order for the deep, cold, non-shelf water, brought onto the shelf by Ekman veering or cyclonic eddies, to break the surface inshore, another process is required (Herzfeld and Tomczak, 1999). As a result of the impinging wind field, wind-driven upwelling is responsible for the presence of the deep, cold, non-shelf waters at the surface (Herzfeld and Tomczak, 1999, Gill, 1982). Depending on the east/west orientation of the coastline between Cape St Francis and Port Alfred and the northeast/southwest orientation of the coastline between Port Alfred and Port Shepstone, easterly and north-easterly longshore winds, respectively, are considered as upwelling favourable (Schumann et al., 1982, Leber et al., 2017). These winds dominate during austral summer resulting in more upwelling during this season (Goschen and Schumann, 2011).

The input of stress from the prevailing winds results in a net offshore Ekman transport approximately 90° to the left of the wind as a result of the effect of the Coriolis force. The balance between the wind stress and the Coriolis force is not immediate, rather it becomes established over several inertial periods. In response to the divergence of surface waters at the coast which are drawn offshore through the established offshore Ekman transport, cold deeper waters are uplifted and replace the original surface waters at the coast (Leber et al., 2017, Smith, 1994). In a study carried out by Goschen et al. (2012), it was found that the cold water breaks the surface at the coast between 19 hours and 2.5 days after the presence of strong easterly component wind.

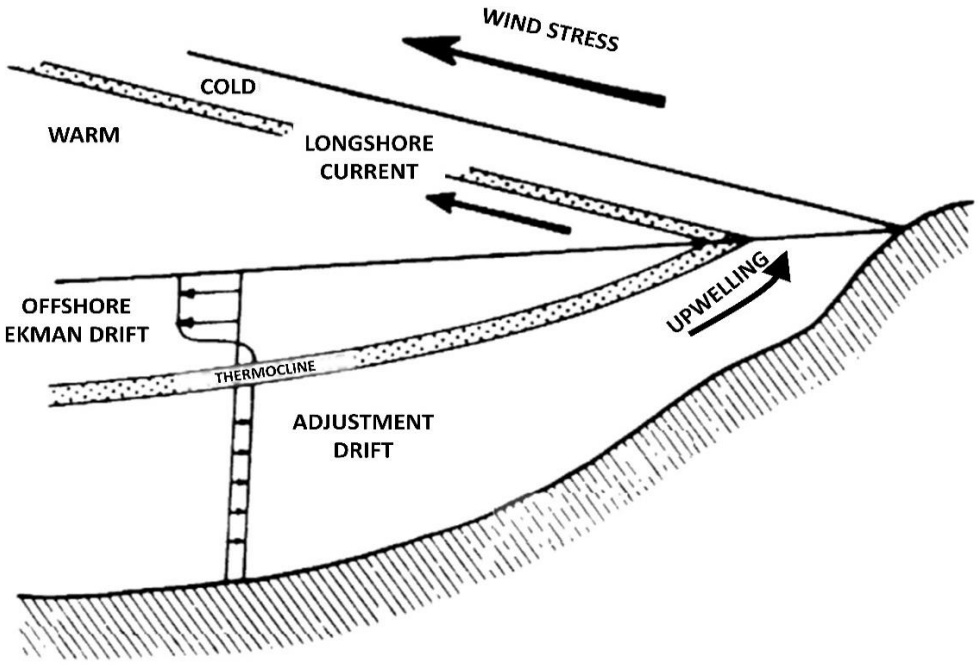

Figure 2.7 Schematic representation of wind-driven upwelling adapted from Schumann et al. (1982). Wind stress at the sea surface induces offshore Ekman transport (drift) in the surface layer which is compensated for and adjustment drift in the deeper layers resulting in upwelling along the coast.

The coastal low pressure systems, effecting the coastal environment of the southeast African shelf, originate on the west coast of South Africa and propagate eastward, following the coastline of southern African (Schumann, 1981). The propagation of coastal low pressure systems are found to coincide with the propagation of sea level disturbances known as coastal-trapped waves (CTWs) (Roberts et al., 2010). CTWs are vorticity dependant waves which in the southern hemisphere, propagate with the coast on the left in the direction of propagation (Goschen and Schumann, 2011). The orientation of the CTW crests is perpendicular to the coast with the amplitude decreasing offshore (Goschen and Schumann, 2011). Schumann and Brink (1990) found that the joint passage of the coastal low pressure systems and the CTWs resulted in the occurrence of temporary barotropic current reversals at the coast, usually lasting less than 24 hours (Goschen et al., 2012).

In the southern hemisphere, solar insolation is characteristically higher during austral summer and lower during austral winter (Schumann, 2013). The southeast African coast falls within the austral summer rainfall region (Landman and Goddard, 2002), which results in the seasonally varying input of large freshwater discharges from rivers into coastal waters (Tong et al., 2015). Therefore, the discharge from rivers along this

coast is expected to increase in summer months due to the increased rainfall. Seasonal differences in solar insolation and rainfall result in relatively high sea surface temperatures (SSTs) and generally lower surface salinities (Schumann, 2013, Lamont et al., 2016, Pearce, 1978, Pearce, 1977) during austral summer. The opposite is true for austral winter, during which SSTs are relatively lower (Pearce, 1978, Pearce, 1977) and surface salinities are relatively higher (Schumann, 2013, Lamont et al., 2016).

2.5 River Activity and Fluvial Input

There are nine major rivers situated along the southeast coastline of South Africa and they include (from south to north) the Gamtoos River, the Sundays River, the Great Fish River, the Great Kei River, the Mzimvubu River, the Mzimkulu River, the Mgeni River, the Mkomasi River and the Thukela River (see Figure 2.8). These rivers lie within South Africa's summer rainfall regions. Rainfall events and more specifically seasons of high rainfall, result in increased freshwater river discharge (Tong et al., 2015) and therefore increased river discharge is expected to occur more predominantly in the summer season. As a result of the river discharge, the injection of freshwater leads to lower levels of salinity which are initially concentrated at the river mouths and ultimately advected into the adjacent coastal waters (Vinayachandran et al., 2015). The freshwater signature from river outflow has been found to dissipate within a few kilometers of the river mouth. This has been previously discussed by Goschen and Schumann (2011) for the rivers in Algoa Bay and observed for the Thukela River by Lamont et al. (2016).

Significant correlations have been found to exist between river flow, rainfall and river nutrient concentrations (Emmerson, 1989). Decreasing nutrient concentration gradients from the river head to the river mouth are indicative of fluvial nutrient input (Emmerson, 1989, Hutchings et al., 2010). Fertilizer seepage as well as sewage input into rivers has been found to affect nutrient concentrations of the river water which ultimately affects the coastal water at the river mouths. A study of the Sundays River carried out by Emmerson (1989) found the presence of nitrogen enrichment which occurred due to the seepage of citrus fertilizer upstream in the river. As a result of urban sewage and industrial effluent input, phosphate enrichment is also found to occur in rivers (Emmerson, 1989).

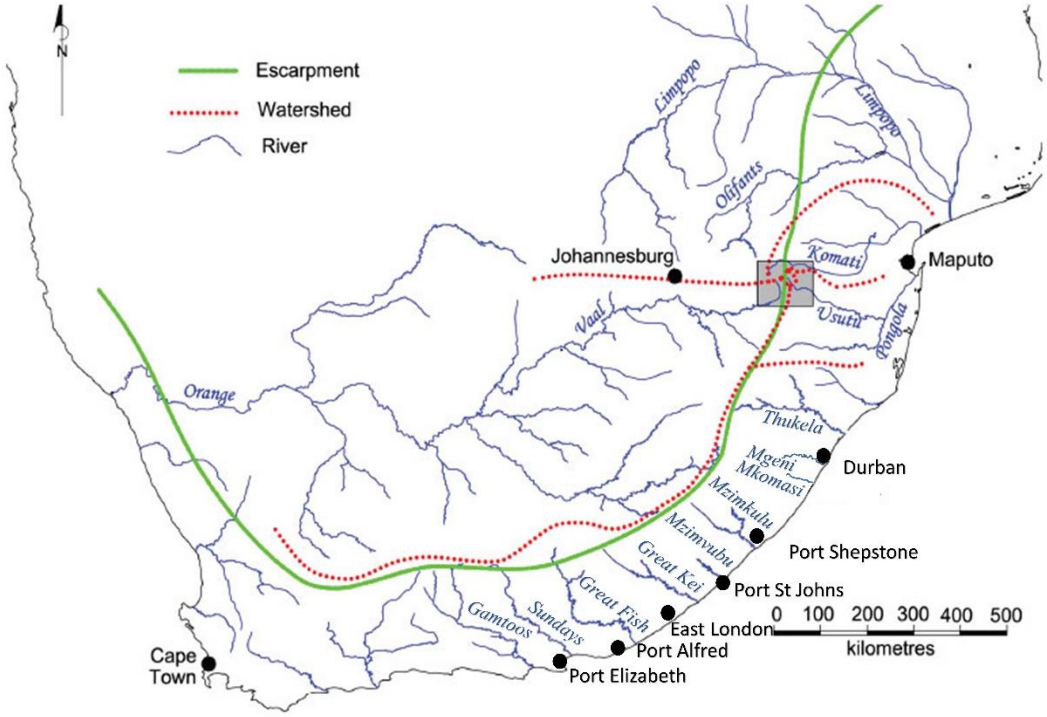

Figure 2.8 Map depicting the location of the rivers along the South African coastline adapted from McCarthy (2011).

3. Data and Methods

As stated in section 1.2, the objective of this current study is to identify the physical oceanographic processes occurring on the southeast African shelf and slope, as well as investigate the influence that the Agulhas Current has on the shelf and slope waters. In order to achieve this objective the following key questions were posed:

1. What are the physical oceanographic processes occurring in January/February and July/August 2017 on the southeast African shelf and slope and how do they differ?
2. How are the southeast African shelf and slope influenced by the adjacent Agulhas Current?
3. What water masses are present on the southeast African shelf and slope in January/February and July/August 2017 and what are their properties?

In order to answer the three key questions, a combination of *in situ* and satellite data, obtained for January/February and July/August 2017, was analysed using figures produced in both Ocean Data View (ODV) version 4.7.8 and Matrix Laboratory (MATLAB®) version R2015a.

3.1 In Situ Data

3.1.1 Cruise Data

As part of a collaborative project between the Department of Environmental Affairs (DEA), the African Coelacanth Ecosystem Programme (ACEP) and the Operation PHAKISA initiative, two hydrographic surveys of the southeast African shelf took place aboard the RV Algoa in 2017. The first took place in the austral summer, from 13 January to 10 February, and the second took place in the austral winter, from 12 July to 14 August. The aim of these multi-disciplinary cruises was to examine the influence of the Agulhas Current on the biological communities of the southeast African shelf. The cruises operated on the southeast African shelf and the continental slope, starting just west of Cape St Francis in the south and moving toward Port Shepstone in the north (Figure 3.1).

The same cruise track and stations were sampled throughout both cruises. This consisted of 38 transects with a total of 217 stations (Figure 3.1). The transects, approximately 18.5 km apart, comprised of between five and seven stations which began inshore and extended offshore over the shelf break. The most inshore stations,

located on the shelf had a bottom depth of 20 m and the most offshore stations, on the slope, had a bottom depth of 1000 m. Between the two extremes were stations covering depths from 50 to 250 m. This type of transect orientation design enabled a high resolution, longitudinal and latitudinal, overview of the processes occurring across the shelf.

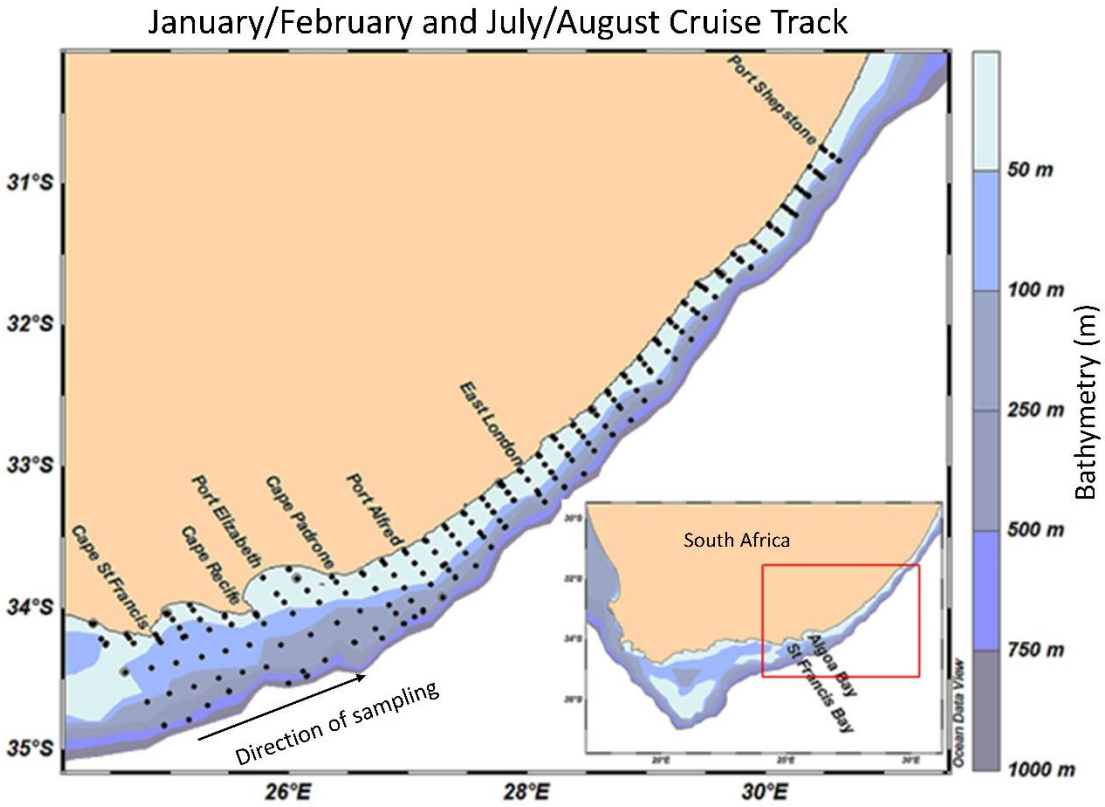

Figure 3.1 Map of the study area depicting the cruise track of the January/February and July/August cruises, outlining the stations sampled during both cruises (depicted by the black dots) as well as the underlying bathymetry (depicted by the shading). The inset shows the study area (red box) in the context of South Africa.

In order to obtain data on the vertical structure of hydrographic properties between Cape St Francis and Port Shepstone, a Conductivity, Temperature and Depth instrument (CTD) Sea-Bird Electronics (SBE) 911 plus was used. Attached to the CTD was a Photosynthetically Available Radiation (PAR) sensor, an oxygen sensor, a flourometer, a transmissometer, a backscatter meter as well as a 12x5 L Niskin bottle rosette. Vertical profiles of temperature, salinity, dissolved oxygen (DO) and fluorescence were obtained from all of the stations, with the use of the CTD.

Nutrient samples (50 ml) were collected from selected Niskin bottles at certain depths at every station and were stored in the -80 ^{o}C freezer for further analysis in the laboratory which will be further discussed in section 3.3.1.1. These certain depths

were chosen for nutrient collection according to the variability in the structure of the water column, so as to acquire an accurate representation of the nutrient profile throughout the water column. DO water samples were collected from certain depths and analysed in the laboratory aboard the RV Algoa, using Winkler titrations (Carpenter, 1965, Carrit and Carpenter, 1966). Chlorophyll-a (chl-a) samples (500 ml) were collected from selected Niskin bottles at certain depths at every station. The depths from which the chl-a samples were collected were chosen in order to capture the variable structure of the fluorescence profiles. The chl-a samples were filtered through 25 mm GF/F filters which were the stored in the freezer for further analysis. The chl-a samples were analysed in the laboratory at the Department of Environmental Affairs (DEA), using the Welshmeyer method (Welschmeyer et al., 1991). The analysed DO and chl-a samples were used for the calibration of the oxygen sensor and flourometer on the CTD, respectively.

The CTD data, collected using the Seasave software (version 7.26.7), was processed using version 7.26.7 of the SBE Data Processing software (Sea-Bird Scientific, 2018). With the use of the Seasoft V2: SBE Data Processing Manual, the following processing steps were carried out (Sea-Bird Scientific, 2017). Initially the data were converted from hexi-decimal to scientific units and thereafter a sensor alignment took place, which essentially matched measurements with the same parcel of water. The data were then filtered in order to remove any remaining digital noise using a Low pass filter. Scan lines with spikes, caused by the ship heave, were removed using pressure loops. The cell thermal mass error for a given flow rate on the conductivity cell was corrected. Dependent variables (salinity, DO concentration, density and sound velocity) were derived from the newly corrected independent variables (temperature, conductivity, pressure and OXVOLTS). The data was then binned, with regards to pressure, into evenly spaced bins of 1 db. The downcasts and upcasts were split and the data were written to an ASCII file which was imported into ODV for plotting. Once processed, the data were ready for analysis which will be further discussed in section 3.3.1.

Current speed and direction data, describing the current dynamics between Cape St Francis and Port Shepstone were obtained, for the summer cruise (January – February 2017) only, using a 75 kHz shipboard Teledyne RD Instruments acoustic Doppler current profiler (S-ADCP). The S-ADCP was set-up to collect data over a total depth of 560 m using 70 bins, which were 8 m in size (Department of Environmental Affairs, 2017). The S-ADCP had an alignment correction set to -46 º in relation to the ship. The current velocity data were then recorded using the Teledyne RD Instruments

VMDAS (version 1.46) software. Once collected, the Short Term (3 minute) Averaged (STA) data were processed to a maximum depth of 500 m and extracted into spreadsheets using the Aqua Vision ViSea DAS and ViSea DPS software (Department of Environmental Affairs, 2017). Once processed, the data was analysed as discussed in further detail in section 3.3.1.

3.1.2 River and Rainfall Data

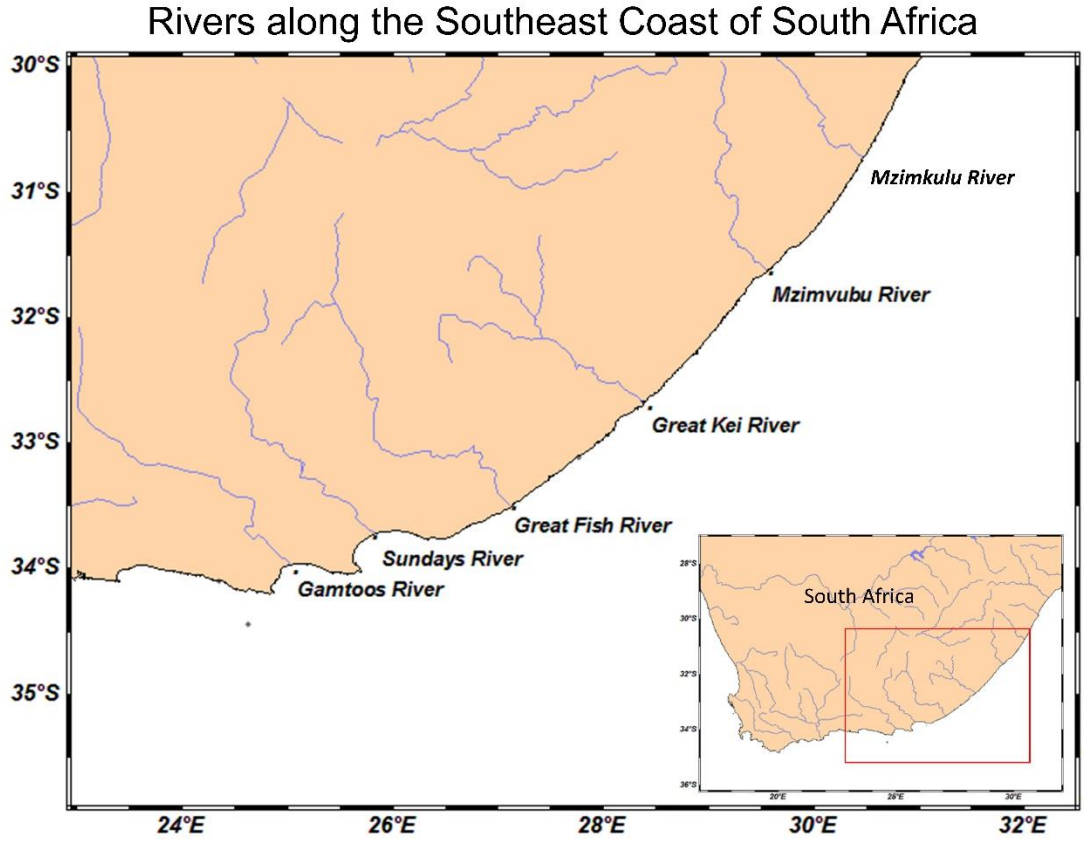

Figure 3.2 Map depicting the rivers along the southeast coast of South Africa in the study area, with the nearby hydrographic sampling was conducted on both of the ACEP research cruises during 2017. The inset shows the study area (red box) in the context of South Africa.

Throughout the year, the Department of Water and Sanitation measure and record the flow rates of the rivers countrywide. For the purpose of this study, six of the nine previously mentioned major rivers were considered and their flow data were acquired from the Department of Water and Sanitation's website (http://www.dwa.gov.za/Hydrology). As can be seen in Figure 3.2 these six rivers include: the Gamtoos River, the Sundays River, the Great Fish River, the Great Kei River, the Mzimvubu River and the Mzimkulu River. While the Mgeni River, the Mkomasi River and the Thukela River are major rivers that also outflow on the East

Coast of South Africa, they were not considered as they do not fall within the area of study outlined in section 3.1.1. Data on the river flow rates for the Gamtoos River and the Mzimkulu River were not available for the given time periods from the Department of Water and Sanitation. Rainfall data in the form of historical rainfall maps were acquired from the South African Weather Service (SAWS) website - http://www.weathersa.co.za.

3.2 Satellite Data

Altimetry data products, such as Sea Level Anomaly (SLA), Absolute Dynamic Topography (ADT), as well as geostrophic current velocity data, are collated by Archiving, Validation and Interpretation of Satellite Oceanographic data (AVISO). Various satellites circle the globe and measure the time taken for a radar pulse to leave the satellites' antennas, reach the surface and return back to the receiver. This information is combined with precise satellite location data yielding a sea surface height (AVISO, 1996). The raw telemetry data get sent to ground stations and are forwarded to quality control centres for quality control and processing and are transformed into level 1 data (AVISO, 1996). The level 1 data are then corrected for any instrumental errors and atmospheric perturbations and are then corrected for any geophysical errors, transforming the level 1 data into level 2 data (AVISO, 1996). The Centre Multimissions Altimètre (CMA) performs quality control and validation on the level 2 data which involves a further correction for instrumental drift, thus creating level 3 data (AVISO, 1996). The data, which have a ¼ º spatial resolution and a daily temporal resolution is made readily available for scientific application from the Copernicus Marine Environment Monitoring Service (CMEMS) website, http://marine.copernicus.eu/ – a platform that provides regular and systematic data on the state of the physical ocean and regional seas.

The Sea Surface Height (SSH) above the reference ellipsoid, depicted in Figure 3.3, is obtained from the altimetry by subtracting the altimetric range from the orbit (Mertz et al., 2018). The geoid is the level surface corresponding to the ocean surface at rest (Stewart, 2008). The Mean Sea Surface (MSS), which is the mean surface above the ellipsoid including the Geoid, is the temporal mean of the SSH over a period N (Figure 3.3). In the case of the product used in this study, the geoid was computed with respect to a twenty-year mean (Rio et al., 2013). The Sea Level Anomaly (SLA), depicted in Figure 3.3, is then calculated by subtracting the MSS from the SSH (Mertz et al., 2018). The Mean Dynamic Topography (MDT), which is the temporal mean of the SSH above the Geoid over a period N, is deduced by subtracting the Geoid from

the MSS (Figure 3.3). Finally, the Absolute Dynamic Topography (ADT), illustrated in Figure 3.3, is obtained by adding the SLA to the MDT (Mertz et al., 2018).

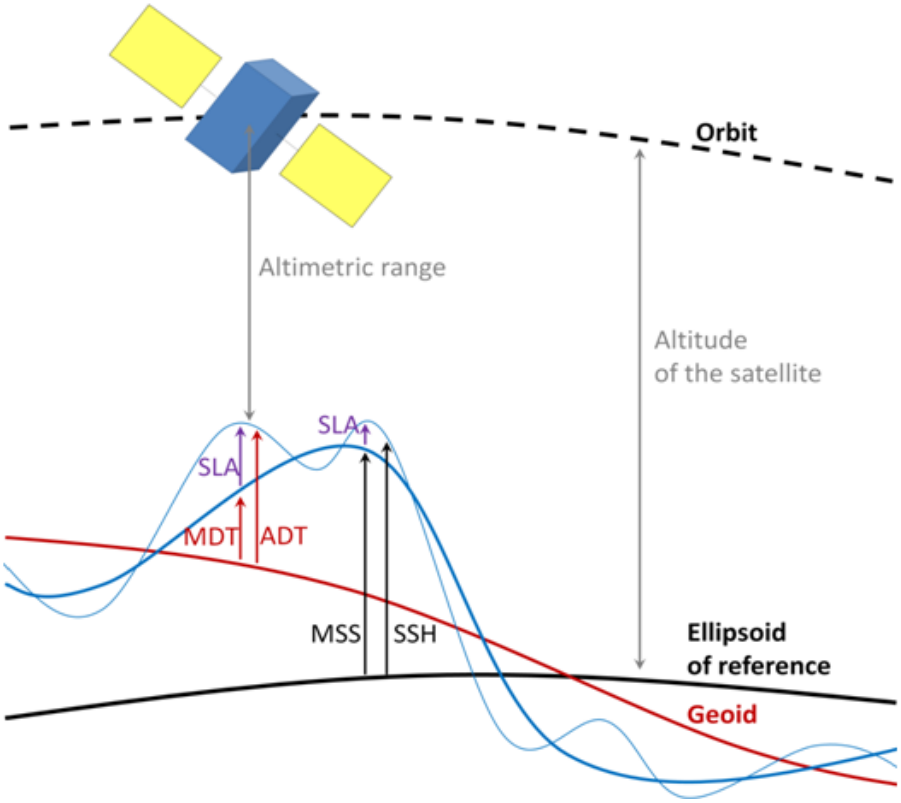

Figure 3.3 Schematic representation of the altimetry principle after Mertz et al. (2018)

Sea surface temperature (SST) data, assembled by ODYSSEA, was also acquired from the CMEMS website. This is a supercollated product as it is a multi-sensor composite, giving it an ultra-high spatial resolution of 0.1 ◦ and a daily temporal resolution. The SST ODYSSEA product is created using a collection of level 2 data from different producers such as NASA, NOAA, and EUMETSAT etc. The collection of level 2 SST data goes through a quality control and then compositing process and is transformed into a single sensor level 3 composite (Piollé and Autret, 2011). The single sensor level 3 composite is corrected for a satellite bias and thereafter goes through a merging process where an adjusted multi-sensor level 3 composite is created (Piollé and Autret, 2011). The final product is then disseminated via CMEMS.

The National Centres for Atmospheric Prediction (NCEP) and the National Center for Atmospheric Research (NCAR) collaborated in producing a dataset known as NCEP-1 Reanalysis. The data are produced using a frozen state-of-the-art global data

assimilation model similar to that which is used for weather forecasts and produces a variety of parameters such as maximum temperature, relative humidity as well as the zonal and meridional components of wind (Kalnay et al., 1996). The model is initialised with actual measured data from a database which is as holistic as possible and consists of a variety of sources such as weather stations, ships, radiosondes and satellite (Kalnay et al., 1996). The data go through a process of preparation, assimilation (producing a homogenous dataset) and ultimately distribution (Kalnay et al., 1996). The zonal and meridional wind components, which has a spatial resolution of 2.5 ° and a 6-hourly temporal resolution, was acquired from the Earth Systems Research Laboratory website: http://www.esrl.noaa.gov/psd/data/gridded/data.ncep.reanalysis.html.

Chlorophyll-a (chl-a) concentration data, produced by ACRI-ST Company, using the Copernicus-Globcolour processor, were acquired from the CMEMS website. The global ocean chl-a concentration product is created using a collection of level 2 data from NASA. Level 2 data acquired from the Moderate Resolution Imaging Spectroradiometer aboard the Aqua spacecraft (MODIS-Aqua) and the Visible Infrared Imaging Radiometer Suite (VIIRSN) go through a pre-processing stage after which they go through a spatial binning (4 km) stage (Volpe et al., 2017). The newly processed and spatially binned level 3 MODIS-Aqua and VIIRSN data then goes through a temporal binning (daily) stage (Volpe et al., 2017). The binned level 3 MODIS-Aqua and VIIRSN data is then merged to form a daily merged product with a 4 km spatial resolution (Volpe et al., 2017). The data is then disseminated via CMEMS.

3.3 Data Analyses

3.3.1 *In Situ* Data Analysis

The analysis of the *in situ* data was done by executing calculations in Microsoft Excel and by producing figures using both ODV (version 4.7.8) and MATLAB® (version R2015a). ODV was used to derive variables such as absolute salinity and conservative temperature according to TEOS-10, while neutral density, a non-thermodynamic density variable which is a function not only of salinity (psu), *in situ* temperature (°C) and pressure (db) but also of the geographic variables of latitude and longitude, was derived according to Jackett and McDougall (1997).

Absolute Salinity is a conservative concentration variable which can be defined as the function of Practical Salinity, pressure, longitude and latitude (Pawlowicz, 2010). Practical salinity is an almost directly measured quantity which is calculated from *in situ* conductivity, temperature and pressure values (IOC et al., 2010). It is essentially the measure of the distribution of conductive ions in seawater, whereas Absolute Salinity is defined by TEOS-10 as the mass fraction of all dissolved non-H2O material in seawater (Pawlowicz, 2010).

Conservative temperature, which represents the “heat content” per unit mass of seawater (McDougall and Barker, 2011), is defined as the function of Absolute Salinity, *in-situ* temperature, and pressure (Pawlowicz, 2010). *In situ* temperature, the quantity that is physically measured, is affected by changes in pressure, as well as the varying heat capacity of seawater (Pawlowicz, 2013). Potential temperature is a variable which takes into account the effects of pressure, such that it is the temperature of a water parcel, if it were to be brought up to the surface adiabatically (Pawlowicz, 2013). While potential temperature is insensitive to pressure, it does not take into account the varying heat capacity of seawater and so TEOS-10 introduced a conservative variable (Conservative Temperature) which takes into account the effects of pressure as well as the effects of varying heat capacity of seawater (Pawlowicz, 2013).

ODV was used to produce vertical sections of the transects, as well as surface plots of the study area using the conservative temperature, absolute salinity, neutral density, DO, chlorophyll-a (chl-a) and backscatter data. This was done in order to gain a detailed understanding of the observed conditions on the southeast African shelf. The mixed layer depth (MLD) for sites A, B, C, E and F have been determined, using Microsoft Excel, as the depth where the local change in density is greater and equal to 0.05 $kg.m^{-3}$ over a depth interval of 1 m, as has been done previously by Barlow et al. (2010). Where no such density change was observed throughout the water column, the respective bottom depth in Table 4.2 was used at the MLD. Temperature-Salinity (TS) plots were created primarily to accurately identify the water masses present, as well as describe their location relative to the shelf. Secondly they were used to see if there was any river influence in either season which would be depicted by anomalously low salinities. While each of the surveys took in excess of 30 days, these figures that were produced, represent an amalgamation of events at different times but given that they represent a glimpse of conditions during particular seasons, for the sake of simplicity, the word snapshot has been used to refer to these maps.

MATLAB® was used to produce vertical sections of the S-ADCP data as well as a surface plot of the velocity vectors. This was done in order to understand the general flow of the currents in the region during the cruise. River flow rates were compiled into tables using in excel and analysed in order to see if the rivers had a significant impact on the water at certain inshore stations that were sampled during the hydrographic surveys along the southeast African shelf. The data were also used to compare the river flow rates in summer with those in winter.

3.3.1.1 Nutrient Analysis

The nutrient analysis was carried out in the laboratory in the Department of Oceanography at the University of Cape Town. After the analyses were completed the final product was added to a spreadsheet and imported into ODV. Surface maps and vertical sections of the various nutrients were plotted using ODV and were further studied. There were four nutrients that were analysed, and these are: nitrate, silicate, nitrite and phosphate. The nitrate and silicate analyses were done using the Lachat Autoanalyzer, whereas the nitrite and phosphate analyses, were carried out manually.

The determination of nitrate was conducted using the Lachat Autoanalyzer which used the Lachat QuickChem® method 31-107-04-1-C (Nitrate/Nitrite in brackish/seawaters by Cadmium Reduction in Flow Injection Analysis) which had a detection limit of 0.12 µM (Lachat Instruments, 2012). The nitrate is reduced to nitrite by passing through a copperized cadmium column. The total nitrite is determined by diazotizing it with sulphanilamide and N-(1-Naphthyl)ethylenediamine (N-NED) dihydrochloride. A magenta azo dye forms and is read at a wavelength of 520 nm. The removal of the cadmium column allows for the determination of nitrite alone. The nitrate concentration therefore can be determined via the subtraction of the concentration of nitrite alone from the total nitrite (including the reduced nitrate). The peak heights of known concentrations of nitrate were measured and plotted to create a standard curve. The equation (Equation 3.1) of the polynomial line of best fit from the standard curve (Figure 3.4) was then used to calculate the micromolar concentration of nitrate for all samples.

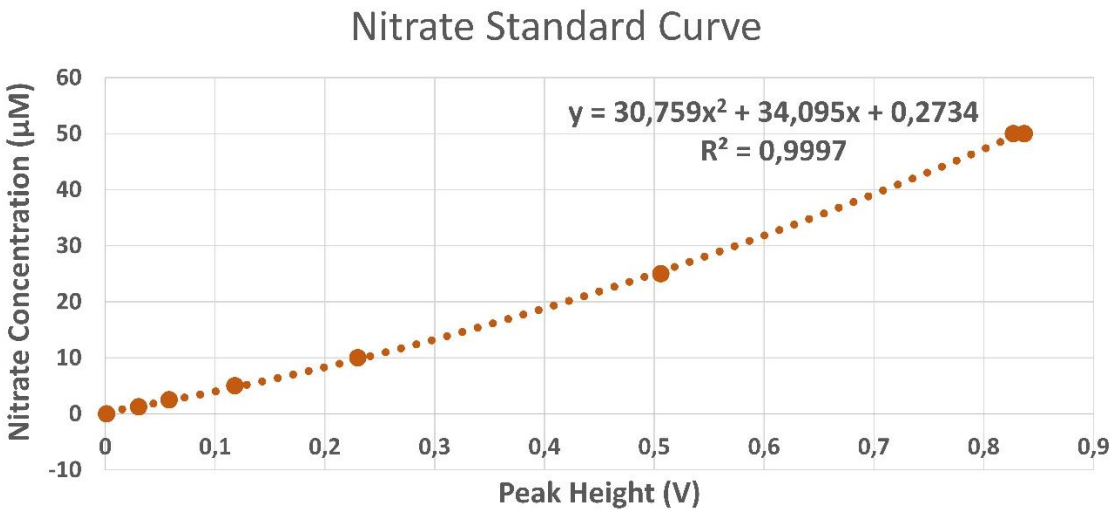

Figure 3.4 Nitrate standard curve. The x-axis represents the peak height reading in volts and the y-axis represents the micromolar concentration of nitrate.

$$y = 30{,}759x^2 + 34{,}095x + 0{,}2734$$

$$\therefore [NO_3] = 30{,}759(\text{peak height})^2 + 34{,}095(\text{peak height}) + 0{,}2734$$

Equation 3.1 Equation used to calculate the concentration of nitrate from the peak height measured using the Lachat Autoanalyzer, where y is the micromolar concentration of nitrate and x is the peak height in volts.

The determination of silicate was also conducted using the Lachat Autoanalyzer which used the Lachat QuickChem® method 31-114-27-1-A (Molybdate-Reactive Method for Silicate in brakish/seawaters by Flow Injection Analysis) with a detection limit of 0.2 µM (Lachat Instruments, 2012). The silicate is determined by adding molybdate under acidic conditions. The molybdate reacts with the silicate and forms a yellow beta molybdosilicic acid which is then reduced with stannous chloride, forming a heteropoly blue complex. This complex is then read at a wavelength of 820 nm where the peak height is determined. In order to calculate the silicate concentrations for all of the samples, a standard curve is constructed using known concentrations of silicate and the corresponding measured peak heights. The polynomial equation (Equation 3.2) of the line of best fit from the standard curve (Figure 3.5) was then used to calculate the micromolar concentration of silicate for all samples.

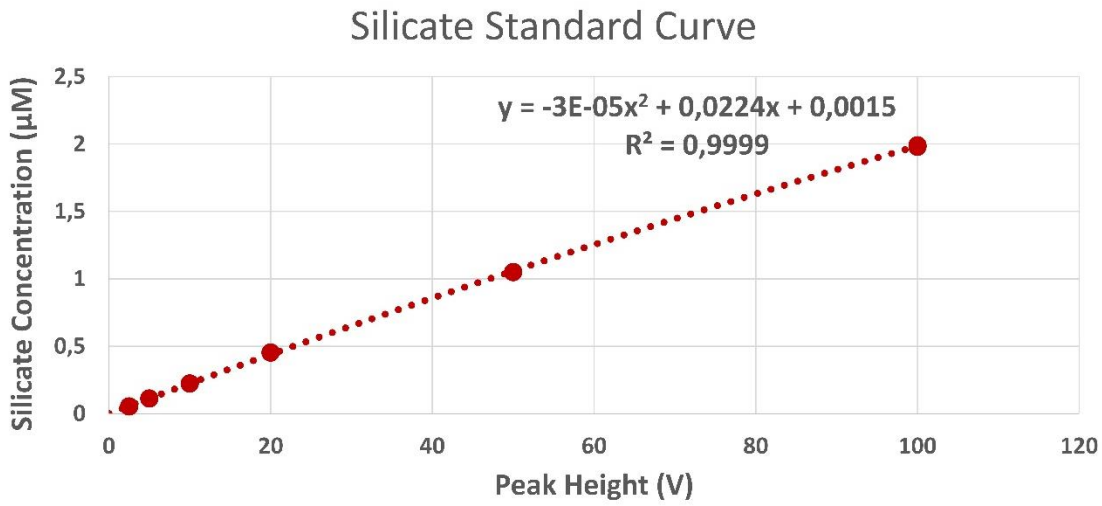

Figure 3.5 Silicate standard curve. The x-axis represents the peak height reading in volts and the y-axis represents the micromolar concentration of silicate.

$$y = -3E-05x^2 + 0{,}0224x + 0{,}0015$$

$$\therefore [SiO_4] = -3E-05(\text{peak height})^2 + 0{,}0224(\text{peak height}) + 0{,}0015$$

Equation 3.2 Equation used to calculate the concentration of silicate from the peak height measured using the Lachat Autoanalyzer, where y is the micromolar concentration of silicate and x is the peak height in volts.

The determination of nitrite was conducted manually using the nitrite test method obtained from Grasshoff et al. (1983). Using a 5 ml Eppendorf pipette, 5ml of each sea water sample was transferred into labelled test tubes and set in test tube racks. 0.1 ml of Sulphanilamide was added into each test tube. The contents of each test tube was then gently mixed using the vortex mixer and was set aside and allowed to react for 2-8 minutes after which a p-diazonium sulphanilamide formed. 0.1 ml of N-NED was added into each of the test tubes. The contents of each test tube was gently mixed, again using the vortex mixer and set aside to react for 10 minutes which allowed for the formation of a pink azo dye. The Spectronic™ Helios™ Epsilon™ spectrophotometer, set at a wavelength of 543 nm, was zeroed using a sample of deionised water and the absorbance of each sample was thereafter measured. The values were then recorded into a spreadsheet. In addition to the collected nutrient samples, varying standards of nitrite were prepared. Their absorbance values were measured and recorded using the same processes as discussed above. A standard curve (Figure 3.6) for nitrite (absorbance at 543 nm vs concentration) was plotted and was used to determine the corresponding nitrite micromolar concentrations of the

samples. The concentration of nitrite for all samples was thus determined using the equation (Equation 3.3) from the line of best fit from the standard curve (Figure 3.6).

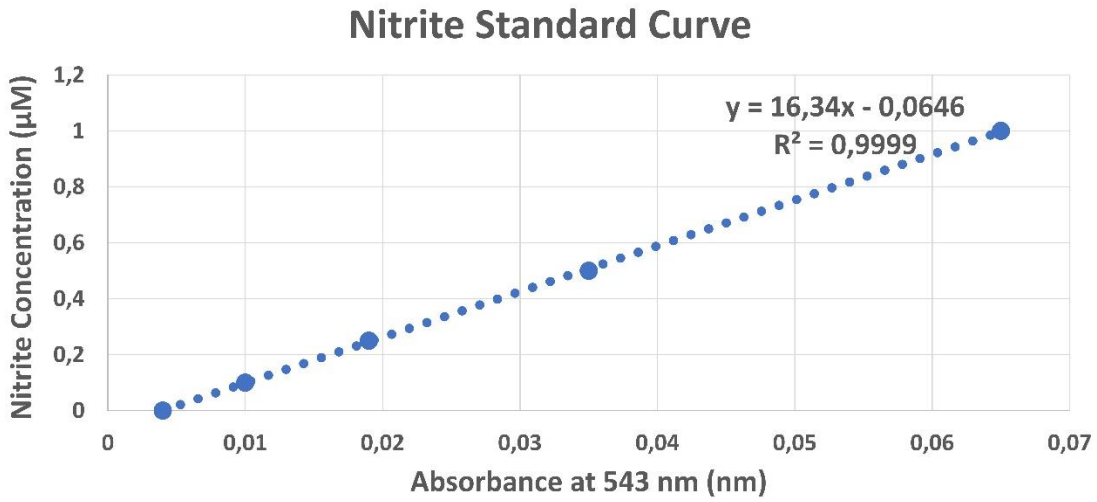

Figure 3.6 Nitrite standard curve. The x-axis represents the absorbance reading at 543 nm and the y-axis represents the micromolar concentration of nitrite.

$$y = 16{,}34x - 0{,}0646$$

$$\therefore [NO_2] = 16{,}34(ABS_{543}) - 0{,}0646$$

Equation 3.3 Equation used to calculate the concentration of nitrite from an absorbance reading using a wavelength of 543 nm, where y is the micromolar concentration of nitrite and x is the absorbance at 543 nm.

The determination of phosphate was conducted manually using the modified single solution method for the determination of phosphate in natural waters from Murphy and Riley (1962). A mixed reagent was prepared in a volumetric flask by adding 10 ml of ammonium molybdate, 25 ml of sulphuric acid, 10 ml of ascorbic acid (at which point there was a yellow colour change) and finally 5 ml of potassium antimonyl-tartrate. 5 ml of each nutrient sample was transferred into labelled test tubes using a 5 ml Eppendorf pipette. 0.5 ml of the mixed reagent was added into each test tube. The contents of each test tube was gently mixed using the vortex mixer and were set aside to allow to react for 10 minutes. The Spectronic™ Helios™ Epsilon™ spectrophotometer was set to a wavelength of 885 nm and zeroed with a test tube filled with deionised water. The absorbance values were read and recorded into a spreadsheet. Varying standards of phosphate were prepared, measured and recorded using the method above. This allowed for a standard curve (Figure 3.7) to be made. The equation of the line of best fit (Equation 3.4) from the phosphate

standard curve (Figure 3.7) was then used to calculate the micromolar concentrations of phosphate for all the samples.

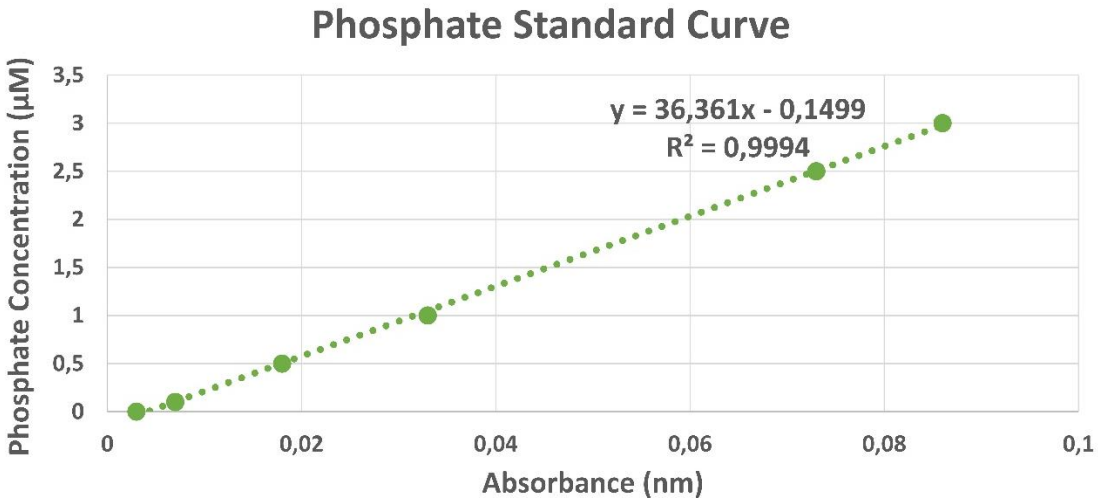

Figure 3.7 Phosphate standard curve. The x-axis represents the absorbance reading at 885 nm and the y-axis represents the micromolar concentration of phosphate.

$$y = 36{,}361x - 0{,}1499$$

$$\therefore [PO_4] = 36{,}361(ABS_{885}) - 0{,}1499$$

Equation 3.4 Equation used to calculate the concentration of phosphate from an absorbance reading using a wavelength of 885 nm, where y is the micromolar concentration of phosphate and x is the absorbance at 885 nm.

3.3.2 Satellite Data Analysis

The analysis of the satellite data was accomplished using MATLAB®. Sea surface temperature (SST) surface plots were produced for days leading up to and during the cruises so as to give a general understanding of the prevailing conditions as well as locate any anomalous activity. Chlorophyll-a (chl-a) surface maps were produced using MATLAB® but due to excessive cloud cover during the time of both cruises (see Figure 3.8) they were not considered in this study. Daily surface plots of the Sea Level Anomaly (SLA) and geostrophic velocity vector data were produced and this was done in order to identify any mesoscale variability (eddies) as well as detect the origin of such activity. Surface plots of shipboard acoustic Doppler current profiler (S-ADCP) data were merged with SLA and geostrophic current vector data to allow for the comparison of the *in situ* velocities with the satellite data (SLA and geostrophic velocity vectors).

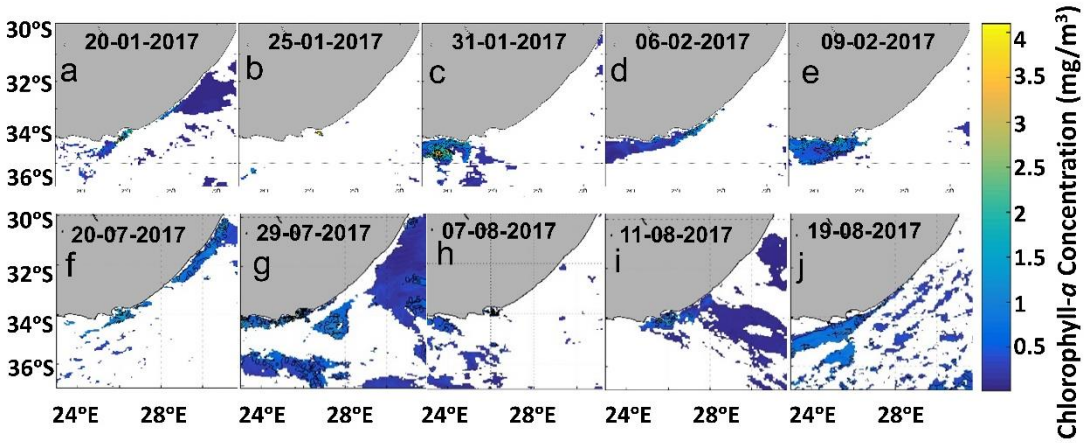

Figure 3.8 Time series of surface chl-a concentration maps spanning a range of days during the January/February (a-e) and July/August (f-j) cruises highlighting the cloud cover obstruction.

Wind field maps for particular days were produced in order to determine whether upwelling favourable wind conditions existed on or prior to the days of the upwelling events. In addition, the Ekman Layer Depth (ELD) of the five sites exposed to upwelling favourable winds (further discussed in section 4.8) was calculated using Equation 3.5 given by Stewart (2008) in order to determine the wind-influenced depth within the water column. Equation 3.5 indicates that the ELD is a function of the resultant wind speed 10 m above the sea (U_{10}) and latitude (θ). Stewart (2008) calculated the constant of 7.6 in Equation 3.5 using ρ = 1027 kg.m^{-3} (surface density of sea water), ρ_{air} = 1.25 kg.m^{-3} (surface air density) and C_D = 2.6 x 10^{-3} (Ekman's value for the drag coefficient). Given that this equation assumes a homogenous ocean, where A_z remains constant with depth and where the wind speed remains constant, the calculated depths may be overestimated.

$$D_E = \sqrt{\frac{2\pi^2 A_z}{f}} = \frac{7.6}{\sqrt{sin|\theta|}} U_{10}$$

Equation 3.5 Equation used to calculate Ekman Depth which is a function of wind speed at 10 m above the sea surface (U_{10}) and latitude (θ) acquired from Stewart (2008).

4. Results

The southeast African shelf exists along the southeast coast of South Africa on the inshore edge of the Agulhas Current. This historically under-sampled region has been the focus of few *in situ* studies which have either been bay scale (Goschen et al., 2012, Roberts, 2010), which fail to identify the larger surrounding oceanographic features, or larger scale (Lutjeharms et al., 2010), which fail to identify the finer details. The objective of this study is to identify the physical oceanographic processes occurring on the southeast African shelf and slope and investigate the influence that the Agulhas Current has on the shelf and slope waters. In order to achieve the objective of this study, the following three key questions have been posed:

1. What are the physical oceanographic processes occurring in January/February and July/August 2017 on the southeast African shelf and slope and how do they differ?
2. How are the southeast African shelf and slope influenced by the adjacent Agulhas Current?
3. What water masses are present on the southeast African shelf and slope in January/February and July/August 2017 and what are their properties?

In order to answer these three key questions, this section implements an approach which uses the combination of shelf-wide high resolution *in situ* data as well as slightly courser resolution satellite data in order to identify and assess both the larger and shelf/smaller scale physical oceanographic processes occurring on the southeast African shelf. This section is split into a large scale overview of the hydrographic parameters which is followed by a more detailed investigation of features in the form of four case studies.

4.1 General Circulation and Mesoscale Variability

Absolute Dynamic Topography (ADT), Sea Level Anomaly (SLA), geostrophic velocity vectors, geostrophic velocity anomaly vectors as well as shipboard acoustic Doppler current profiler (S-ADCP) data are shown in Figure 4.1 to Figure 4.3. These figures were examined in order to determine the general circulation of the study area, as well as determine whether any mesoscale variability was present at the time of sampling during both the January/February and July/August 2017 cruises. Technical difficulties experienced during the July/August cruise, resulted in a lack of S-ADCP data for that

cruise. For this reason S-ADCP data is presented for the January/February 2017 cruise only.

4.1.1 January/February 2017 – Austral Summer

The ADT and geostrophic velocity vector data, seen in Figure 4.1a, depict a strong south-westward flow, with speeds greater than 2 $m.s^{-1}$, in close proximity to the coastline, between Port Shepstone and Cape Padrone. This same south-westward flow of the Agulhas Current is observed in the S-ADCP velocity vector data, seen in Figure 4.2. In Figure 4.2 however, the velocity vectors are noticeably smaller inshore and larger offshore. The relatively strong south-westward flow is observed further offshore, south-west of Cape Padrone (Figure 4.1a and Figure 4.2).

A decrease in velocity, as well as a variation in the meridional component of the geostrophic velocity vectors, was observed west of Cape Padrone, between the coast and the inshore edge of the Agulhas Current (Figure 4.1a). A similar pattern was observed in the S-ADCP data (Figure 4.2), where there was a decrease in velocity, as well as variation in both the meridional and zonal components of the S-ADCP velocity vectors. North-eastward S-ADCP velocity vectors were observed south of Cape St Francis, depicting a current reversal (Figure 4.2). This current reversal, although not observed in the ADT data in Figure 4.1a, is depicted in the SLA data seen in Figure 4.1b. As can been seen in Figure 4.1b, a SLA of -0.25 m, located at 35 ^{o}S, is accompanied by cyclonic circulation, seen extending into Algoa Bay, which is depicted by the geostrophic velocity anomaly vectors all of which are consistent with the presence of a cyclonic cold-core eddy (hereafter termed the January/February cyclonic eddy).

The January/February cyclonic eddy, whose core was located along the 2000 m isobath at 35°S and 24.8°E and inshore edge was located along the 1000 m isobath (Figure 4.1b), measured approximately 90 km (34.8°S-35.6°S) latitudinally and 250 km (23.8°E-26°E) longitudinally. The January/February eddy was observed to originate from the KwaZulu-Natal (KZN) Bight on the 18th of October 2016 (Figure A.1). The propagation speed of the cyclonic eddy was calculated using the distance along the 200 m contour from Durban to Port Alfred, divided by the total time (in days) taken for it to propagate along that distance from Durban to Port Alfred. Similar calculations were carried out by Rouault and Penven (2011). The distance along the 200 m contour from Durban to Port Alfred was calculated to be approximately 546 km. It took the January/February eddy 59 days to propagate along the 546 km from

Durban to Port Alfred, reaching Port Alfred on the 15th of December 2016 (Figure A.1). It therefore, had a propagation speed of approximately 9.25 km/day. While the propagation speed is slightly slower than those of Natal Pulses (10-20 km/day; de Ruijter et al., 1999), the size and origin characteristics are consistent with those of Natal Pulses.

In terms of direction, there is good agreement in the patterns between the satellite data depicted in Figure 4.1 and the *in situ* data depicted in Figure 4.2. The satellite data (Figure 4.1a and b), displayed similar speeds (>2 $m.s^{-1}$) to the *in situ* for the inshore edge of the Agulhas Current but slightly underestimated the speed observed by the *in situ* data (Figure 4.2) for the inshore and mid-shelf region, between Cape St Francis and Cape Padrone.

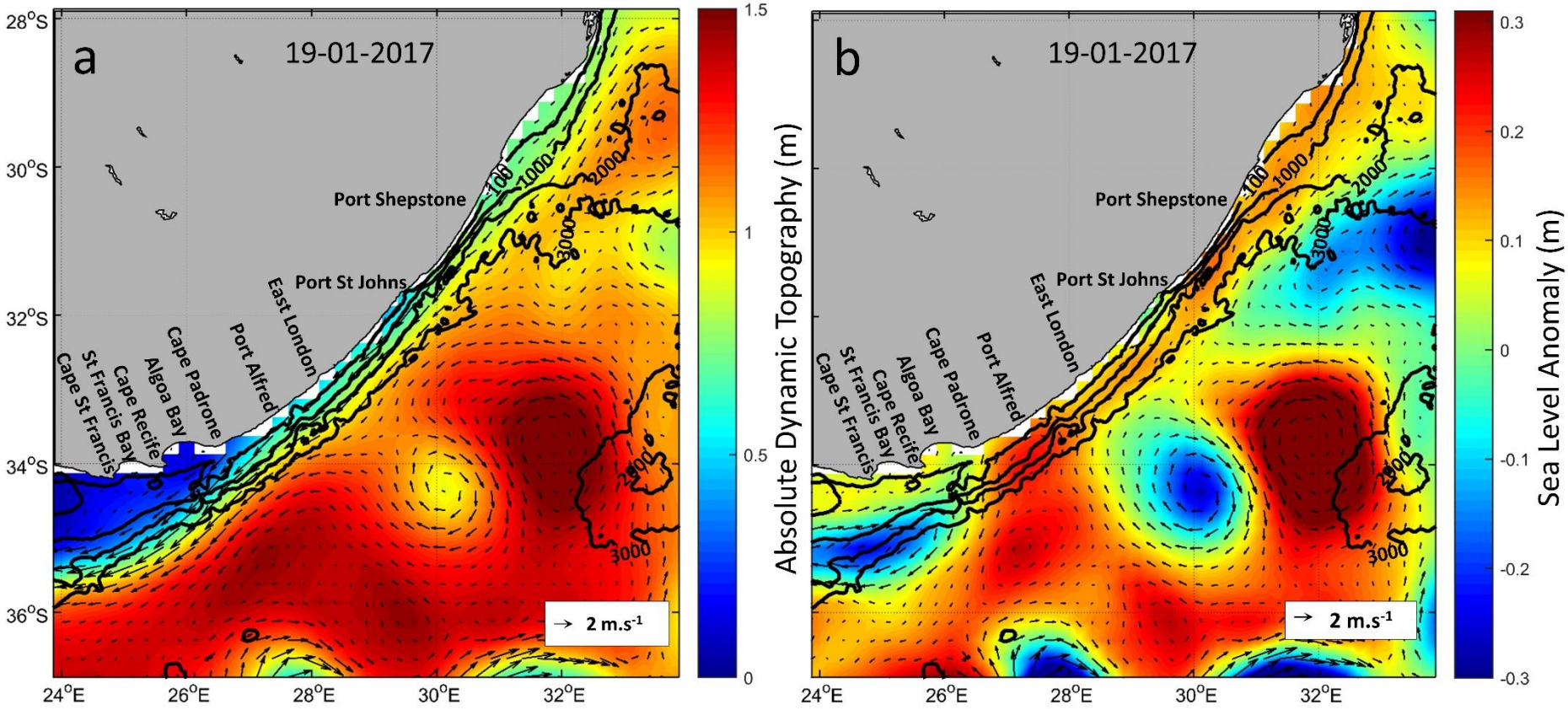

Figure 4.1 Altimetry satellite data acquired from AVISO for the 19/01/2017 overlain with bathymetric ETOPO2 contours (100, 1000, 2000, 3000 m). a.) The location of the Agulhas Current is represented by absolute dynamic topography overlain with geostrophic velocity vectors. b.) The presence of a cyclonic eddy (35°S; 24.8°E) whose core is located along the 2000 m isobath and inshore edge along the 1000 m isobath, is depicted by the sea level anomaly overlain with geostrophic velocity anomaly vectors. Note: the different scales for the ADT and SLA.

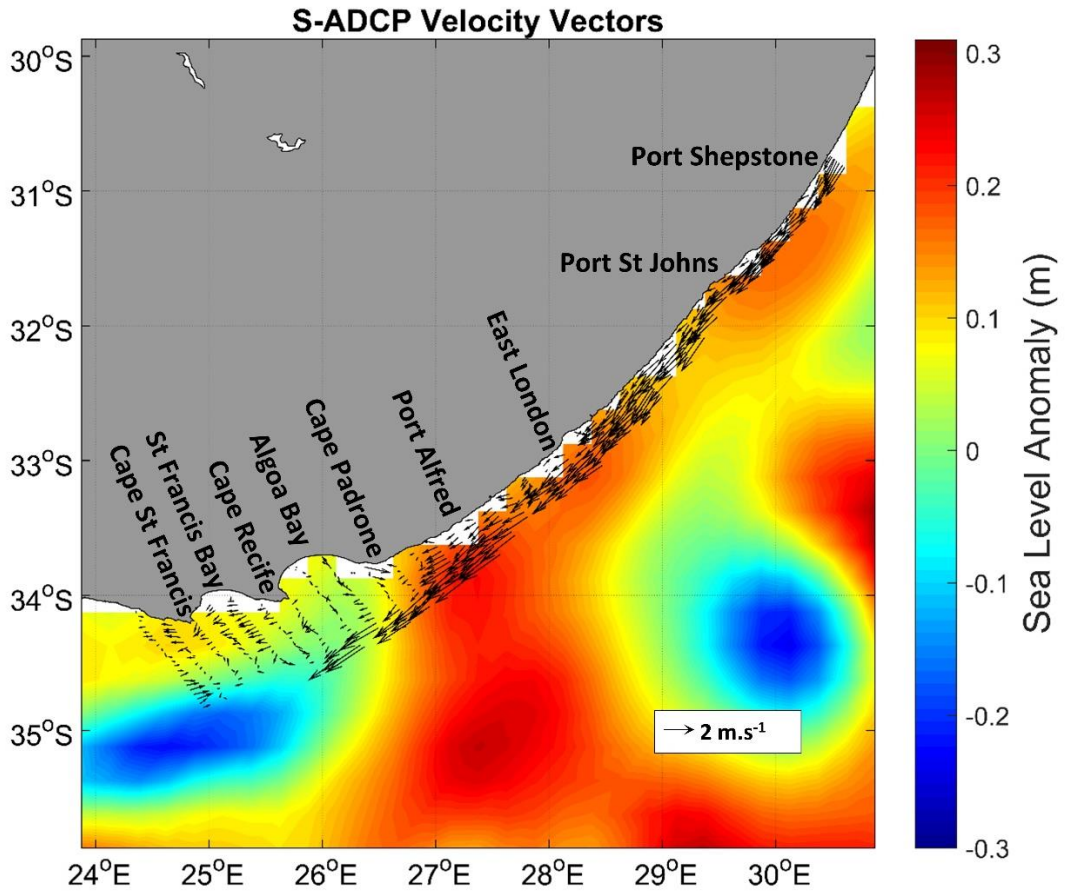

Figure 4.2 Sea level anomaly (SLA) data (19/01/2017) acquired from AVISO overlain with *in situ* shipboard-acoustic Doppler current profiler (S-ADCP) data acquired from the January/February 2017 cruise. The figure which is zoomed in for the better representation of the S-ADCP vectors, depicts good correspondence between the satellite and *in situ* data by the negative SLA and the change in S-ADCP current speed and direction, indicating the presence of a cyclonic eddy.

4.1.2 July/August 2017 – Austral Winter

A strong south-westward flow, associated with the inshore edge of the Agulhas Current, was observed in close proximity to the coastline, between Port Shepstone and East London (Figure 4.3a). Off East London, this south-westward flow (Figure 4.3a) was deflected southward from the shelf break and was found to re-establish its location against the shelf break off of Cape St Francis. The current instability depicted in Figure 4.3a, coincided with the presence of a SLA of -0.3 m (Figure 4.3b), as well as cyclonic circulation which is depicted by the clockwise orientated geostrophic velocity anomaly vector. This negative SLA accompanied by a cyclonic circulation is consistent with the presence of a cyclonic cold-core eddy (hereafter termed the July/August cyclonic eddy).

The July/August cyclonic eddy, whose core was located further offshore than the January/February cyclonic eddy, beyond the 3000 m isobath at approximately 34.8°S and 27.4°E (Figure 4.3b) and inshore edge was located along the 2000 m isobath, measured approximately 200 km (33.8°S-35.6°S) latitudinally and 310 km (26.0°E-28.8°E) longitudinally. The July/August eddy was found to originate in the KZN Bight on the 10th of May 2017 (Figure A.2). It took 77 days to travel the 546 km along the 200 m contour from Durban to Port Alfred, reaching Port Alfred on the 25th of July 2017 (Figure A.2) and therefore had a propagation speed of approximately 7.1 km/day. While the propagation speed of the July/August eddy was relatively slower than the general propagation speed of Natal Pulses (10-20 km/day; de Ruijter et al., 1999), its origin and size characteristics resemble those of a Natal Pulse. The July/August cyclonic eddy (Figure 4.3b) was both larger in size and intensity than the January/February cyclonic eddy (Figure 4.1b) but had a slower propagation speed.

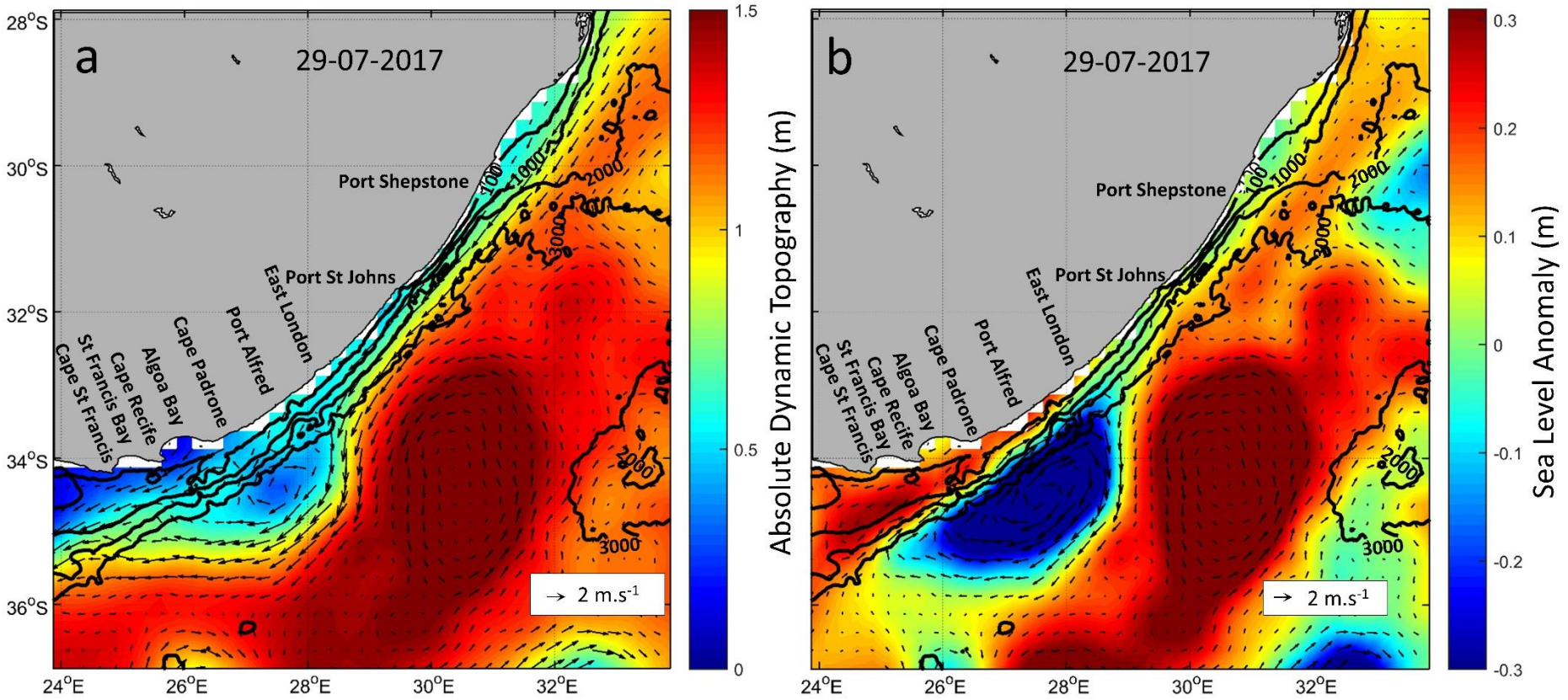

Figure 4.3 Altimetry satellite data acquired from AVISO for the 29/07/2017 overlain with bathymetric ETOPO2 contours (100, 1000, 2000, 3000 m). a.) The location of the Agulhas Current is represented by absolute dynamic topography overlain with geostrophic velocity vectors. b.) The presence of a cyclonic eddy (34.8°S; 27.4°E) whose core is located further offshore than the 3000 m isobath, is depicted by the sea level anomaly overlain with geostrophic velocity anomaly vectors. Note: the different scales for the ADT and SLA.

4.2 Distribution of Temperature and Salinity

This section will investigate and describe satellite and *in situ* temperature data as well as *in situ* salinity data. ODYSSEA sea surface temperature (SST) data acquired from the Copernicus Marine Environment Monitoring Service (CMEMS) is represented in two separate time series images. Figure 4.4 depicts the SST time series over the course of the January/February 2017 cruise, which took place during the austral summer, starting from the 05/01/2017 to the 10/02/2017. Figure 4.7 depicts the SST time series over the course of the January/February 2017 cruise which took place during the austral winter, starting from the 05/01/2017 to the 10/02/2017. The satellite time series (Figure 4.4 and Figure 4.7) were plotted on a five-day interval, with exception of Figure 4.4d which represented SST data from the 19/01/2017 and Figure 4.7e which represented data from the 29/07/2017. These two figures (Figure 4.4d and Figure 4.7e) were plotted for the same dates for which the ADT and SLA data were plotted, represented in Figure 4.1 and Figure 4.3. This was done in order to allow for a further investigation of the relationship between the mesoscale eddies, identified in section 4.1, with the SST data investigated in this section.

The *in situ* temperature and salinity data acquired during the January/February 2017 cruise are represented in Figure 4.5a-b and Figure 4.6a-b respectively. The *in situ* temperature and salinity data acquired during July/August 2017 cruise are represented in Figure 4.5c-d and Figure 4.6c-d respectively. The upper panels of both Figure 4.5 and Figure 4.6 represent the surface values and the lower panels represent the bottom sampled values. The surface values depicted in both figures represent data captured within 3 to 5 m of the sea surface which was swell-dependant as well as to ensure that the CTD would not sample air. The bottom values, depicted in both figures, represent data captured within 1 m to 5 m from the sea floor to ensure that the CTD would not hit the bottom and sample sediment. If rough weather persisted at the time of sampling, the distance from the sea floor would increase.

4.2.1 January/February 2017 – Austral Summer

Satellite observations over the period of the January/February 2017 cruise depict a north-south negative temperature gradient which can be seen in Figure 4.4a-i. The relatively high SST's, represented by the 24 ^{o}C isotherm (Figure 4.4a-i) can be said to be a visual and qualitative indicator for the position of the inshore edge of the Agulhas Current. A good representation of this can be seen with the comparison of Figure 4.4d and Figure 4.1a, in which the increasing velocity gradients on the

shoreward side of the Agulhas Current's path (Figure 4.1a) can be seen to coincide with the position of the 24 ºC isotherm (Figure 4.4d). The maximum SST recorded over this time was between 28-29 ºC (Figure 4.4h-i) and the minimum SST was between 19-20 ºC (Figure 4.4d and f-g). The relatively low SSTs (below 23 ºC) along the inshore edge of the Agulhas Current are representative of the divergence-induced upwelling as a result of the offshore deflection of the current from the coast near East London (~33 ºS; Figure 4.4a-i). The lowest SST's (< 20 °C) represented in Figure 4.4d specifically, coincide with the position of the January/February cyclonic eddy, represented by the negative SLA, in Figure 4.1b, confirming that the January/February cyclonic eddy indeed has a cold-core and is associated with upwelling of cold water.

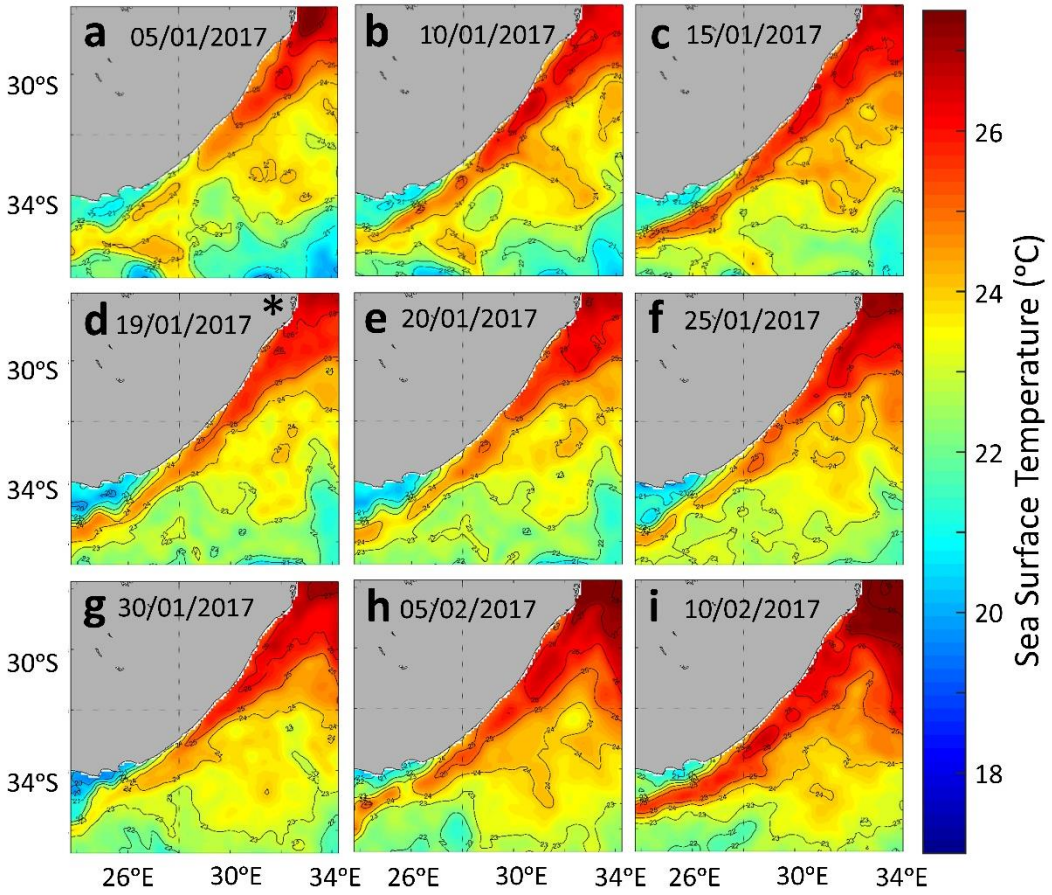

Figure 4.4 Time series of daily satellite ODYSSEA sea surface temperature (SST) (ºC) for January/February 2017. The * represents SSTs for the 19/01/2017, the date used to plot the altimetry data in Figure 4.1.

The analysis of the *in situ* surface temperature data, represented in Figure 4.5a, reveals similar patterns to those which were observed in the satellite SST data (Figure 4.4a-i). Figure 4.5a reveals a similar north-south orientated negative temperature gradient to that which was observed in the satellite SST data (Figure 4.4a-i). Similar

to the satellite SST temperature, the *in situ* surface temperatures were also observed to increase in an offshore direction (Figure 4.5a). The surface temperatures observed during January/February, ranged from 10.7 to 26 ^{o}C (Figure 4.5a). The low surface temperature of 10.7 ^{o}C, observed in the *in situ* surface temperature data (Figure 4.5a), was not observed in the satellite SST data due to the coarser resolution of the satellite data.

In situ surface temperatures of 24 ^{o}C and higher were observed in close proximity to the coast between East London and Port Shepstone (Figure 4.5a), which is similarly seen in the satellite SST data (Figure 4.4a-i). Southwest of East London, relatively low surface temperatures (<23 ^{o}C) were observed inshore and relatively high surface temperatures (>23 ^{o}C) were observed further offshore (Figure 4.5a) all of which was also represented in the satellite SST data (Figure 4.4a-i). The position of the inshore edge of the Agulhas Current presented *in situ* data, is represented by the 24 ^{o}C isotherm in Figure 4.5a, which is similarly seen in the satellite data (Figure 4.4a-i). The southward deviation of the 24 ^{o}C isotherm observed offshore of Cape Padrone, is as a result of the position and clockwise circulation of the January/February cyclonic eddy, depicted by the negative SLA and cyclonic circulation (Figure 4.1b) and by the S-ADCP data (Figure 4.2).

Low temperatures of 18 ^{o}C and less were observed inshore between Cape St Francis and Port Alfred and were concentrated at three distinct sites which are labelled as Sites A, Site B and Site C in Figure 4.5a. The first site (Site A) was located just west of Cape Recife, where a surface temperature minimum of 10.7 ^{o}C was observed close inshore. The second site (Site B) was located just south west of Cape Padrone where a surface temperature of 15.3 ^{o}C was observed in the mid-shelf region. The third last site (Site C) was located at Port Alfred where a surface temperature of 15.3 ^{o}C was observed close inshore. While cooling was observed in the satellite SST data (Figure 4.5a), the low temperatures observed at sites A, B and C in the *in situ* data (Figure 4.5a) were not observed in the satellite SST data (Figure A.3), most probably as a result of the coarser resolution of the satellite data.

The surface salinities observed during January/February ranged from 33.7 to 35.5 g/kg (Figure 4.6a). As can be seen in Figure 4.6a, the majority of the surface salinities observed throughout the study area were above 35.2 g/kg, displaying a high degree of homogeneity, with the exception of two distinct coastal sites which are delineated by the 35.1 g/kg isohaline. A low surface salinity of 34.8 g/kg was observed at Site A coinciding with the surface temperature minimum of 10.7 ^{o}C (Figure 4.5a and Figure

4.6a). The second low salinity site (Site D) was located at mouth of the Mzimvubu River where the surface salinity minimum of 33.7 g/kg was observed.

The bottom temperatures ranged from 6 to 24.5 ^{o}C (Figure 4.5b). A general pattern regarding bottom temperature is revealed in Figure 4.5b, which demonstrates an inshore-offshore orientated decreasing temperature gradient. As expected from the general observed pattern, relatively high bottom temperatures, greater than 20 ^{o}C, were observed inshore along the coast from just east of East London to Port Shepstone but due to the scale of Figure 4.5b, this is not easily observed in this figure. As illustrated in Figure 4.5b, the lowest bottom temperatures, ranging between 6 and 10 ^{o}C, were observed in patches offshore between Cape Padrone and Port Shepstone. However, between Algoa Bay and Cape St Francis, these low temperatures were observed in close proximity to the coast as depicted by the 10 ^{o}C isotherm (Figure 4.5b).

The bottom salinities ranged from 34.5 to 35.5 g/kg and although this range is smaller than the surface salinity range, a greater degree of spatial variability is seen in Figure 4.6b. As illustrated in Figure 4.6b, the general bottom salinity gradient, like the bottom temperature gradient, was negative and had an inshore-offshore orientation. Salinities lower than 34.9 g/kg were observed offshore in patches, coinciding with the low temperature patches, located between Cape Padrone and Port Shepstone (Figure 4.6b). Coinciding with the large region of low temperature on the shelf observed between Algoa Bay and Cape St Francis, was a large area of low salinity, located in close proximity to the coast, depicted by the 34.9 g/kg isohaline (Figure 4.6b).

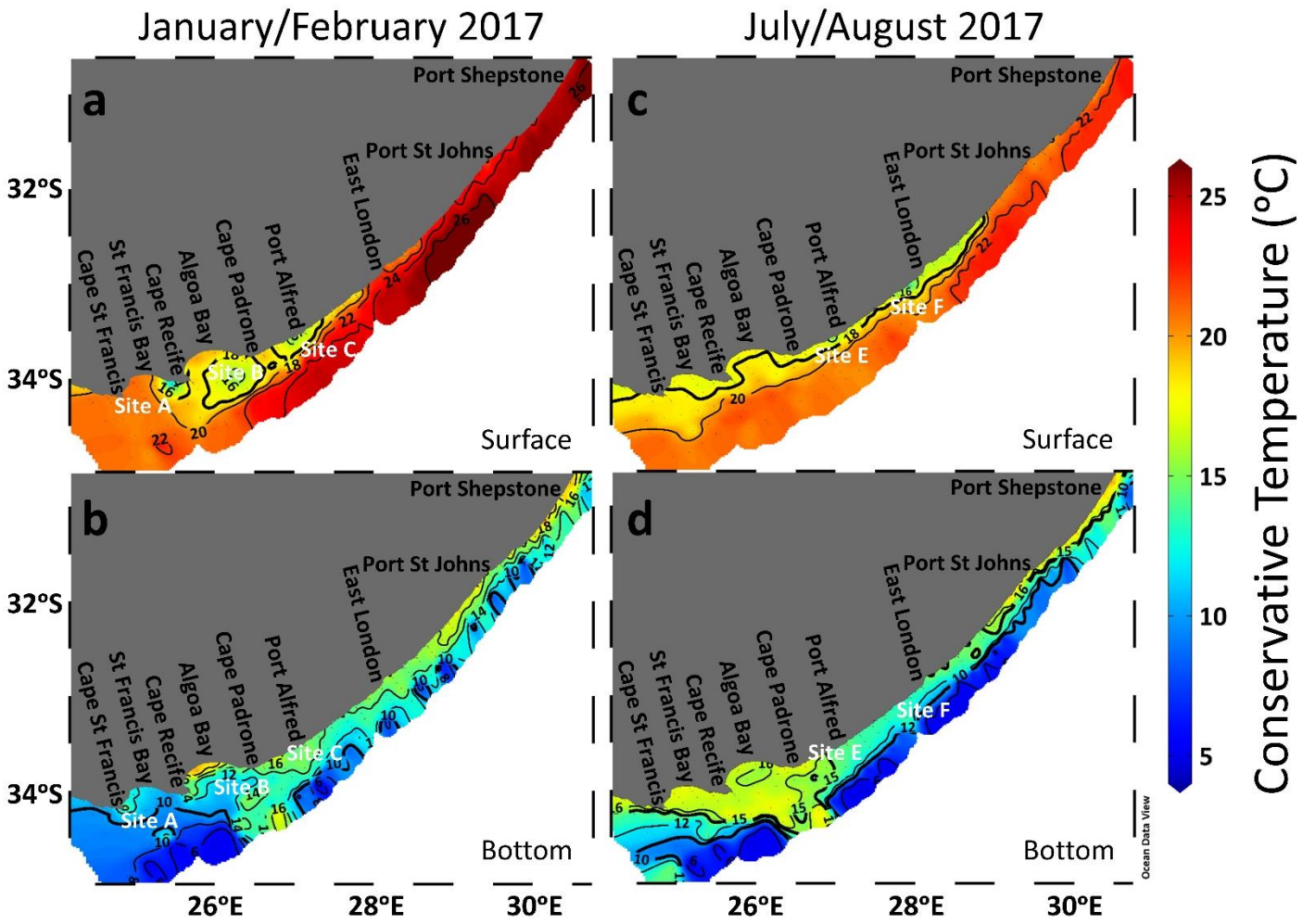

Figure 4.5 *In situ* surface and bottom conservative temperature maps for January/February (a-b) and July/August (c-d) 2017 highlighting five sites of upwelling labelled site A, B, C, E and F.

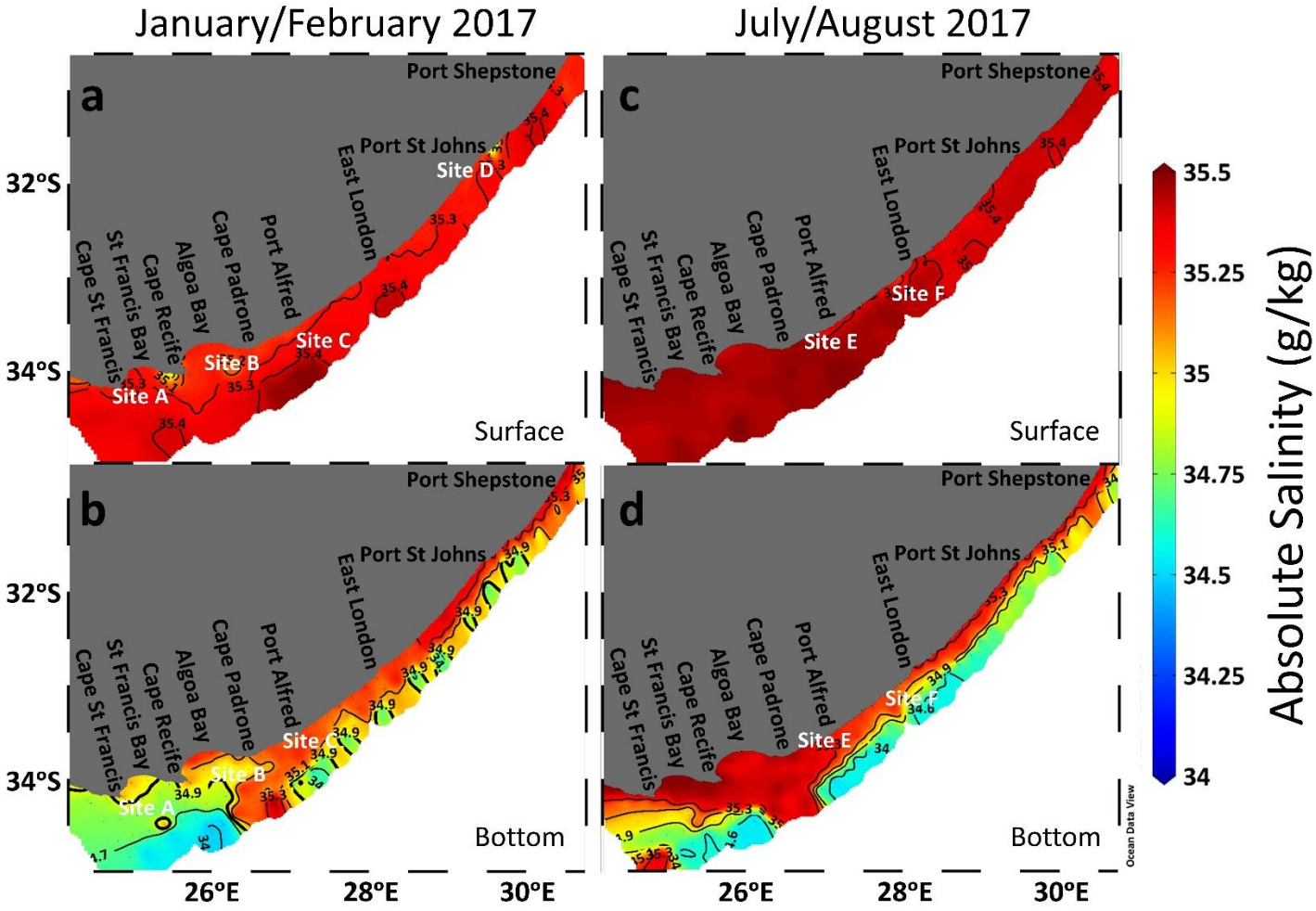

Figure 4.6 *In situ* surface and bottom absolute salinity maps for January/February (a-b) and July/August (c-d) 2017, highlighting two sites of low salinity labelled site A (upwelling) and D (river influence). Low temperature sites (A, B, C, E and F) from Figure 4.5 are labelled.

4.2.2 July/August 2017 – Austral Winter

A north-south negative temperature gradient, similar to that which was observed in the January/February 2017 satellite SST data (Figure 4.4a-i), was also observed in the July/August 2017 satellite SST data (Figure 4.7a-i). The maximum SSTs recorded over this time were between 23-24 °C (Figure 4.7a and i) which is 5 °C lower than the maximum January/February satellite SSTs (Figure 4.4h-i). The minimum SSTs were observed to be between 17-18 °C (Figure 4.7a-i) which are also lower than the minimum January/February satellite SSTs (Figure 4.4d and f-g).

During July/August, the position of the inshore edge of the Agulhas Current edge is qualitatively established by the location of the 22 °C isotherm (Figure 4.7a-i), which coincided with relatively high horizontal velocity gradients on the shoreward side of the Agulhas Current's path (Figure 4.3a). The decision was made to use of 22 °C isotherm, as opposed to the 24 °C which is used in January/February (Figure 4.4a-i), due to the presence of relatively lower SSTs which were observed during July/August (Figure 4.7a-i) than in January/February (Figure 4.4a-i). The relatively high SSTs (> 22 °C) presented in Figure 4.7e coincide with the position of the Agulhas Current represented by the relatively high ADT, as well as the south-westward geostrophic velocity vectors seen in Figure 4.3a.

The presence of the July/August cyclonic eddy, like that of the January/February cyclonic eddy, is observed in the satellite SST data (Figure 4.7e). The low SSTs observed in Figure 4.7e specifically, coincide with the position of the core of the July/August cyclonic eddy, represented by the negative SLA and clockwise orientated geostrophic velocity anomaly vectors, seen in Figure 4.3b. On the 29/07/2017, relatively high SSTs (23-24 °C), representative of the Agulhas Current, located at 26 °E, were observed to have been directed inshore (Figure 4.7e) which coincides with the position of the outer edge of the July/August cyclonic eddy (Figure 4.3b). Similar to what was observed in January/February (Figure 4.4a-i), relatively lower SST's (below 21 °C) are depicted along the inshore edge of the Agulhas Current from between Port St Johns and East London (Figure 4.7a-i), representing the divergence-induced upwelling as a result of the offshore deflection of the Agulhas Current.

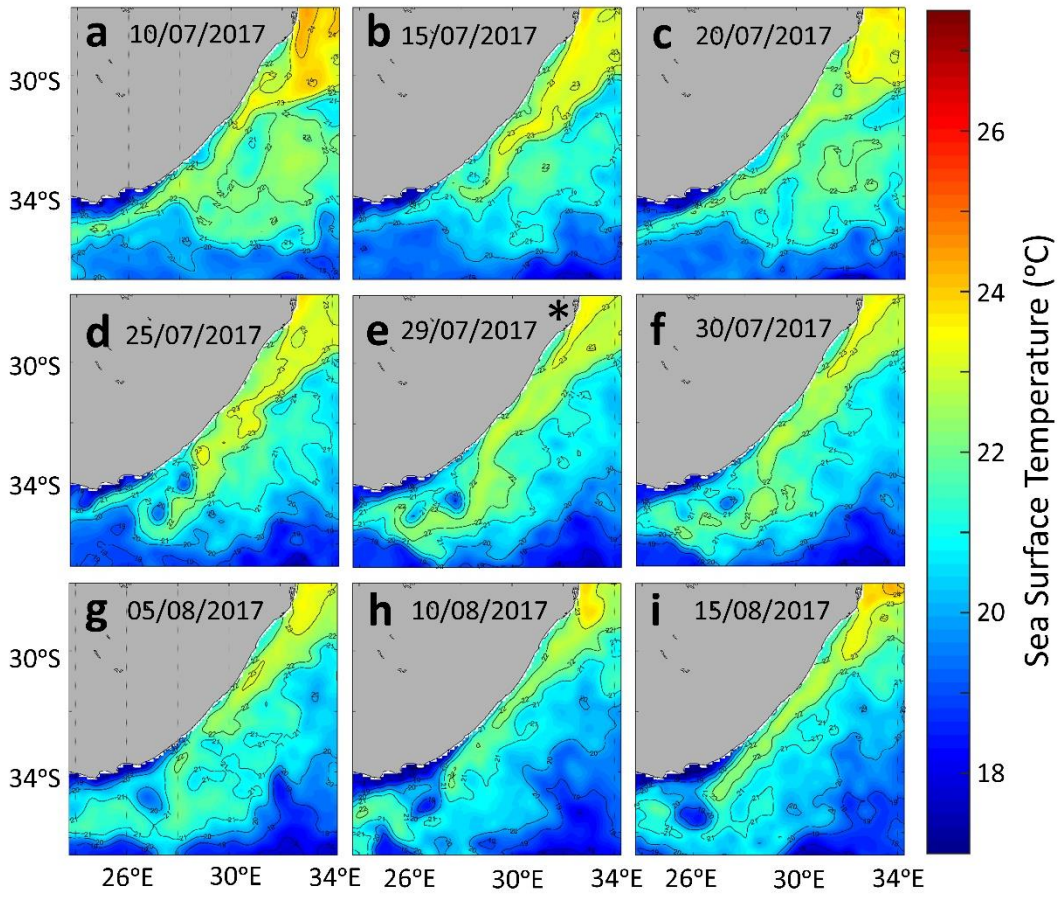

Figure 4.7 Time series of daily satellite ODYSSEA sea surface temperature (SST) (°C) for July/August 2017. The * represents SSTs for the 29/07/2017, the date used to plot the altimetry data in Figure 4.3.

The analysis of the *in situ* surface temperature data, represented in Figure 4.5c, reveals similar surface patterns to those which were observed in the satellite SST data, represented in Figure 4.7a-i. The *in situ* surface temperatures during July/August ranged from 13 to 23 °C (Figure 4.5c). The maximum *in situ* surface temperature (Figure 4.5c) is similar to maximum satellite SST (Figure 4.7a and i) observed during July/August. The minimum *in situ* surface temperature (Figure 4.5c) was 4 °C lower than the minimum satellite SST (Figure 4.7a-i). The maximum *in situ* surface temperatures observed in July/August (Figure 4.5c) were 4 °C lower than the maximum *in situ* surface temperatures observed in January/February (Figure 4.5a).

The *in situ* surface temperature pattern observed in July/August (Figure 4.5c), was similar to that which was observed in January/February (Figure 4.5a), such that the surface temperatures increased in an offshore direction. This same pattern is observed in the satellite SST data for July/August (Figure 4.7a-i). As can be seen in Figure 4.5c, the highest *in situ* surface temperatures, between 22 and 23 °C, were observed offshore between East London and Port Shepstone only. The offshore

stations to the west of East London portrayed temperatures between 20 and 22 °C (Figure 4.5b). Lower temperatures observed inshore are depicted by the 18 °C isotherm which is seen hugging the coastline from Cape St Francis to just east of East London (Figure 4.5b) which is similarly seen in the satellite SST data for July/August (Figure 4.7a-i). Bound between the coast and the 18 °C isotherm are two sites at which the lowest *in situ* surface temperatures were observed (Figure 4.5b). The locations of the lowest *in situ* surface temperature during July/August were different to the locations of the lowest *in situ* surface temperature during January/February, except for the site at Port Alfred. As can be seen in Figure 4.5b, the first site (Site E) was located at Port Alfred and was observed to have an *in situ* surface temperature of 14.5 °C. The second site (Site F) was located just west of East London and was observed to have the lowest *in situ* surface temperature (13.7 °C) for July/August (Figure 4.5b). As a result of the coarser resolution of the satellite SST data, the low *in situ* surface temperatures observed at sites E and F (Figure 4.5b) were not observed in the satellite SST data (Figure 4.7a-i).

The surface salinity ranged from 35.2 to 35.5 g/kg – a considerably smaller range than that observed in January/February (Figure 4.6a and c). The surface salinity for the majority of the study region ranged between 35.4 and 35.5 g/kg, which resulted in a low degree of spatial variability and no distinguishable general pattern (Figure 4.6c). Bound between the 35.4 g/kg isohaline and the coast are two sites at which the lowest surface salinities were observed (Figure 4.6c). A salinity of 35.3 g/kg, which coincided with a low surface temperature of 14.5 °C, was observed at the first site – Site E (Figure 4.5c and Figure 4.6c). The lowest surface salinity of 35.2 g/kg was observed at Site E and coincided with the lowest surface temperature of 13.7 °C (Figure 4.5c and Figure 4.6c).

The bottom temperatures ranged from 4.25 to 20.5 °C (Figure 4.5d). Figure 4.5d revealed an inshore-offshore orientated decreasing bottom temperature gradient, similar to that which was observed in January/February (Figure 4.5b). Relatively high bottom temperatures above 16 °C were observed inshore along the coast, from Cape St Francis to just west of Port Alfred and from just east of East London to Port Shepstone (Figure 4.5d). Between Cape St Francis and Port Alfred, the temperatures above 16 °C were also observed to extend offshore toward the position of the 1000 m isobath (Figure 4.5d). Between Port Alfred and East London, temperatures of 15 °C and less were observed inshore, as indicated by the 15 °C isotherm in Figure 4.5d. The lowest bottom temperature of 4.25 °C was observed offshore of East

London (Figure 4.5d). As depicted by the 10 ^{o}C isotherm in Figure 4.5d, low bottom temperatures were observed offshore throughout the length of the coast. Unlike the January/February cruise (Figure 4.5b), these low temperatures of 10 ^{o}C and less, did not extend far inshore during July/August (Figure 4.5d).

The bottom salinity ranged from 34.49 to 35.50 g/kg (Figure 4.6d). Similar to what was observed in January/February, a larger spatial variability was observed in the bottom salinities as opposed to the surface salinities (Figure 4.6a-d). The higher salinities were observed inshore and the lower salinities were observed offshore which resulted in an inshore-offshore orientated decreasing salinity gradient (Figure 4.6d). As seen in Figure 4.6d, the highest bottom salinities were observed inshore between Cape St Francis and Port Alfred. In contrast to January/February, relatively higher salinities were observed inshore between Port Alfred and Port St Johns, depicted by the 35.3 g/kg isohaline. The majority of the offshore stations presented salinities lower than 34.6 g/kg with the exception of those located offshore of Algoa Bay and just west of Cape St Francis which presented relatively high salinities above 35.3 g/kg (Figure 4.6d).

4.3 Water Masses

Temperature-Salinity (TS) plots for both the January/February and July/August cruises are shown in Figure 4.8a-b and Figure 4.9. With the aid of the physical properties of water masses outlined in *Table 2.1*, the same five water masses were identified in both January/February (Figure 4.8a) and July/August (Figure 4.8b). In order of ascending neutral densities, these five water masses are Tropical Surface Water (TSW), Subtropical Surface Water (STSW), South Indian Central Water (SICW), Antarctic Intermediate Water (AAIW) and Red Sea Water (RSW). When comparing the two cruises, five distinguishable characteristics presented themselves (see Figure 4.8a-b and Figure 4.9).

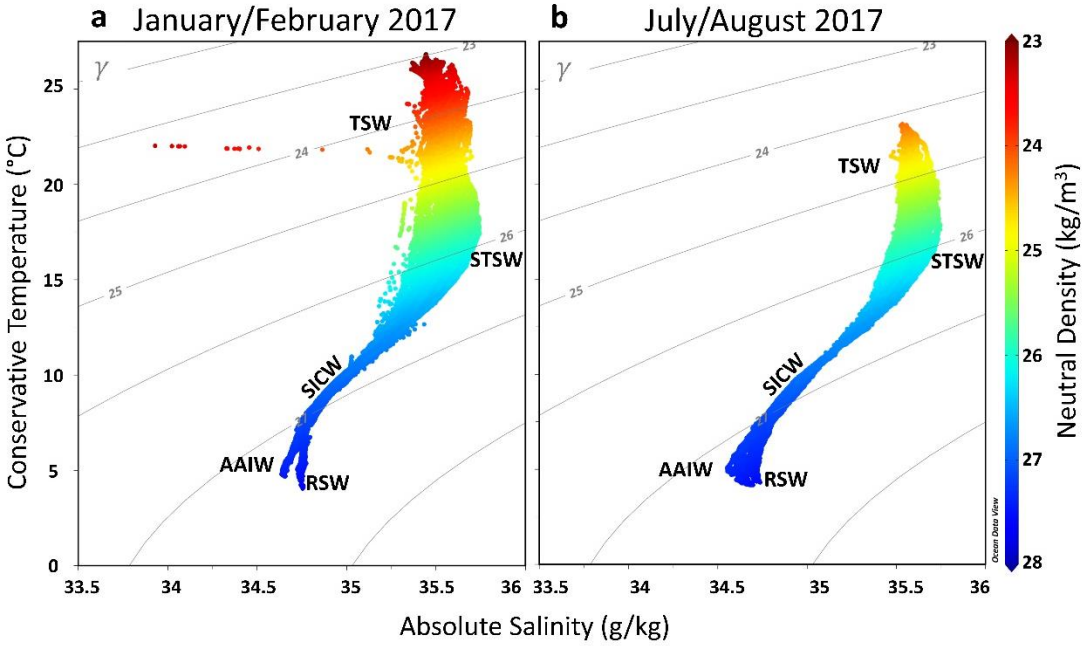

Figure 4.8 *In situ* Temperature-Salinity plots for the a.) January/February and b.) July/August 2017 with neutral density as shown by the colour bar and contours. The same five water masses were observed in each cruise and they were: Tropical Surface Water (TSW), Subtropical Surface Water (STSW), South Indian Central Water (SICW), Antarctic Intermediate Water (AAIW) and Red Sea Water (RSW). Note that the low salinities of 33.7 g/kg represents the influence of river outflow which was interestingly only observed during the austral summer (January/February 2017).

The first characteristic is the approximate 4 °C difference in the temperature maxima between January/February and July/August observed within the TSW layer. Accompanying the higher temperature maximum observed in January/February, is the larger temperature range of the TSW. As can be seen in Figure 4.8a-b and Figure 4.9, the temperature range of the TSW extends from approximately 17.5 to 26.8 °C,

whereas during July/August the TSW temperature range extends from 17.5 to 23.1 ^{o}C.

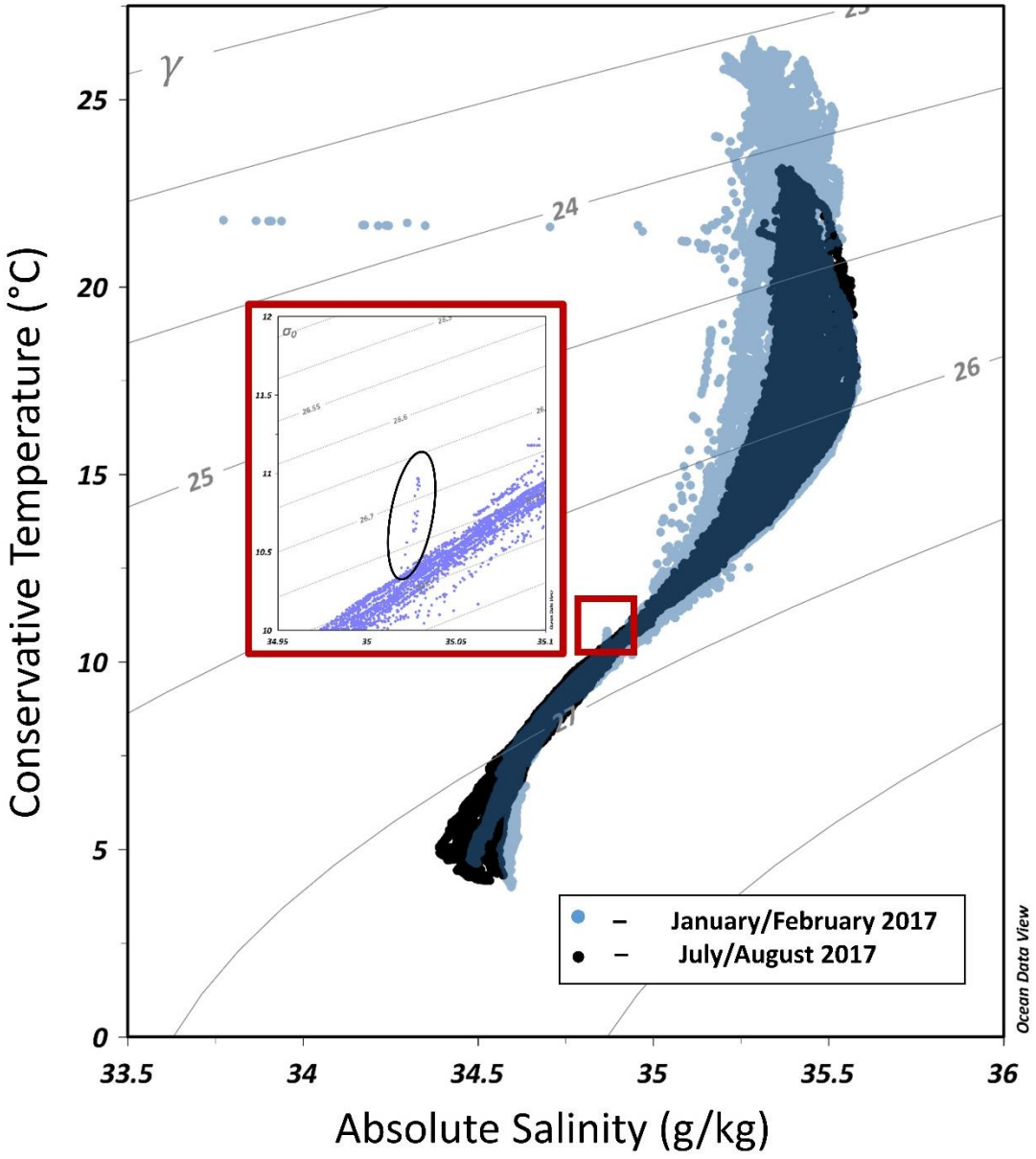

Figure 4.9 Temperature-Salinity plot presenting a comparison of the *in situ* data collected during the January/February (represented by the blue dots) and July/August (represented by the black dots) 2017 cruises. The 33.7 g/kg salinity minimum represents river influence. The zoom inset of the vertically orientated data points represents the wind-driven upwelling of South Indian Central Water at site A.

The second characteristic is the difference in salinity ranges observed between the January/February and July/August cruises (Figure 4.8a-b and Figure 4.9). The salinity data for the TSW and the STSW, observed in July/August, was found to be confined to a relatively small salinity range (35.15 to 35.5 g/kg) and subsequently appears more condensed on the TS plot (Figure 4.8a-b and Figure 4.9). In contrast to this, the

January/February data appears to be more spread across its larger salinity range (35 to 35.5 g/kg) on the TS plot (Figure 4.8a-b and Figure 4.9). The 33.7 g/kg salinity minimum observed within the TSW was purposefully disregarded here as it will be further discussed below (Figure 4.8a-b and Figure 4.9).

The third characteristic, further investigated in section 4.9, is the anomalously low salinity minimum of 33.7 g/kg, which was observed at one station within the TSW layer in January/February (Figure 4.8a and Figure 4.9). This salinity minimum corresponds with the surface salinity minimum observed in Figure 4.6a at the inshore station at Site D (the Mzimvubu River mouth at Port St Johns). If the salinity minimum anomaly of January/February 2017 were to be overlooked, then the salinity minima observed during January/February and July/August 2017 would be 34.49 and 34.39 g/kg respectively and they both would be located within the AAIW layer (seen in Figure 4.8a-b and Figure 4.9).

The fourth characteristic is notably smaller than the three previously mentioned characteristics and is easily overlooked. The vertically orientated data points, highlighted in Figure 4.9, were observed during the January/February 2017 cruise within the SICW and are indicative of upwelling. This is the upwelling that was found to occur at site A which is further investigated in case study 3 in section 4.8.

The fifth and final distinguishable characteristic, further investigated in section 4.7, is the pronounced separation of the AAIW and RSW in January/February, which is depicted by the explicit partitioning of the AAIW and the RSW in Figure 4.8a and Figure 4.9. Contrastingly, during July/August, greater mixing between AAIW and RSW was observed which is depicted by the spread of data between AAIW and RSW in Figure 4.8b and Figure 4.9. The differentiation of RSW and AAIW was confirmed by dissolved oxygen (DO) concentrations, discussed further in case study 2 in section 4.7.

4.4 Distribution of Nutrients

Nitrate, silicate, phosphate and nitrite are four of the principal nutrients utilised by phytoplankton in the ocean (Talley, 2013). These nutrients have been found to vary inversely with regards to dissolved oxygen concentrations (DO), particularly within the upper and mid-oceanic layers (Talley, 2013). An idea of the nutrient distribution throughout the study area combined with dissolved oxygen (DO) and chlorophyll-a

(chl-a) concentrations will assist in investigating the biological response to the physical process occurring on the southeast African shelf and slope.

The nutrient data, acquired during the January/February and July/August 2017 cruises, have been used to investigate the changes in concentration and distribution of the four main nutrients: silicate, nitrate, phosphate and nitrite. The surface and bottom nutrient concentrations for both the January/February and July/August 2017 cruises are represented in Figure 4.10a-d, Figure 4.11a-d, Figure 4.12a-d and Figure 4.13a-d. The nutrient concentrations with regards to the water masses, previously identified in section 4.3, are also investigated in this section and are represented by nutrient concentration versus neutral density plots in Figure 4.14a-d (January/February) and Figure 4.15a-d (July/August).

4.4.1 January/February 2017 – Austral Summer

Silicate had the largest concentration range from 0 to 60 μM (Figure 4.10a-b). Nitrate had the second largest concentration range which was from 0 to 37 μM (Figure 4.11a-b), and this was followed by phosphate, which had a concentration range from 0 to 2.4 μM (Figure 4.12a-b). Nitrite was observed to have the smallest concentration range from 0.05 to 0.8 μM (Figure 4.13a-b).

The surface concentrations of all four of the nutrients were found to be considerably lower than their corresponding bottom concentrations (see Figure 4.10a-b, Figure 4.11a-b, Figure 4.12a-b and Figure 4.13a-b). Taking into account the different scales used to illustrate the concentrations of all of the nutrients, little spatial variability was observed at the surface, while greater spatial variability was observed at the bottom (see Figure 4.10a-b, Figure 4.11a-b, Figure 4.12a-b and Figure 4.13a-b).The surface concentrations for all of the nutrients except for nitrite were observed to be relatively higher at sites A, C, off Cape Padrone as well as just south of site A (Figure 4.10a, Figure 4.11a, Figure 4.12a and Figure 4.13a). Relatively high surface concentrations of nitrite, between 0.4 and 0.7 μM, were observed at site A, while moderate concentrations between 0.2 and 0.4 μM were observed at sites B and C (Figure 4.13a).

The bottom silicate, phosphate and nitrate concentrations were observed to increase offshore (Figure 4.10b, Figure 4.11b and Figure 4.12b), while the bottom nitrite concentrations were observed to be elevated inshore, across the shelf between just west of Cape St Francis and Cape Padrone (Figure 4.13b). Elevated bottom concentrations for all nutrients (Figure 4.10b, Figure 4.11b, Figure 4.12b and Figure

4.13b) were observed to coincide with the position of the January/February cyclonic eddy (Figure 4.1b) and low bottom water temperature (Figure 4.5b) and salinity Figure 4.6b.

4.4.2 July/August 2017 – Austral Winter

As was similarly seen in January/February, silicate was identified as having the largest concentration range, from 0 to 59 µM (Figure 4.10c-d), which was followed by nitrate with a concentration range from 0 to 36 µM (Figure 4.11c-d). Phosphate concentrations ranged from 0 to 2.4 µM (Figure 4.12c-d) and was followed by nitrite which was found to have the smallest concentration range from 0.05 to 0.8 µM (Figure 4.13c-d). As indicated above, the nutrient concentration ranges observed during the January/February and July/August 2017 cruises were very similar but the spatial distribution patterns differ slightly (Figure 4.10a-d, Figure 4.11a-d, Figure 4.12a-d and Figure 4.13a-d).

The majority of the surface nutrient concentrations for all four of the nutrients, throughout the July/August cruise, were observed to be very low with the exception of a few areas (Figure 4.10c, Figure 4.11c, Figure 4.12c and Figure 4.13c). Silicate and nitrate display similar surface concentration patterns (Figure 4.10c and Figure 4.11c) of relatively high surface concentrations, between 5 and 10 µM, just west of Cape Padrone as well as at Site F. Relatively high surface phosphate concentrations, between 0.5 and 0.75 µM, were observed at sites E and F (Figure 4.12c), while relatively high surface nitrite concentrations, between 0.2 and 0.4 µM, were observed west of Cape St Francis, around Cape Recife as well as between Cape Padrone and Port Alfred (Figure 4.13c). Similar to what was observed during the January/February 2017 cruise, the surface nutrient concentrations were observed to be considerably lower than the bottom nutrient concentrations (Figure 4.10a-d, and Figure 4.11a-d, Figure 4.12a-d and Figure 4.13a-d).

The bottom silicate, nitrate and phosphate concentrations were observed to increase offshore while the bottom nitrite concentration was observed to be higher inshore, specifically between just west of Cape St Francis and East London, and decrease offshore (Figure 4.10d, and Figure 4.11d, Figure 4.12d and Figure 4.13d).

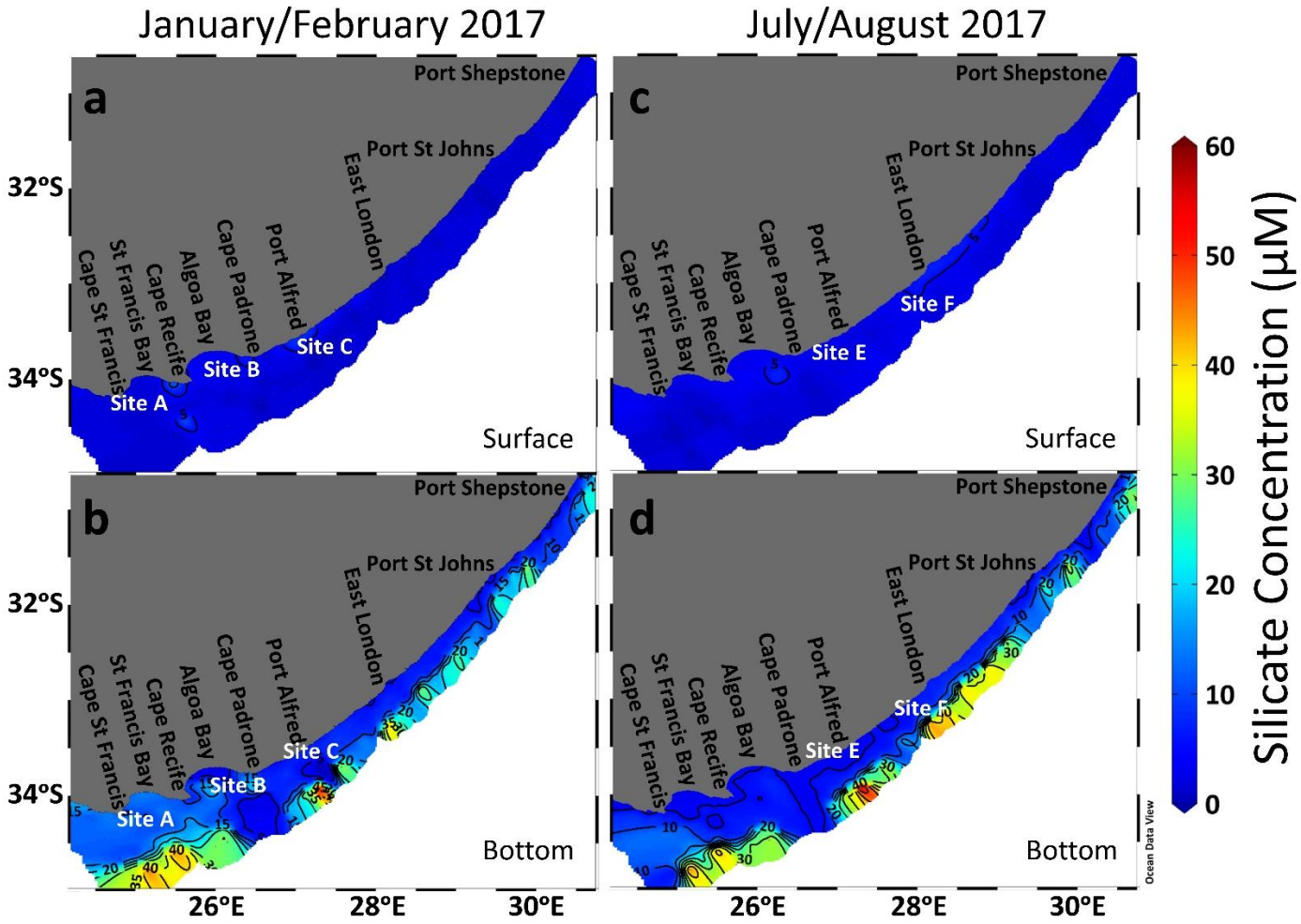

Figure 4.10 Surface and bottom micromolar concentration maps of silicate for January/February (a-b) and July/August (c-d) 2017 depicting low concentrations in the surface and bottom waters on the shelf and high concentrations in the slope waters.

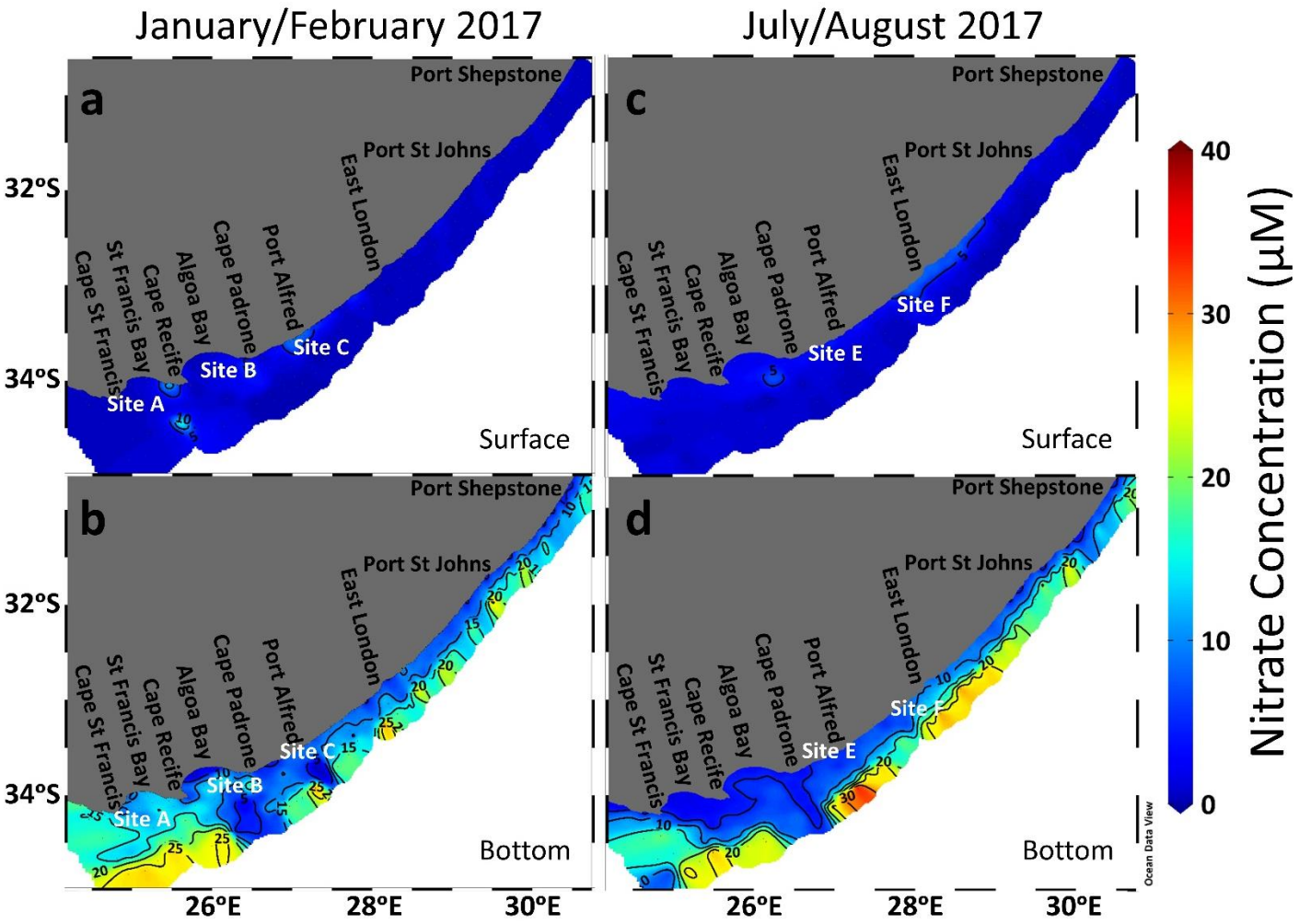

Figure 4.11 Surface and bottom micromolar concentration maps of nitrate for January/February (a-b) and July/August (c-d) 2017 depicting low concentrations in the surface and bottom waters on the shelf and high concentrations in the slope waters.

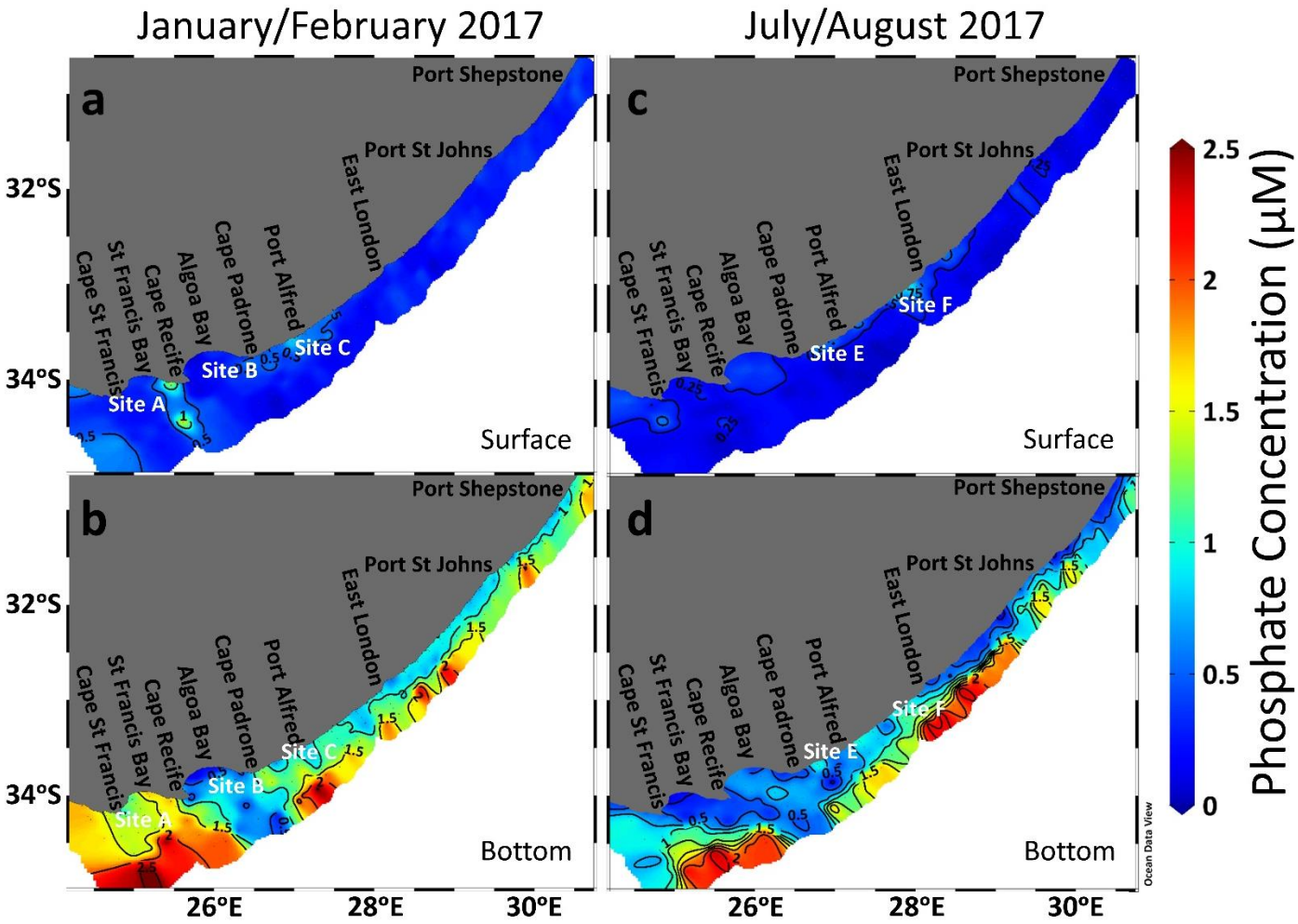

Figure 4.12 Surface and bottom micromolar concentration maps of phosphate for January/February (a-b) and July/August (c-d) 2017 depicting low concentrations in the surface and bottom waters on the shelf and high concentrations in the slope waters.

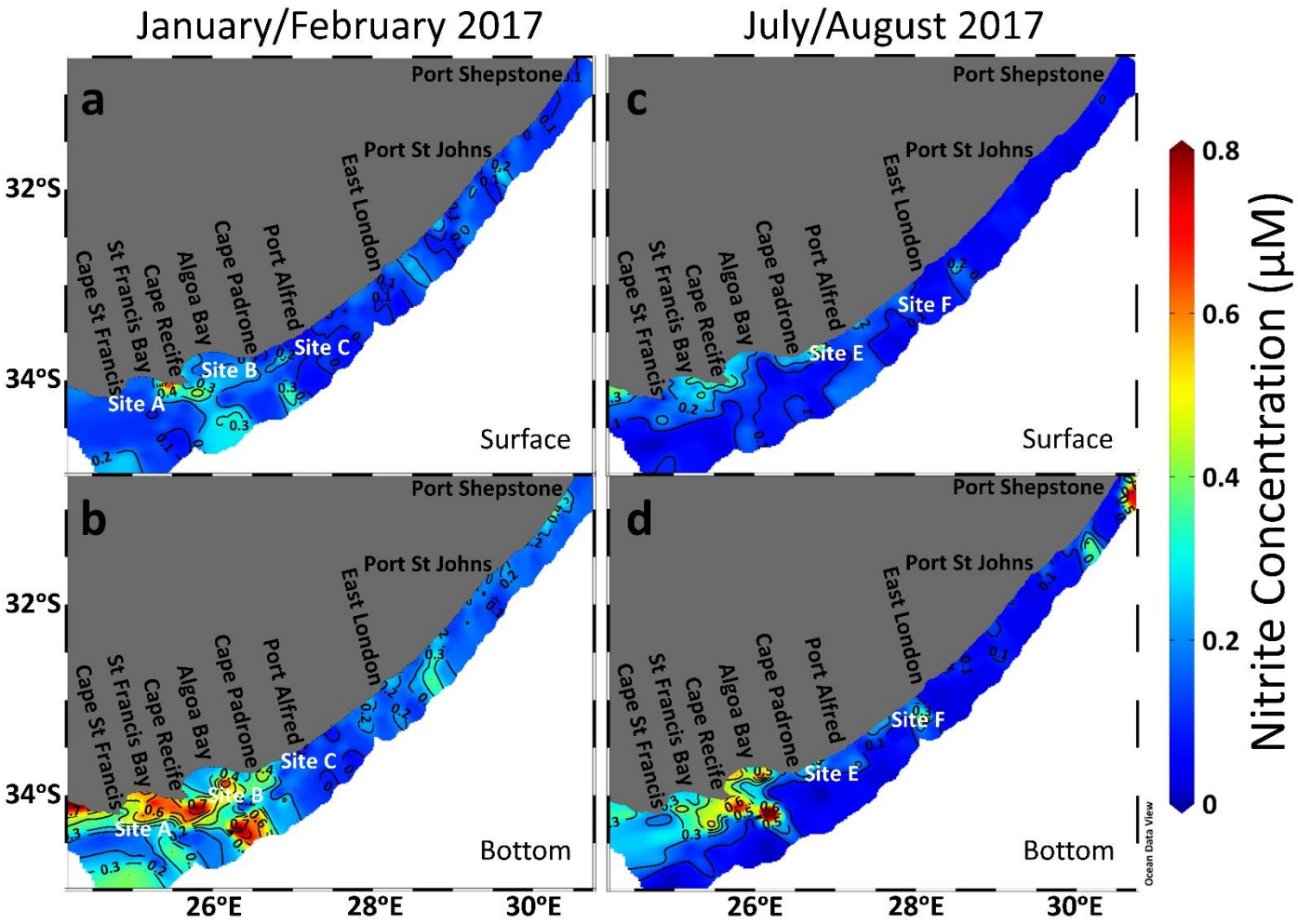

Figure 4.13 Surface and bottom micromolar concentration maps of nitrite for January/February (a-b) and July/August (c-d) 2017 depicting low concentrations at the surface and along the slope and high concentrations in the bottom waters on the shelf.

4.4.3 Nutrient Concentration of Water Masses

The nutrient concentration data acquired from the January/February and July/August 2017 cruises, plotted against neutral density, represented in Figure 4.14a-d and Figure 4.15a-d, revealed that the five water masses identified in section 4.3, had different nutrient concentrations which were found to vary slightly between the two cruises.

The nutrient concentrations for the water masses identified during the January/February 2017 cruise are described below. TSW was observed to contain between 0 and 9 µM of silicate and nitrate (Figure 4.14a and c), between 0 and 1.5 µM of phosphate (Figure 4.14b) and between 0.05 and 0.7 µM of nitrite (Figure 4.14d). STSW was observed to contain between 0 and 13 µM of silicate (Figure 4.14a), between 0 and 14 µM of nitrate (Figure 4.14c), between 0.1 and 1.75 µM of phosphate (Figure 4.14b) and 0.05 and 0.7 µM of nitrite (Figure 4.14d). SICW was observed to contain between 2 and 24 µM of silicate (Figure 4.14a), between 3 and 23 µM of nitrate (Figure 4.14c), between 0.4 and 2.2 µM of phosphate (Figure 4.14b) and between 0.05 and 0.6 µM of nitrite (Figure 4.14d). AAIW was observed to contain between 12 and 48 µM of silicate (Figure 4.14a), between 16 and 32 µM of nitrate (Figure 4.14c), between 1.3 and 2.4 µM of phosphate (Figure 4.14b) and between 0.05 and 0.4 µM of nitrite (Figure 4.14d). RSW was observed to contain between 15 and 59 µM of silicate (Figure 4.14a), between 13 and 36 µM of nitrate (Figure 4.14c), between 1.5 and 2.45 µM of phosphate (Figure 4.14b) and between 0.05 and 0.54 µM of nitrite (Figure 4.14d).

The nutrient contents for the water masses identified during the July/August 2017 cruise are described below. TSW was observed to contain between 0 and 9 µM of silicate (Figure 4.15a), between 0 and 11 µM of nitrate (Figure 4.15c), between 0 and 2 µM of phosphate (Figure 4.15b) and between 0.05 and 0.45 µM of nitrite (Figure 4.15d). STSW was observed to contain between 0 and 11 µM of silicate (Figure 4.15a), between 0 and 15 µM of nitrate (Figure 4.15c), between 0.05 and 1.7 µM of phosphate (Figure 4.15b) and 0 and 0.8 µM of nitrite (Figure 4.15d). SICW was observed to contain between 3 and 23 µM of silicate (Figure 4.15a), between 4 and 26 µM of nitrate (Figure 4.15c), between 0.2 and 2.1 µM of phosphate (Figure 4.15b) and between 0 and 0.75 µM of nitrite (Figure 4.15d). AAIW was observed to contain between 26 and 57 µM of silicate (Figure 4.15a), between 26 and 36 µM of nitrate (Figure 4.15c), between 1.2 and 2.5 µM of phosphate (Figure 4.15b) and between

0.02 and 0.06 µM of nitrite (Figure 4.15d). RSW was observed to contain between 19 and 58 µM of silicate (Figure 4.15a), between 20 and 34 µM of nitrate (Figure 4.15c), between 1 and 2.5 µM of phosphate (Figure 4.15b) and between 0 and 0.56 µM of nitrite (Figure 4.15d).

Upon examination of the nutrient concentration curves, depicted in Figure 4.14a-d and Figure 4.15a-d, a few stand out characteristics presented themselves. Nutrient concentrations were observed at lower neutral densities within the TSW water mass during January/February (Figure 4.14a-d), as a result of the higher surface temperatures observed during January/February (Figure 4.5a and Figure 4.8a) which took place during the austral summer. All of the nutrient concentrations, besides for nitrite, displayed a general trend in which the concentrations would increase with increasing neutral density (Figure 4.14a-d and Figure 4.15a-d). For both the January/February and July/August 2017 cruises, the shallow water masses (TSW and STSW) were found to have relatively lower nutrient concentrations than the deep water masses (AAIW, RSW and SICW) which were found to have higher nutrient concentrations (Figure 4.14a-d and Figure 4.15a-d). The nitrite concentration curve did not display the same pattern (Figure 4.14d and Figure 4.15d). The nitrite concentration of TSW as well as that of SICW was relatively higher during the January/February 2017 cruise (Figure 4.14d), whereas STSW had higher concentrations of nitrite during the July/August 2017 cruise (Figure 4.15d).

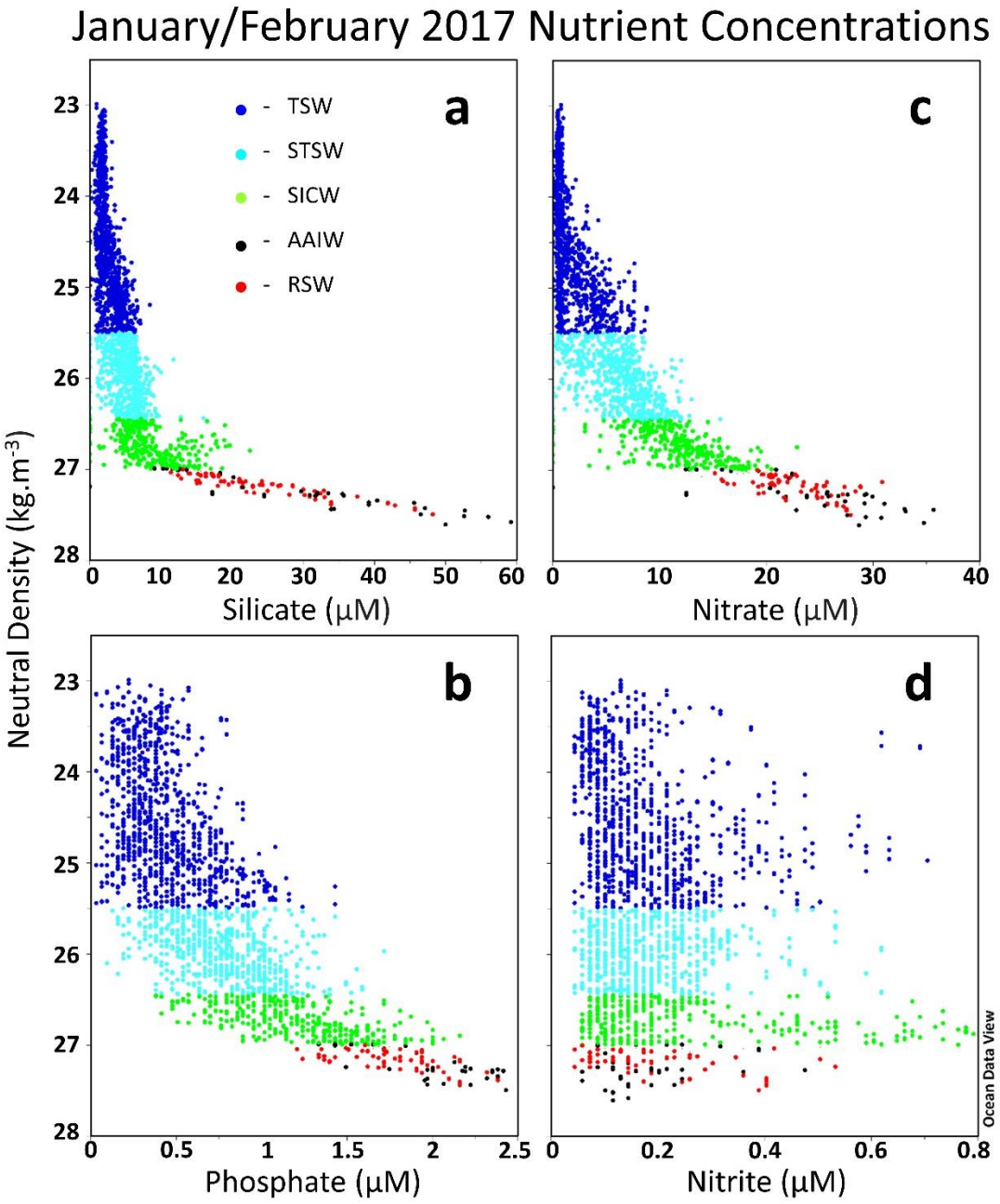

Figure 4.14 a.) Silicate, b.) Nitrate, c.) Phosphate and d.) Nitrite micromolar concentrations during the January/February 2017 cruise for the five identified water masses: tropical surface water (dark blue), subtropical surface water (light blue), south Indian central water (green), Antarctic intermediate water (black) and Red Sea water (red).

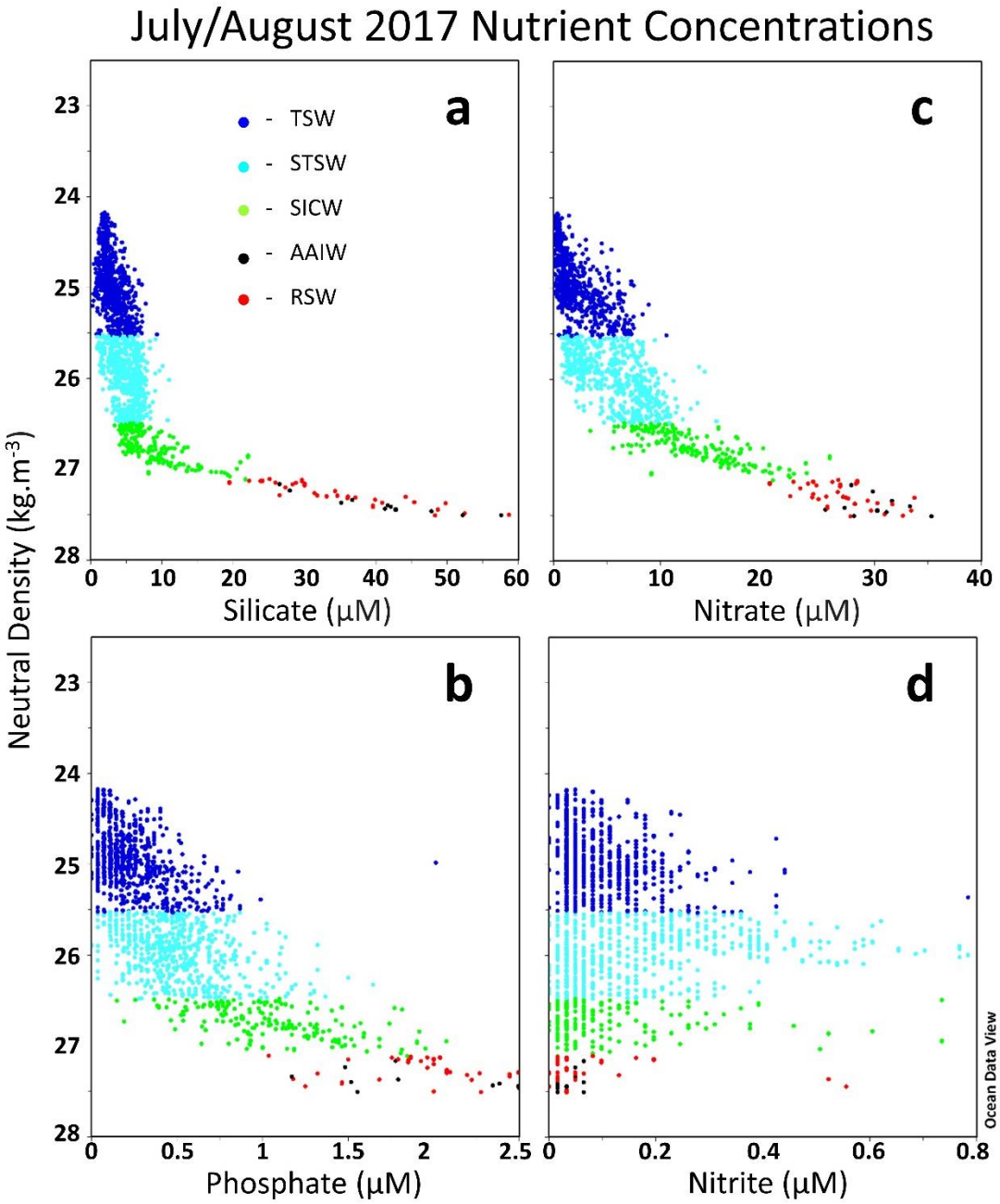

Figure 4.15 a.) Silicate, b.) Nitrate, c.) Phosphate and d.) Nitrite micromolar concentrations during the July/August 2017 cruise for the five identified water masses: tropical surface water (dark blue), subtropical surface water (light blue), south Indian central water (green), Antarctic intermediate water (black) and Red Sea water (red).

4.5 Dissolved Oxygen and Chlorophyll-a Concentrations

The dissolved oxygen (DO) content of the ocean has considerable impacts on marine biogeochemical processes (Stramma et al., 2008). Different oxygen states result in varying ecological consequences such that they can be either ideal for marine organisms to thrive or can cause extreme stress and mortality of the marine organisms (Monteiro and van der Plas, 2006). Since DO is a product of photosynthesizing phytoplankton, high levels of DO are usually observed in areas of high photosynthesis coinciding with high chlorophyll-a (chl-a) concentrations (Parsons et al., 2013). The DO and chl-a concentrations, in conjunction with the previously discussed nutrient concentrations (section 4.4), will be used to briefly investigate and describe the impact that the physical processes could have on the biology of the southeast African shelf and slope. Surface and bottom DO concentrations for the January/February 2017 cruise are depicted in Figure 4.16a-b respectively and surface and bottom DO concentrations for July/August 2017 cruises are depicted in Figure 4.16c-d respectively. Surface as well as chl-a concentrations from the level of maximum chlorophyll (FMAX) for the January/February 2017 cruise are depicted in Figure 4.17a-b respectively and surface and FMAX chl-a concentrations for the July/August 2017 cruises are depicted in Figure 4.17c-d respectively.

4.5.1 January/February 2017 – Austral Summer

The majority of the surface DO concentrations ranged between 4.50 and 5.25 ml/l (Figure 4.16a). The majority of the higher surface DO concentrations were observed inshore throughout the study area, while the lower surface DO concentrations, associated with the position of the inshore edge of the Agulhas Current, were observed offshore, specifically between Cape Recife and Port Shepstone (Figure 4.16a). Patches of relatively high surface DO concentrations (> 5.25 ml/l), were observed between Cape Recife and just east of East London (Figure 4.16a) while relatively low (4.25-5 ml/l) surface DO concentrations were observed at sites A, B and C (Figure 4.16a). The majority of the bottom DO concentrations ranged between 3.50 and 4.50 ml/l (Figure 4.16a). A general pattern for bottom DO concentrations is not easily discernible from Figure 4.16b but what is visible is that the surface DO concentrations are higher than the bottom DO concentrations (Figure 4.16a-b). Bottom DO concentrations between 3.5 and 3.75 ml/l were observed both inshore, east of Cape St Francis, in St Francis Bay as well as west of Cape Padrone, and offshore (Figure 4.16b). A bottom DO maximum of 5.45 ml/l was observed in the shallow waters of Algoa Bay (Figure 4.16b). According to ecological consequences of

different oxygen states given by Monteiro and van der Plas (2006), the DO levels observed on the shelf during January/February were found to be in the range where the biological responses would be insignificant, suggesting that oxygen availability was adequate in supporting the existing shelf biology.

The majority of the observed surface chl-a concentration throughout the study area was low (<0.5 $mg.m^{-3}$; Figure 4.17a). Relatively higher surface concentrations of chl-a, between 2 and 5 $mg.m^{-3}$, were observed between Cape Recife and just east of East London (Figure 4.17a). Low surface chl-a concentrations were also observed at sites A, B and C, as depicted by the 0.5 $mg.m^{-3}$ chl-a contour which is seen encircling the three specific sites (Figure 4.17a). These low chl-a concentrations were observed throughout the water column at the three sites (A, B and C) (Figure 4.17a-b). Throughout the study area, the maximum chl-a concentrations, between 2.5 and 5 $mg.m^{-3}$, were observed to occur subsurface at varying depths (Figure 4.17b and e). As was expected, high surface DO concentrations were associated with high concentrations of chl-a (Figure 4.16a and Figure 4.17a).

4.5.2 July/August 2017 – Austral Winter

The concentration of DO observed throughout the study area during the July/August 2017 cruise ranged from a minimum of 3.25 ml/l, observed offshore in the bottom layer, to a maximum of 5.25 ml/l, observed inshore at the surface (Figure 4.16c). The majority of the surface DO concentrations ranged between 4.50 and 4.75 ml/l (Figure 4.16c). The observed surface DO maximum was 5.25 ml/l and was located inshore from just west of Cape St Francis to Algoa Bay, while the observed surface DO minimum, of 4 ml/l, was situated inshore at site F (Figure 4.16c). The bottom DO concentrations were observed to be higher inshore and lower offshore (Figure 4.16d). The majority of the inshore bottom DO concentrations were observed to be between 4 and 4.5 ml/l while the majority of the offshore stations were observed to have bottom DO concentrations lower than 3.75 ml/l (Figure 4.16d). The DO levels observed on the shelf during July/August were similar to those observed during January/February, which according to the criteria given by Monteiro and van der Plas (2006) on the ecological consequences of different oxygen states, were found to be in the range where the biological responses would be insignificant, which suggests that oxygen availability was adequate in supporting the existing shelf biology.

As can be seen in Figure 4.17c, the majority of the observed surface chl-a concentrations were found to be lower than 0.5 $mg.m^{-3}$. Much like the majority of the study area, sites E and F displayed low chl-a concentrations of less than 0.5 $mg.m^{-3}$ throughout their respective water columns (Figure 4.17c-d). Relatively high surface chl-a concentrations, between 1.5 and 2.5 $mg.m^{-3}$, were observed off Port St Johns (Figure 4.17c). The overall maximum chl-a concentrations, between 1.5 and 3 $mg.m^{-3}$, were observed subsurface (Figure 4.17d and f).

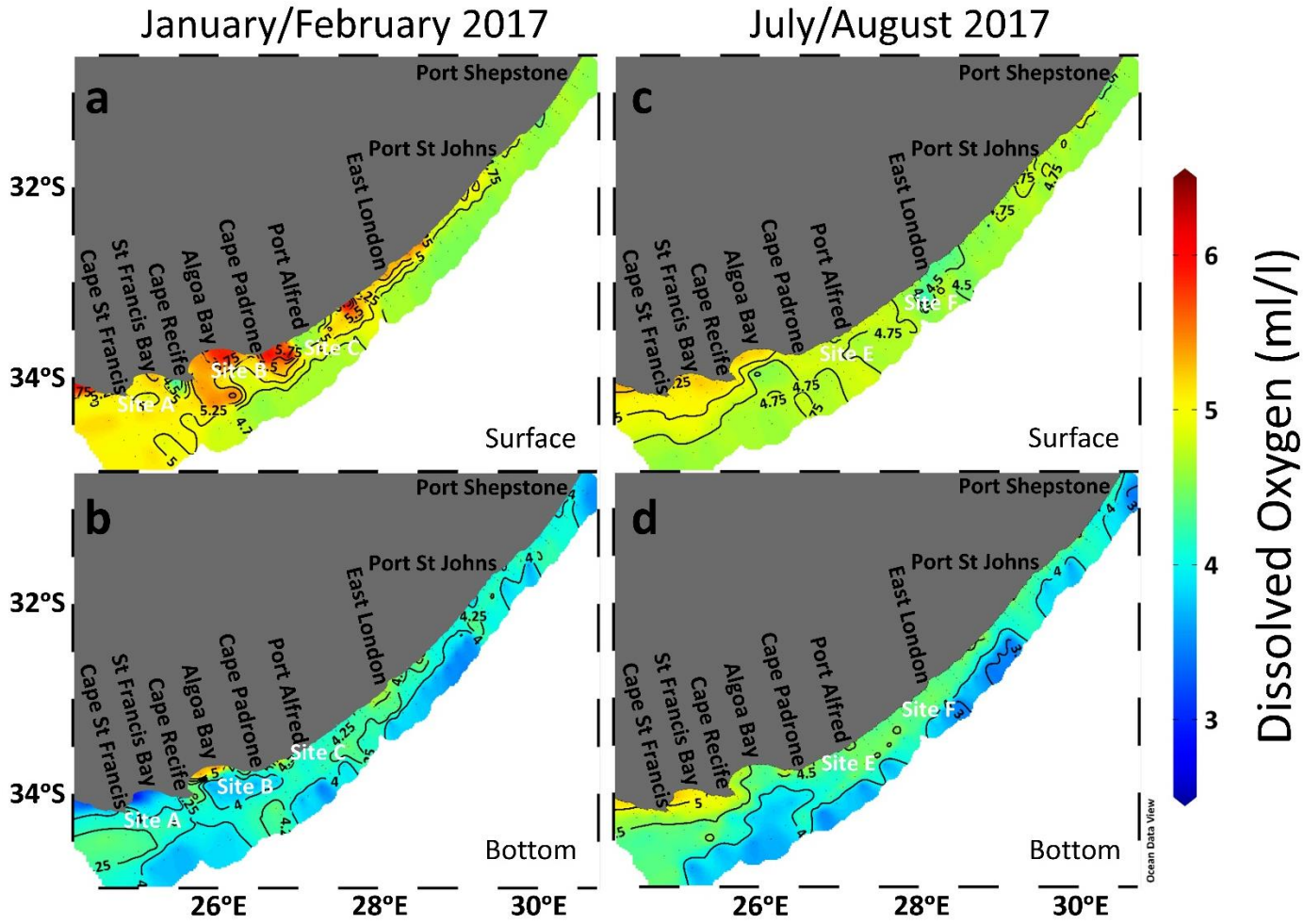

Figure 4.16 *In situ* surface and bottom dissolved oxygen concentration maps for January/February (a-b) and July/August (c-d) 2017, which depict high oxygen at the surface and lower oxygen at depth.

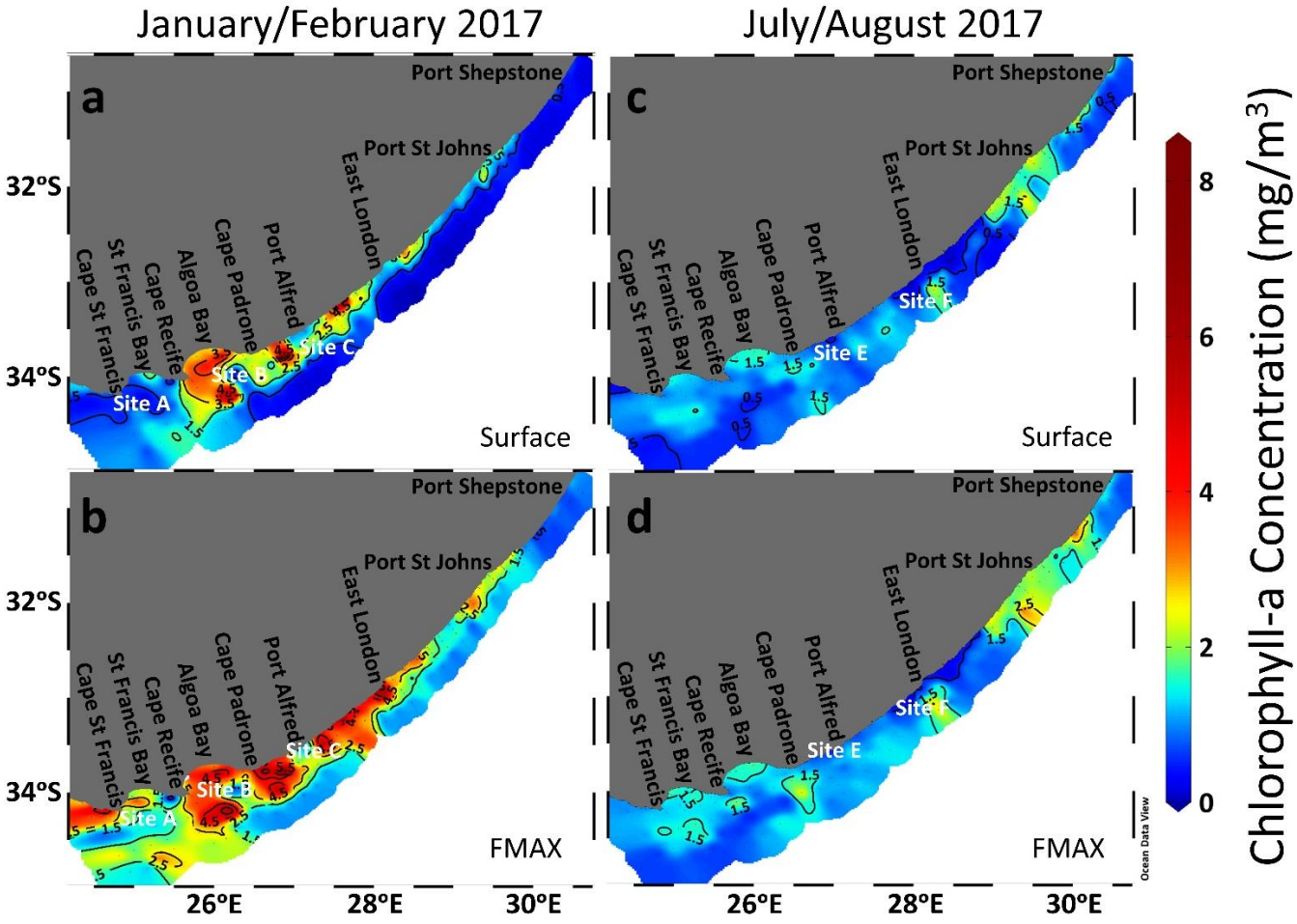

Figure 4.17 *In situ* surface and the level of maximum chlorophyll (FMAX) chlorophyll-a (chl-a) concentration maps for January/February (a-b) and July/August (c-d) 2017, depicting higher chl-a in the austral summer than in the austral winter. Sites (A, B, C, E and F) of low chl-a concentration are highlighted.

4.6 Case Study 1: Influence of Mesoscale Features on Shelf Waters

The presence of a cyclonic eddy during the course of both the January/February and July/August 2017 cruises was identified in Figure 4.1a-b and Figure 4.3a-b respectively. As previously discussed in section 2, cyclonic cold-core eddies have a clockwise circulation in the southern hemisphere which result in the uplift of cold water from depth, potentially increasing the nutrient input into the upper ocean (Doblin et al., 2016, Bakun, 2017). This case study therefore seeks to identify the effect that these mesoscale features had on the shelf waters during the period of the January/February and July/August 2017 cruises.

4.6.1 January/February 2017 – Austral Summer

The cyclonic cold-core eddy identified in Figure 4.1, has been further highlighted in Figure 4.18a. The presence of the cyclonic eddy coincided with the presence of a inshore current reversal, confirmed by the S-ADCP velocity vectors (Figure 4.19) as well as by the cyclonic circulation depicted by the geostrophic velocity anomaly vectors (Figure 4.18a). The presence of low bottom temperatures between 6 and 10 ^{o}C, were observed offshore, with these waters extending inshore into both St Francis Bay and Algoa Bay, depicted by the 10 ^{o}C isotherm in Figure 4.18b. These low bottom temperatures have been found to coincide with the location of the cyclonic eddy identified in Figure 4.18. An analysis of the bottom neutral density (Figure A.4a) indicated that the low temperature water observed on the shelf was consistent with South Indian Central Water (SICW; 26.4-27.0 kg/m^3). The vertical temperature sections represented in Figure A.5a, further illustrate the influence that the January/February cyclonic eddy had on the shelf water in comparison to when it was not there in July/August. The uplift and advection of the SICW onto the shelf is represented by the close proximity of the 10 ^{o}C isotherm to the surface (at 100 db), as well as to the coast (between approximately 20-30 km) seen in Figure A.5a. The presence of these central waters, which extend inshore as well as eastward, are most likely as a result of Ekman pumping associated with the presence of the cyclonic eddy. In contrast, in the absence of an eddy at the same transect during July/August, the 10 °C isotherm is located at 450 db, roughly 65 km from the coast (Figure A.5b).

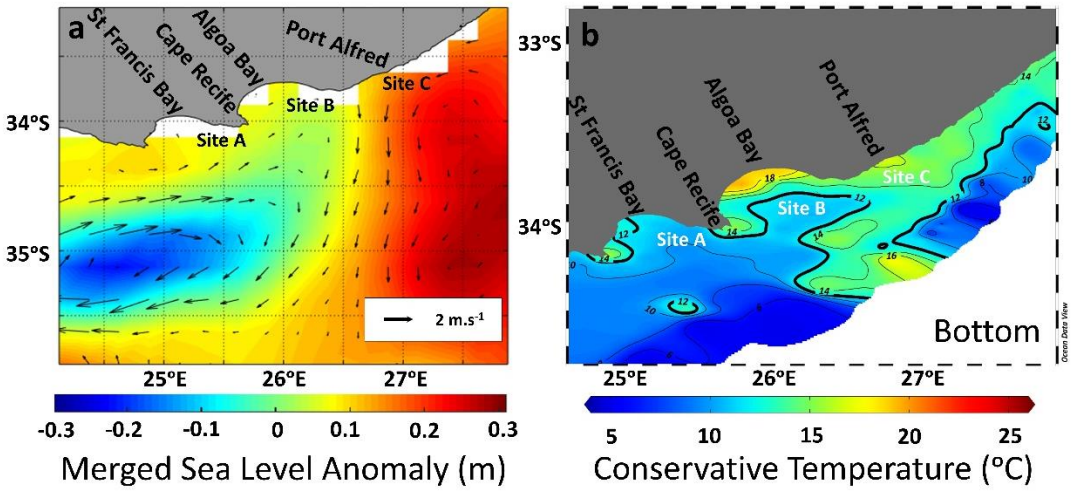

Figure 4.18 Zoomed maps of areas influenced by the January/February cyclonic eddy. a.) AVISO sea level anomaly data (19/01/2017) overlaid with geostrophic velocity anomaly vectors, depicting the January/February cyclonic eddy (35°S; 24.8°E). b.) *In situ* bottom temperature map illustrating the influence of the January/February cyclonic eddy.

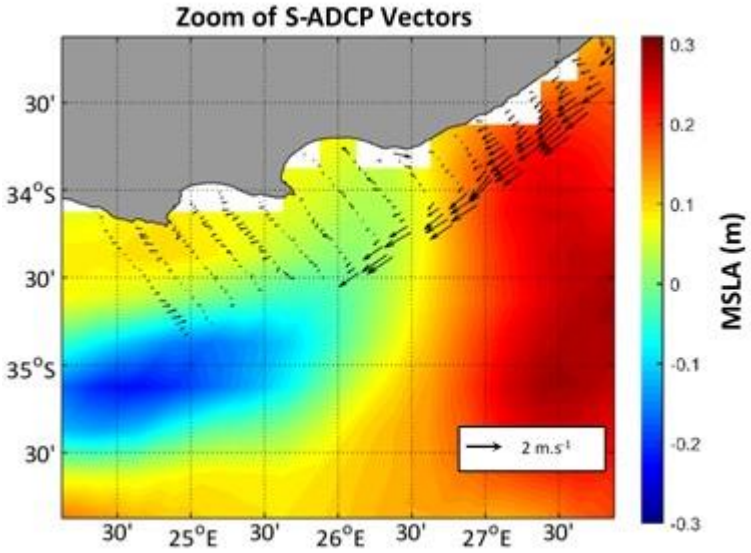

Figure 4.19 Zoomed in map of SLA data acquired from AVISO on the 19/01/2017 overlaid with shipboard acoustic Doppler current profiler (S-ADCP) velocity vectors obtained from the January/February 2017 cruise, highlighting the cyclonic motion of the January/February cyclonic eddy captured by the S-ADCP.

4.6.2 July/August 2017 – Austral Winter

The northern section of the July/August 2017 cyclonic eddy, identified in Figure 4.3b, has been further highlighted in Figure 4.20a. No *in situ* current reversals were observed during the July/August 2017 cruise on account of the unavailability of the S-ADCP data, however current reversals were observed in the ADT data

represented in Figure 4.3a and Figure 4.20a. With regards to the influence of the eddy on the bottom temperature, relatively low bottom temperatures were observed inshore, which is depicted by the 15 ^{o}C isotherm between Port Alfred and East London (Figure 4.20b). These bottom temperatures were not as low as those observed in January/February (Figure 4.18b). The analysis of the bottom neutral density (Figure A.4b) indicated that the low temperature water observed on the shelf was consistent with South Indian Central Water (SICW; 26.4-27.0 kg/m^3). Similar to what was observed in January/February, the presence of the low temperature SICW on the shelf in July/August is most likely as a result of Ekman pumping associated with the presence of the cyclonic eddy. As a result of the July/August eddy being located further offshore (> 3000 m isobath; Figure 4.20a and *Figure 4.3*b), it is suggested that the uplift observed during July/August was not as intense as that which was observed in January/February, where the core of the January/February cyclonic eddy (2000 m isobath) was closer to the shelf (Figure 4.18a and Figure 4.1b).

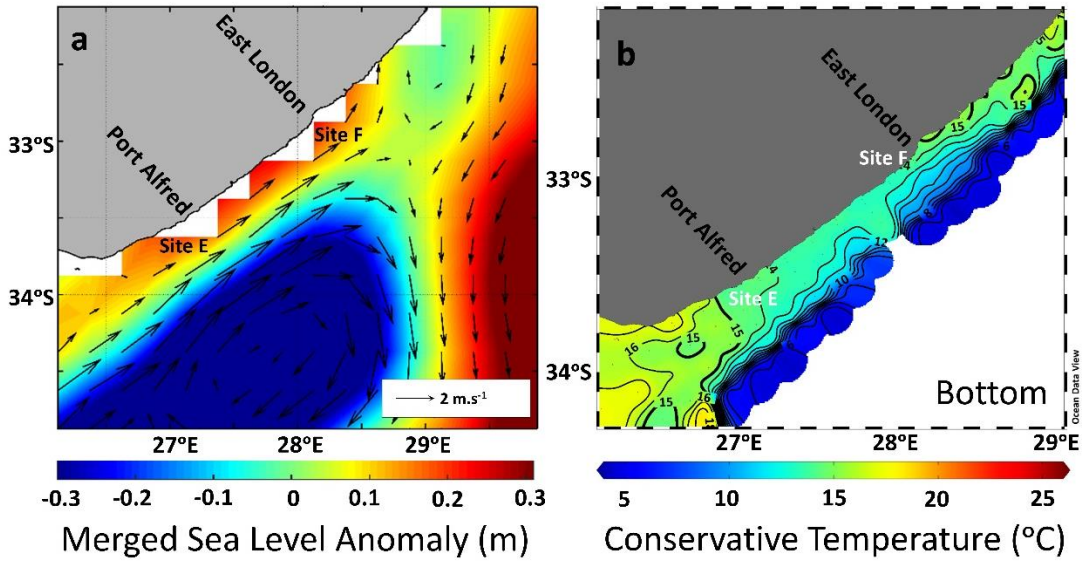

Figure 4.20 Zoomed maps of areas influenced by the July/August cyclonic eddy. a.) AVISO sea level anomaly data (29/07/2017) overlaid with geostrophic velocity anomaly vectors, depicting the northern part of the July/August cyclonic eddy. b.) *In situ* bottom temperature map illustrating the cooling resulting from Ekman pumping associated with the July/August cyclonic eddy.

4.7 Case Study 2: Influence of Mesoscale Features on Intermediate Water Masses

The intermediate water masses observed during both the January/February and July/August 2017 cruises comprised of AAIW and RSW and were located at the offshore stations (1000 m isobath) which can be seen in the geographical maps in both Figure 4.21 and Figure 4.22 . A comparison of the intermediate waters resulted in the identification of two contrasting scenarios. During the January/February 2017 cruise there was a clear separation between the AAIW and the RSW (Figure 4.8a and Figure 4.21a). During the July/August 2017 cruise, there seemed to be greater mixing of the AAIW and RSW (Figure 4.8b). These two contrasting scenarios prompted a deeper investigation into the source of this difference.

The 1000 m isobath stations at which RSW was observed, during the January/February 2017 cruise, were located between Cape Padrone and Port Shepstone, as indicated by the red dots in Figure 4.21c. The stations at which the AAIW was observed, were located roughly between Cape St Francis and Cape Padrone, as indicated by the blue dots depicted in Figure 4.21c. The geographic position of the AAIW stations (Figure 4.21c) were found to coincide with the position of the January/February cyclonic eddy (Figure 4.1b).

During the July/August cruise, the location of the AAIW versus RSW differed from that which was observed during the January/February cruise. During the July/August cruise, RSW was observed at the 1000 m isobath stations located between Cape St Francis and Cape Padrone, as well as between East London and Port Shepstone, as indicated by the red dots in Figure 4.22c. The AAIW was located at ten consecutive offshore stations between Cape Padrone and East London as indicated by the blue dots in Figure 4.22c. The geographic positions of the AAIW stations (Figure 4.22c) were found to coincide with the position of the July/August cyclonic eddy (Figure 4.3b) which similarly occurred in January/February (Figure 4.1b and Figure 4.21c).

AAIW has a higher dissolved oxygen (DO) concentration than RSW and so the higher DO concentration present in the 2 to 10 ^{o}C temperature range, depicted in Figure 4.21b and Figure 4.22b, supports the suggestion that higher proportions of AAIW are located at the eddy-impacted stations during both the January/February and July/August 2017 cruises. The presence of a cyclonic eddy in January/February and July/August 2017 has been identified as the source of AAIW at the 1000 m

isobath stations along the inshore edge of the Agulhas Current, while RSW was observed at the 1000 m isobath stations where there was no cyclonic eddy present.

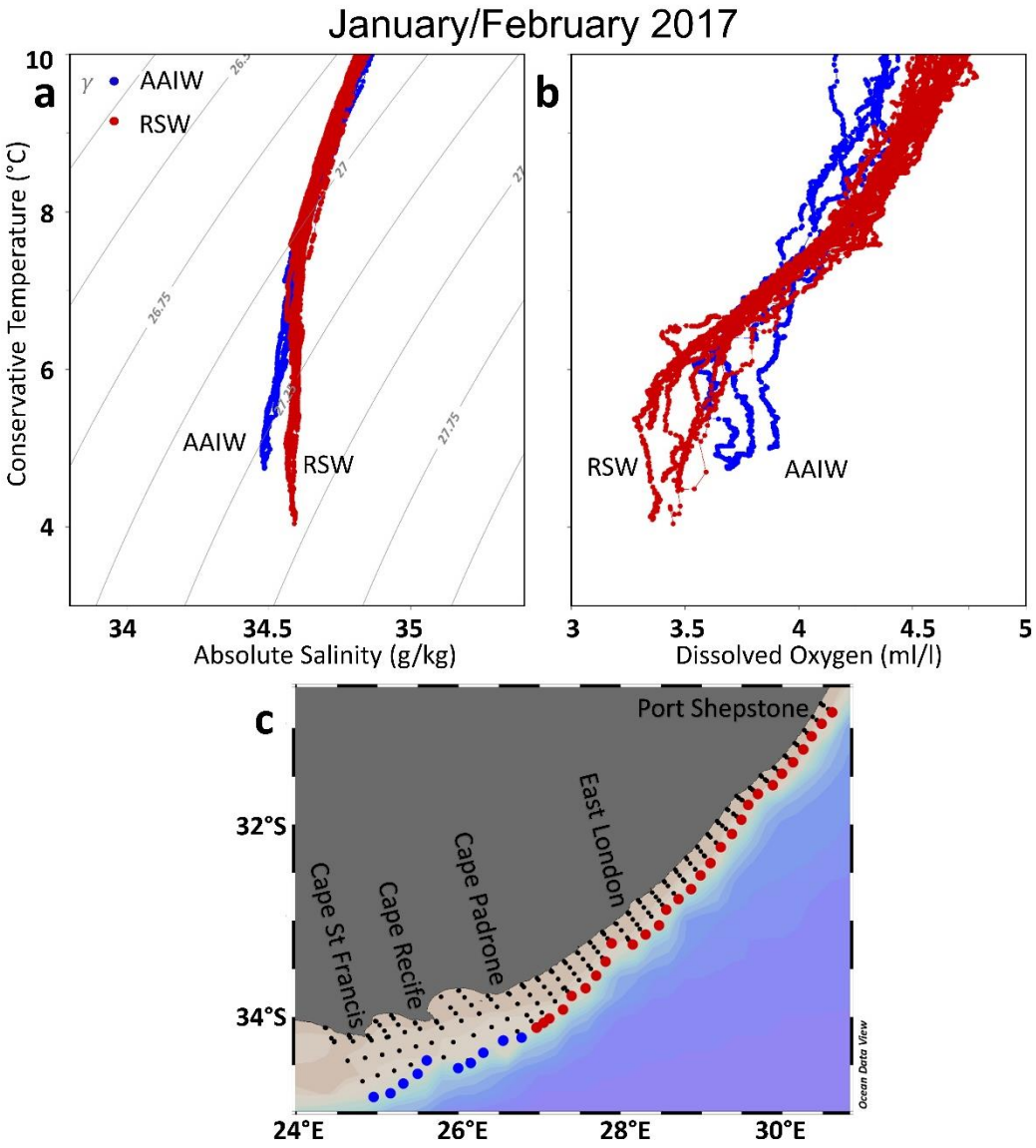

Figure 4.21 a.) Temperature-Salinity (TS) and b.) Temperature-Oxygen (TO) plots for Red Sea Water (RSW; red dots) and Antarctic Intermediate Water (AAIW; blue dots) observed during the January/February 2017 cruise. c.) Geographical map indicating the location of the stations at which AAIW and RSW were observed.

The contrasting scenarios which saw less mixing of AAIW and RSW during January/February, and more mixing of AAIW and RSW during July/August, has been attributed to the positions of the cores of the January/February and July/August cyclonic eddies relative to the slope. In January/February, the AAIW stations (Figure 4.21c) were located within close proximity to the core the cyclonic eddy (Figure 4.1b) which was positioned against the continental slope (along the 2000 m isobath)

resulting in the clearer separation and limited mixing of the water masses. In July/August 2017, the AAIW stations (Figure 4.22c) were not in close proximity to the core of the eddy because it was positioned further offshore (> 3000 m isobath; Figure 4.3b) which allowed for greater mixing between the AAIW and RSW to take place.

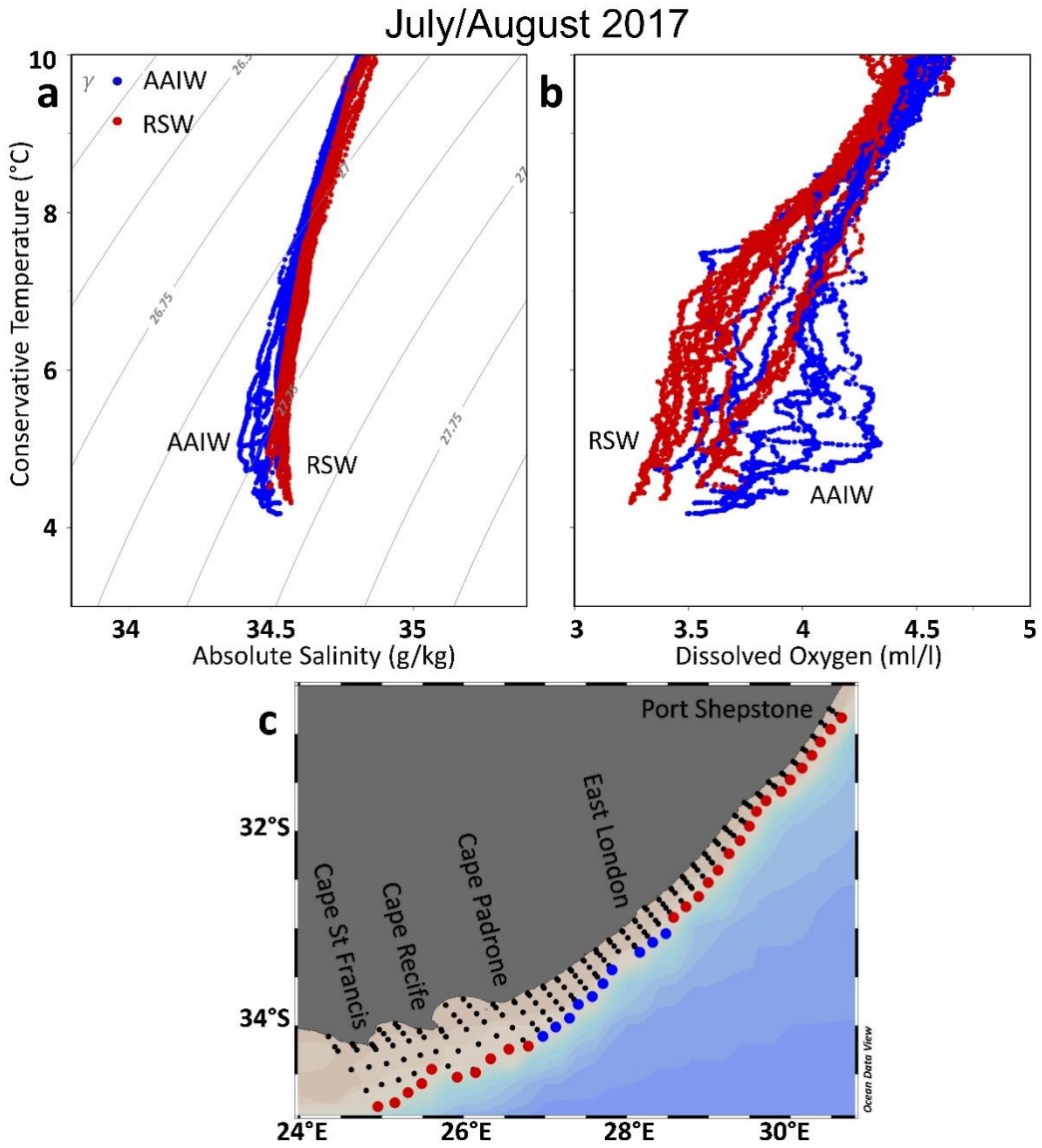

Figure 4.22 a.) Temperature-Salinity (TS) and b.) Temperature-Oxygen (TO) plots for Red Sea Water (RSW; red dots) and Antarctic Intermediate Water (AAIW; blue dots) observed during the July/August 2017 cruise. c.) Geographical map indicating the location of the stations at which AAIW and RSW were observed.

4.8 Case Study 3: Influence of Wind on Hydrographic Patterns

Five sites of low surface temperature were identified in section 4.2. Three sites (A, B and C) were observed during the January/February 2017 cruise (Figure 4.23a) and the remaining two (E and F) were observed during the July/August 2017 cruise (Figure 4.23b). Sites A, C, E and F were located inshore, in close proximity of the coast, while Site B was located slightly further from the coast in the mid-shelf region. The locations, surface temperatures and dates of sampling of the above mentioned sites have been highlighted in Table 4.1. With wind-driven coastal upwelling being a common occurrence along the southeast coast of South Africa (Goschen et al., 2012), this case study will seek to identify whether the process responsible for these low surface temperature sites was wind-driven coastal upwelling.

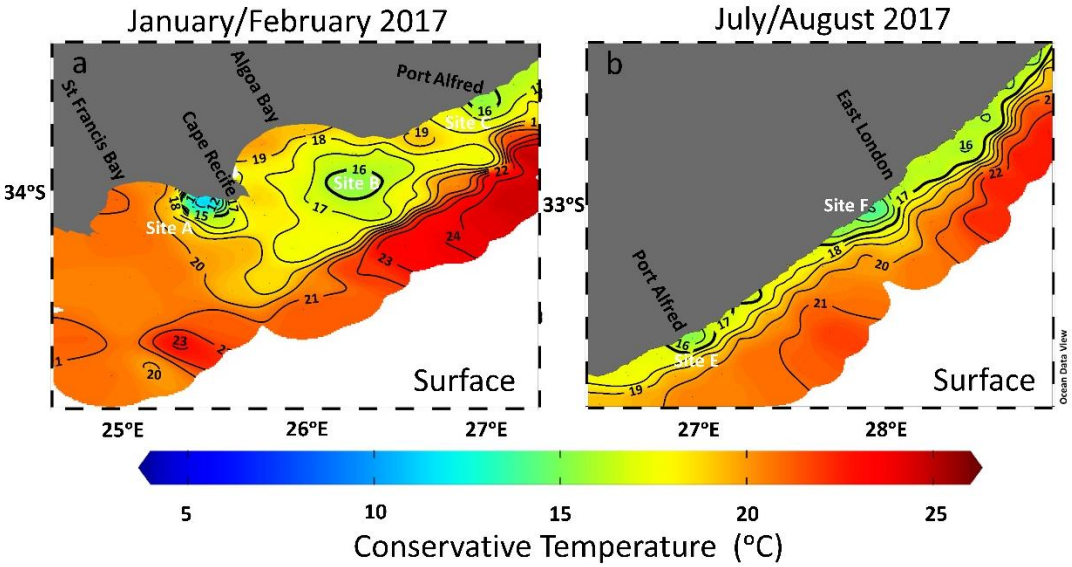

Figure 4.23 Zoomed surface temperature maps for the a.) January/February 2017 and b.) July/August 2017 cruises, highlighting sites of low surface temperature labelled sites A, B, C, E and F.

Table 4.1 Sites of low surface temperature, their location, as well as the date of sampling from the January/February and July/August 2017 cruises.

Site	Location	Surface Temperature	Date of Sampling
A	Cape Recife	10.7 °C	18-01-2017
B	West of Cape Padrone	15.3 °C	20-01-2017
C	Port Alfred	15.3 °C	22-01-2017
E	Port Alfred	14.5 °C	29-07-2017
F	West of East London	13.7 °C	01-08-2017

4.8.1 January/February 2017 – Austral Summer

As depicted by the wind vectors in Figure 4.24a-f, an easterly component wind was present one day prior to sampling, as well as on the day of sampling (refer to Table 4.1), at both sites A and C. Shoreward sloping isotherms, depicted in Figure 4.25a and c, indicate that the winds were successful in breaking down the stratification of the water column at both sites A and C and thus depict upwelling. As can be seen in Figure 4.25a, the 11 °C isotherm, which surfaces at site A, extends far offshore, connecting the shallow inshore waters to the deep offshore waters, influenced by the cyclonic eddy discussed in section 4.6.1. Contrastingly, the 15 °C isotherm, which surfaces at site C, was confined inshore depicting no connection between the deep offshore waters (Figure 4.25c). The upwelling at site A saw the surfacing of SICW as presented in section 4.3, while the upwelled water at site C was STSW.

The Ekman Layer Depths (ELDs) at sites A and C were calculated to be 101.57 m and 102.22 m, respectively (Table 4.2), which suggest that frictional influence of the wind should have affected the entire water column at the respective sites, resulting in an isothermal structure from the surface to the calculated ELDs. Since the bottom depth at these sites is much less that the calculated ELD, the MLDs were also analysed. The isothermal structure suggested for sites A and C has been confirmed by the calculated Mixed Layer Depths (MLDs) which extend to 23 m and 24 m, respectively which are the bottom of the water column at these sites. Since the wind acts over an area larger than just that of the specific sites (Figure 4.24a-f), this isothermal structure was expected to be observed across the shelf (see temperature sections in Figure 4.25a and c), from the surface to approximately the same depth as the respective calculated ELDs. While an isothermal structure was observed throughout the water column at sites A and C, respectively, it was not observed

across the shelf (Figure 4.25a and c). The absence of the expected shelf-wide isothermal structure is suggested to be as a result of the dominating influence of the impinging features such as, the inshore edge of the Agulhas Current (in Figure 4.25c) and the January/February cyclonic eddy (in Figure 4.25a), over that of the influence of the wind. The close proximity of the inshore edge of the Agulhas Current observed in Figure 4.25c, resulted in the input of warm Agulhas Current water at the surface, which enhanced the stratification across the shelf. The influence of the January/February cyclonic eddy observed in Figure 4.25a, enhanced stratification across the shelf via the input of cold (< 10 ^{o}C) water along the bottom of the shelf through the upwelling process associated with cyclonic eddy dynamics, as well as via the input of warm Agulhas Current water at the surface due to the eddy's clockwise circulation at the surface.

Table 4.2 Sites of low temperature exposed to upwelling favourable wind, the date of sampling, their latitude, the bottom depth, the resultant wind speed on the date on sampling, the Ekman Layer Depth calculated using Equation 3.5 and the Mixed Layer Depth

Site	Date of Sampling	Latitude (θ)	Bottom Depth	Wind Speed (U_{10})	Ekman Layer Depth	Mixed Layer Depth
A	18-01-2017	34.05 °S	23 m	10 m.s^{-1}	101.57 m	23 m
B	20-01-2017	33.96 °S	98 m	12 m.s^{-1}	122.02 m	23 m
C	22-01-2017	33.56 °S	24 m	10 m.s^{-1}	102.22 m	24 m
E	29-07-2017	33.59 °S	28 m	8 m.s^{-1}	81.74 m	28 m
F	01-08-2017	33.03 °S	26 m	9 m.s^{-1}	92.64 m	26 m

Site B was exposed to varying winds, initially dominated by winds with easterly components and thereafter dominated by winds with westerly components (Figure 4.24a-d). These varying winds induced vertical mixing and the uplift of cooler waters at site B, which is depicted by the doming of the isotherms seen in Figure 4.25b. In comparison to site A where SICW was upwelled, STSW was upwelled at site B, similar to that at site C. Although the ELD at site B was calculated to be 122.02 m (Table 4.2), the expected isothermal structure throughout the water column was not observed across the shelf in the temperature section nor in the water column at site B (Figure 4.25b). The MLD, contrasting the ELD and indicates that an isothermal structure was observed in the upper 23 m of the water column (Table 4.2). It is suggested that the expected isothermal structure throughout the water column was

not observed as a result of the influence of the January/February cyclonic eddy, which resulted in the continuous advection of cold water in the lower layers to site B – preventing the development of isothermal conditions.

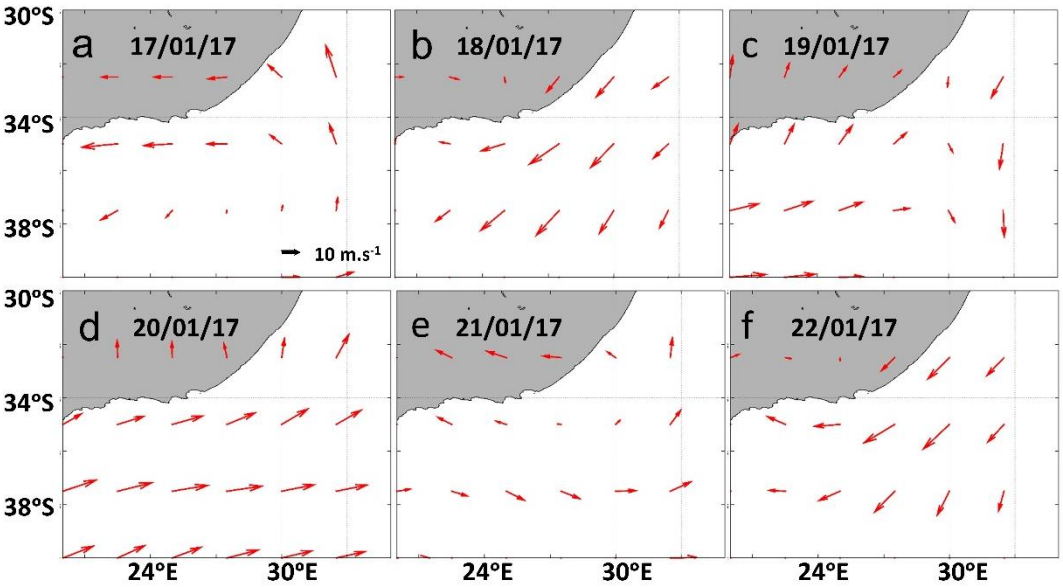

Figure 4.24 Selected daily National Centres for Atmospheric Prediction (NCEP) surface wind maps for the January/February 2017 cruise, depicting upwelling favourable winds prior to the sampled wind-driven upwelling events.

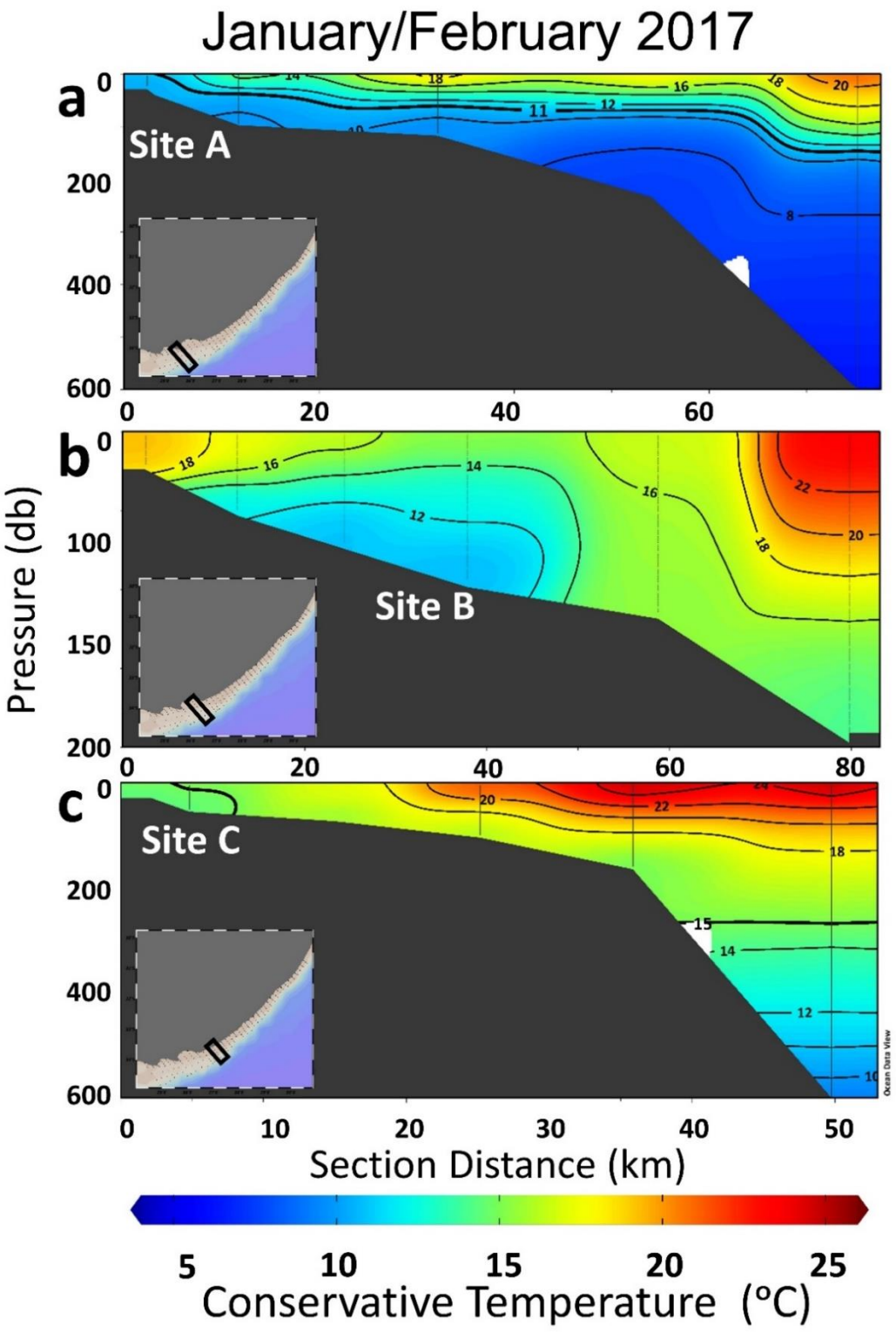

Figure 4.25 Vertical temperature sections of the three upwelling sites during the January/February 2017 cruise. a.) Site A (sampled on 18-01-2017), depicting the connection between the inshore and offshore waters due to the influence of the January/February cyclonic eddy. b.) Site B (sampled on 20-01-2017), depicting doming of isotherms as a result of wind induced vertical mixing and c.) Site C (sampled on 22-01-2017), depicting no connection between the inshore and offshore waters.

4.8.2 July/August 2017 – Austral Winter

Northerly winds with slight easterly components were present one day prior to sampling at site E (Figure 4.26a), while on the day of sampling at site E (refer to Table 4.1), winds with strong westerly components were present (Figure 4.26b). Figure 4.27a depicts shoreward sloping isotherms whose gradient flattens on approach of site E. This flattening of the inshore isotherms' gradients (Figure 4.27a), depicts the possible end of an upwelling event as a result of the varying wind directions.

As can be seen in Figure 4.26d, northerly winds with relatively large easterly components, were present one day prior to sampling at site F (refer to Table 4.1). Figure 4.27b depicts shoreward sloping isotherms, whose gradients steepen on approach of site F. This relatively steep inshore gradient suggests that the winds were successful in breaking down the stratification of the water column at site F and thus are indicative upwelling (Figure 4.27b). A connection between the shallow inshore waters and the deep offshore waters is depicted by the 14 ^{o}C isotherm in Figure 4.27b. At the shelf-edge, the increase in gradient of the 10 ^{o}C isotherm, at the section distance of approximately 26 km (Figure 4.27b), coincides with the location of the July/August cyclonic eddy discussed in 4.6.2. Similar to what was observed at site A during the January/February 2017 cruise, the upwelling at site F saw the surfacing of SICW while that at site E saw the surfacing of STSW (similar to sites B and C during the January/February cruise).

The Ekman Layer Depth (ELD) at sites E and F were calculated to be 81.74 m and 92.64 m, respectively (Table 4.2), which suggests that the frictional influence of the wind is expected to be felt throughout the water column, resulting in an isothermal structure from the surface to the calculated ELDs. Given that the bottom depths at these sites are much less that the calculated ELDs, the MLDs were also analysed. The abovementioned isothermal structure, at sites E and F, has been confirmed by the calculated Mixed Layer Depths (MLDs) which extend to 28 m and 26 m, respectively, the bottom of the water column at these sites. While the expected isothermal structure was observed in the water columns at sites E (Figure 4.27a) and F (Figure 4.27b), it was not observed across the shelf. The influence of the July/August cyclonic eddy observed in Figure 4.27a-b was similar to that of the January/February cyclonic eddy in Figure 4.24a, such that it resulted in the enhanced shelf-wide stratification via the same processes discussed in the previous section.

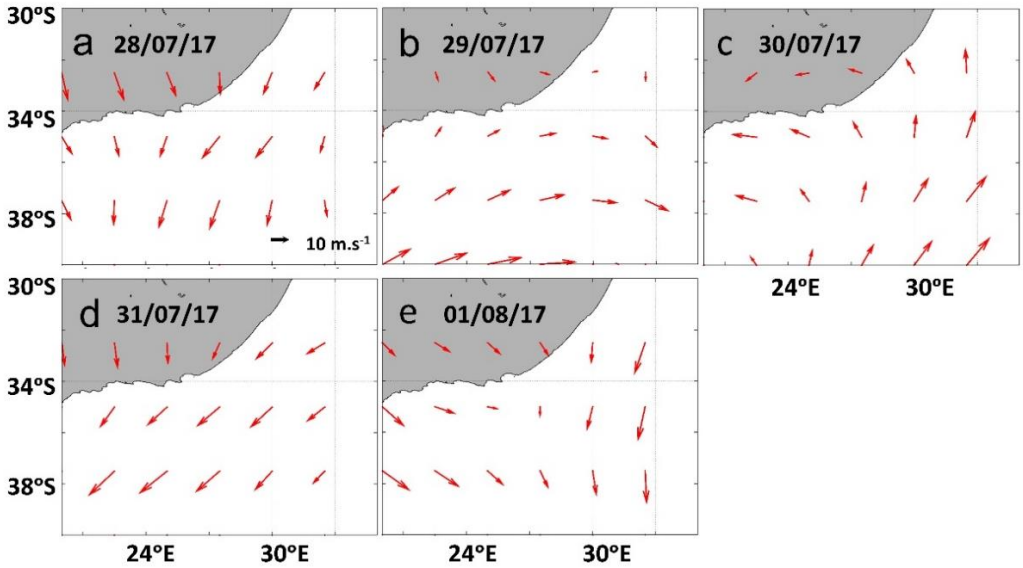

Figure 4.26 Selected daily National Centres for Atmospheric Prediction (NCEP) surface wind maps for the July/August 2017 cruise, depicting upwelling favourable winds prior to the sampled wind-driven upwelling events.

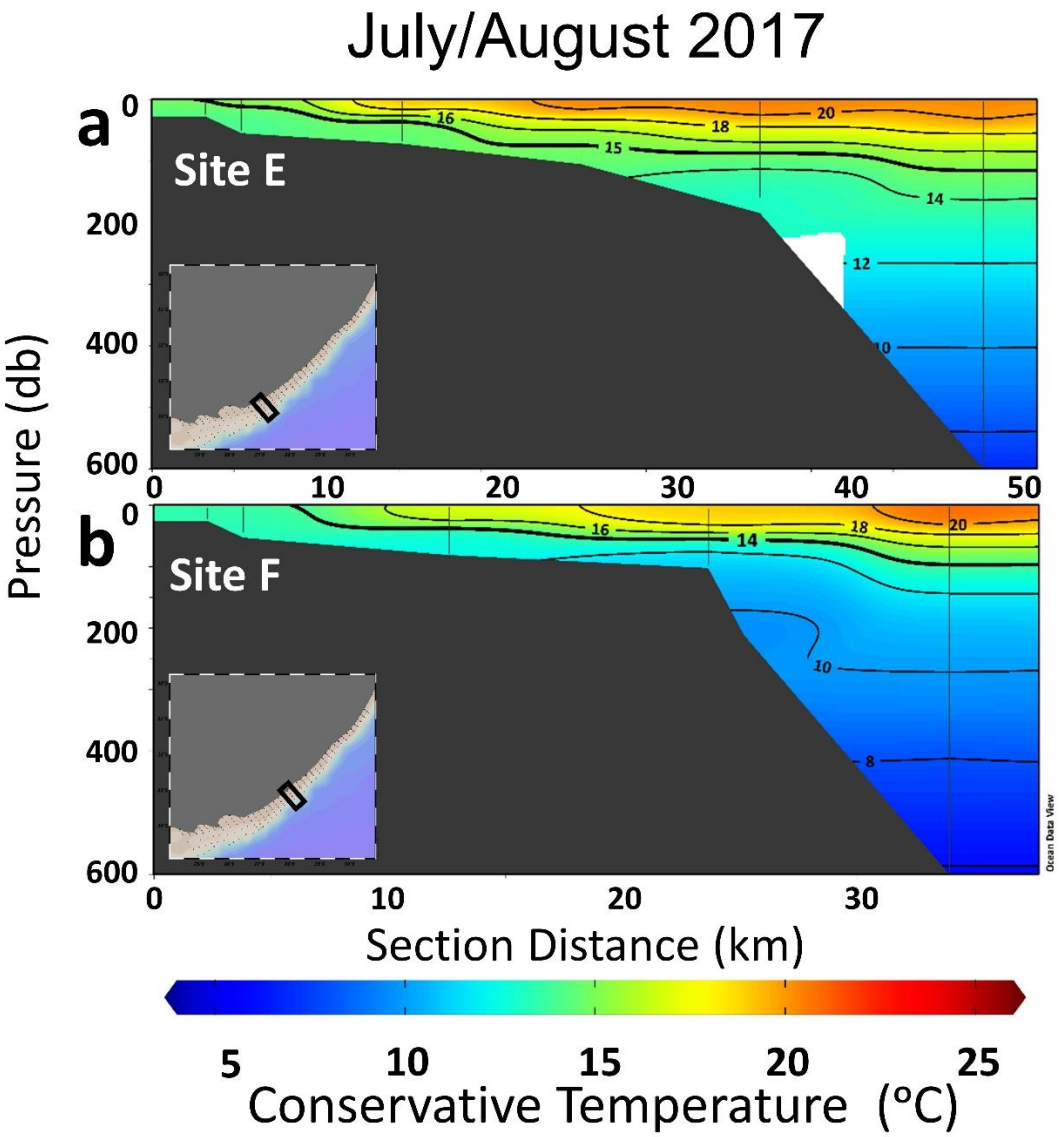

Figure 4.27 Vertical temperature sections for sites a.) E (sampled on 29-07-2017) and b.) F (sampled on 01-08-2017) during the July/August 2017 cruise, depicting the connection between the inshore and offshore waters as a result of the influence of the July/August cyclonic eddy.

4.9 Case Study 4: Influence of River Outflow on the Hydrography of Near-shore Stations

Two sites of low surface salinity, sites A and D, were identified in section 4.2 (see Figure 4.6a). As described in case study 3, in section 4.8, site A was exposed to easterly component alongshore winds prior to the day of sampling which induced Ekman transport in the surface layer which led to upwelling at site A. This upwelling led to the surfacing of less saline water from depth which is illustrated in the vertical section in Figure 4.28a. The low surface salinity observed at site A (Figure 4.28a), is clearly linked to upwelling but that which is observed at site D (Figure 4.28b), is not. As illustrated in the vertical section in Figure 4.28b, the anomalously low surface salinity of 33.7 g/kg was observed to be confined to the surface layer at Site D. Upon further investigation it was found that site D was located at the Mzimvubu River mouth.

This case study therefore seeks to investigate and describe the influence of river outflow on the hydrography of the near-shore stations. The near-shore sites situated at the mouths of the Mzimvubu River, the Sundays River, the Great Fish River and the Great Kei River were investigated during both the January/February and July/August 2017 cruises. In order to determine the river influence on the hydrography of the near-shore sites, salinity maps, rainfall maps as well as river flow rate graphs were considered.

The general rainfall pattern indicated higher rainfall during the course of the January/February 2017 cruise which took place during the austral summer season (Figure 4.29a-c). Relatively higher river flow rates were also observed during the January/February cruise (Figure 4.30a-d). The occurrence of low river flow rates (Figure 4.30a-d) coincided with low rainfall (Figure 4.29d-f) and the occurrence of relatively high river flow rates (Figure 4.30a-d) coincided with moderate to high rainfall (Figure 4.29a-c).

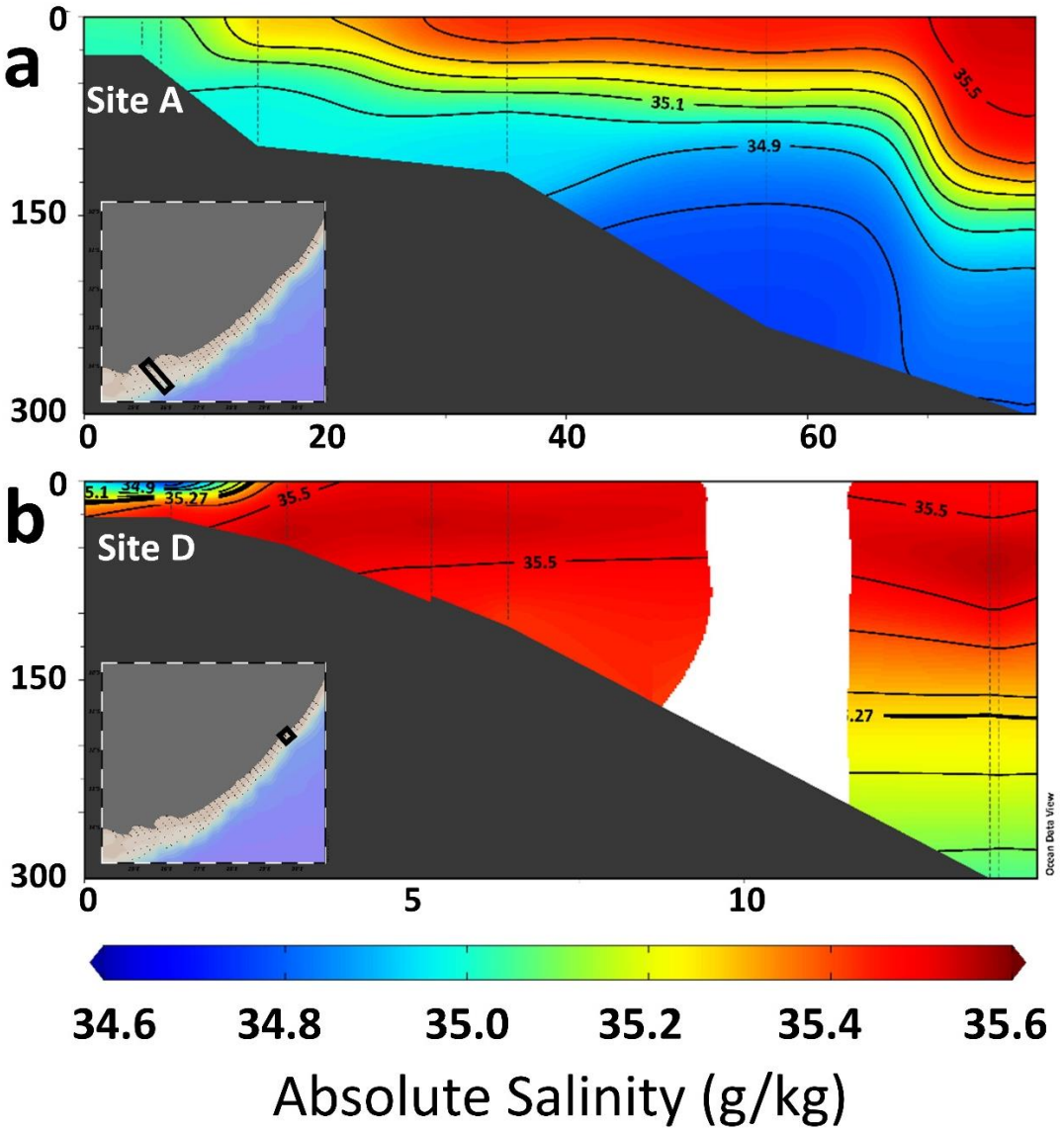

Figure 4.28 Vertical cross-shelf salinity sections of the sites of low surface salinity observed during the January/February 2017 cruise. a.) Depicts the transect associated with site A, highlighting the connection between the low salinity waters observed inshore, with those observed offshore as a result of the influence of the January/February cyclonic eddy. b.) Depicts the transect associated with site D (Mzimvubu River), highlighting the influence and extent of the Mzimvubu River outflow on the upper waters by the 35.27 g/kg isohaline, with the white patch indicating an area of no data as a result of the chosen interpolation.

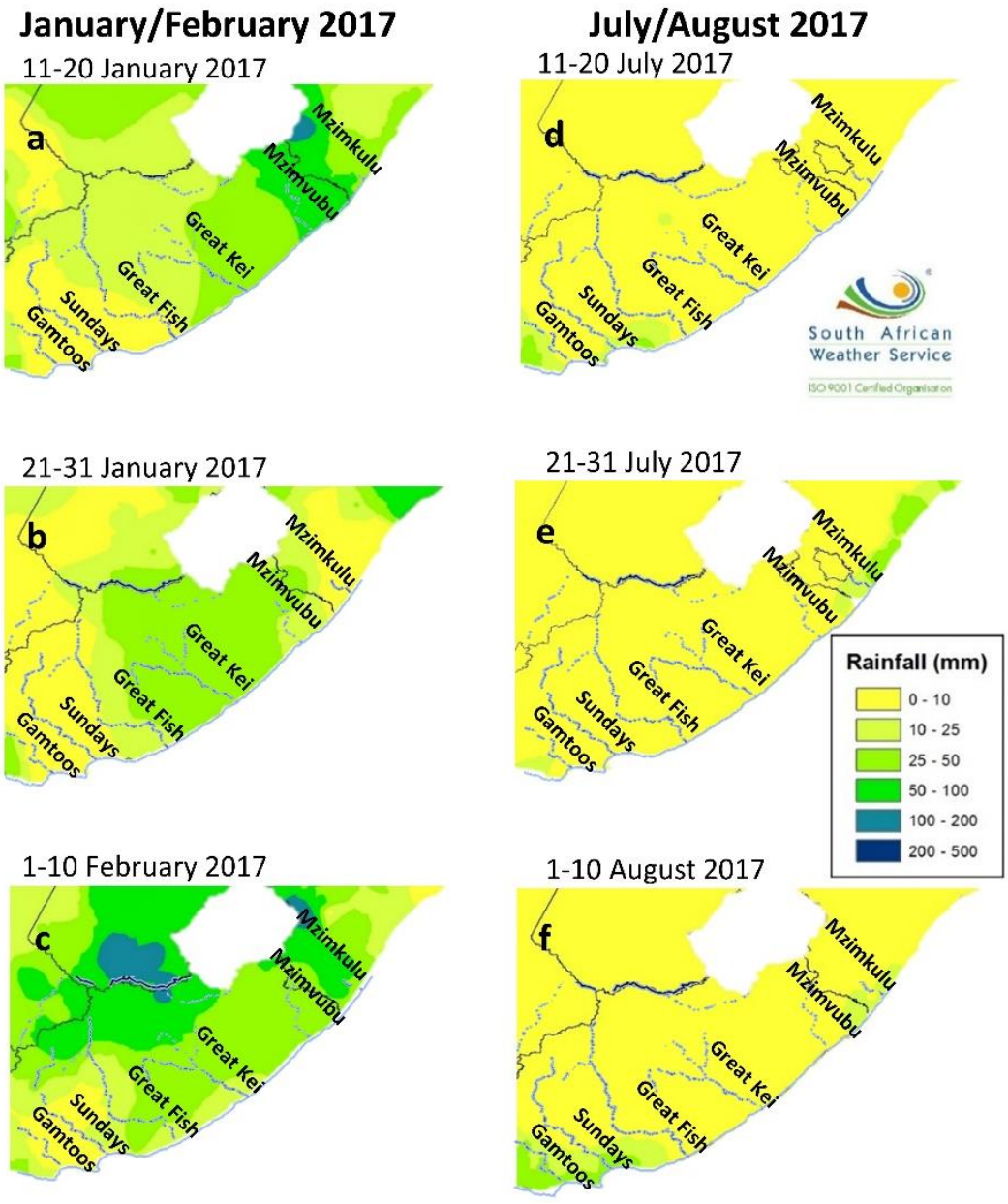

Figure 4.29 Rainfall maps, adapted from the South African Weather Service (SAWS), depicting total ten-day rainfall over the south eastern region of South Africa throughout the course of the January/February (a-c) and July/August (d-f) 2017 cruises. Relatively higher rainfall was observed during January/February than during July/August, particularly over the Mzimvubu River catchment area.

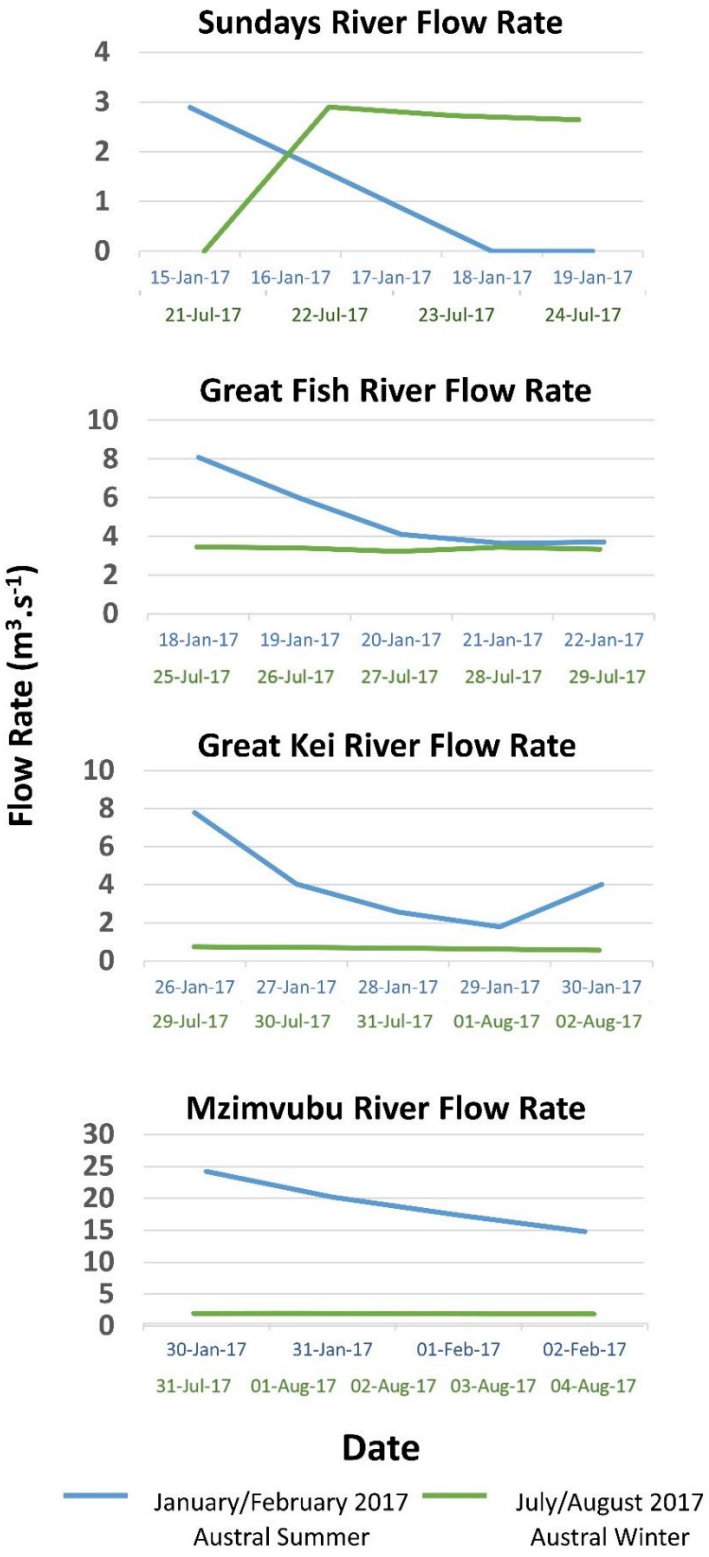

Figure 4.30 River flow rates for the days leading up to the date of sampling, during the January/February (blue) and July/August (green) 2017 cruises, at the Sundays, the Great Fish, the Great Kei and the Mzimvubu Rivers. Relatively higher river flow rates were observed during January/February than during July/August. In comparison to the other rivers, the Mzimvubu River was observed to have the highest river flow rate during January/February.

Moderate rainfall, between 25 and 100 mm, was found to occur in the Mzimvubu River catchment area in the austral summer during the week when site D was sampled (Figure 4.29b-c). This moderate rainfall was found to coincide with the highest river flow rate, ranging between 14 and 24 $m^3.s^{-1}$, at the Mzimvubu River (Figure 4.30d). This high river flow rate resulted in the outflow of a large amount of fresh water into the coastal waters of site D which were found to have an anomalously low salinity of 33.7 g/kg (Figure 4.31).

The Mzimvubu River, during January/February 2017, was found to be the only river that had a noticeable influence on the salinity of the surrounding coastal waters. Using the salinity value of 35.27 g/kg to distinguish river influenced water (according to Lamont et al. (2016)), the influence of the Mzimvubu river was found to be confined to the upper 11 m of the water column and dispersed within 2.8 km from the river mouth. The low or lack of rainfall in the catchment areas of the Sundays, Great Fish and Great Kei Rivers, during both the January/February and July/August 2017 cruises as well as in the catchment area of the Mzimvubu river during the July/August 2017 cruise, resulted in low river flow rates that had little or no influence on the surrounding coastal waters.

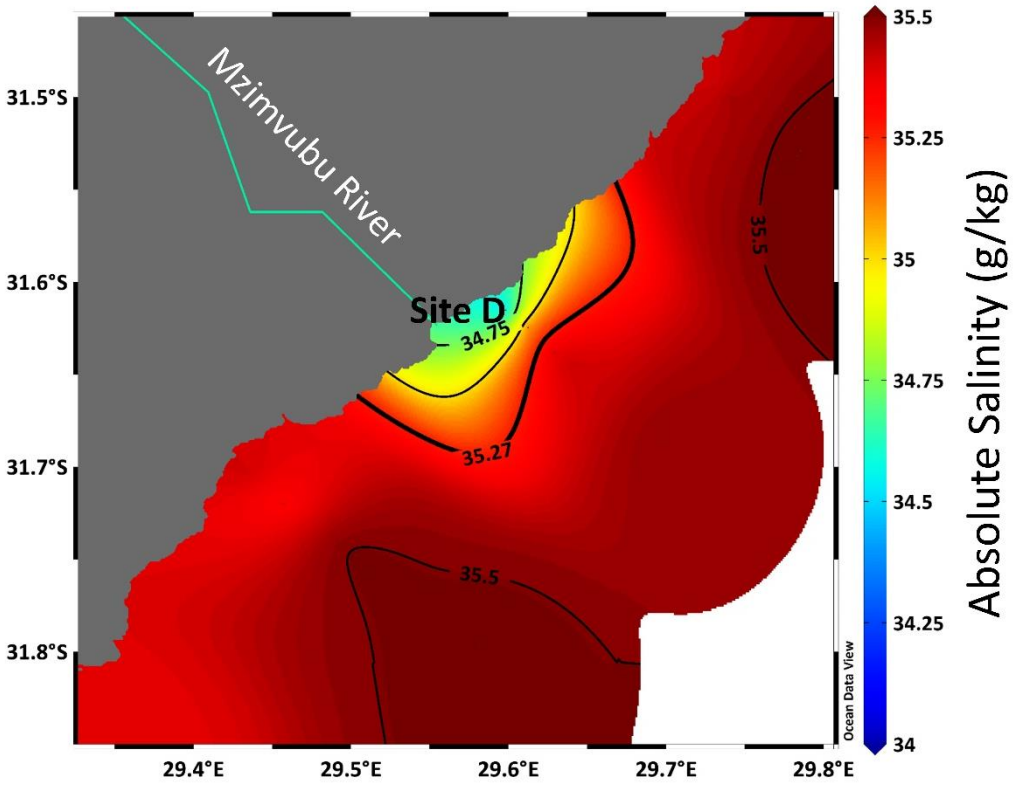

Figure 4.31 Surface salinity map of the coastal waters near the Mzimvubu River mouth, highlighting the low (33.7 g/kg) salinities at site D as a result of freshwater input.

4.10 Case Study 5: Ekman veering of the Agulhas Current

The low temperatures observed throughout the water column at site A (Figure 4.25a), during the January/February 2017 cruise, and at sites E and F (Figure 4.27a-b), during the July/August 2017 cruise, were as a result of the uplift and advection associated with the presence of the January/February and the July/August 2017 cyclonic eddies, respectively, as well as the influence of wind-driven offshore Ekman transport allowing the water to break the surface. The influence that the eddies had on the temperature throughout the water column is clearly illustrated vertical temperature sections in Figure 4.25a and Figure 4.27a-b, where the low temperatures observed inshore are linked to the low temperatures observed offshore. The low temperatures observed inshore, throughout the water column at site C however, were not linked to the low temperatures observed offshore (Figure 4.25c). While the wind-driven upwelling allowed for the low temperature water to break the surface at site C, another process was responsible for the presence of this low temperature water inshore on the shelf. The aim of this case study is therefore to investigate whether the cold water inshore at Port Alfred (site C) is as a result of Ekman veering in the bottom boundary layer of the Agulhas Current. In order to investigate the presence of Ekman veering, vertical temperature sections were plotted for the four transects north of Port Alfred (site C).

Figure 4.32e clearly illustrates that there is little to no link between the low temperatures observed inshore, at site C, with those observed offshore. The downstream location of the January/February cyclonic eddy from Port Alfred, as well as its limited north-eastward extent, suggests that it was not responsible for the uplift and advection of the low temperature non-shelf water onto the shelf and into the region of site C. The low temperature water, observed at site C (Figure 4.32e), was therefore uplifted onto the shelf and advected south-westward with the flow of the Agulhas Current from a location upstream. Upon investigation of the temperature sections upstream of Port Alfred, the link between the low temperatures observed inshore with those observed offshore was found to increase in intensity with every upstream transect illustrated in Figure 4.32. Current spirals at the shelf break at the four transects north of Port Alfred indicate that shoreward movement in the bottom boundary layer was observed only at the fourth transect north of Port Alfred and not at the other transects (Figure A.8).

The shoreward sloping of the isotherms (Figure 4.32) could be the result of inherent inclined density structure associated with a WBC or as a result of Ekman veering in

the BBL as both of these would result in upslope movement cold Central Water from depth. Figure A.4 illustrates how the 26.4 $kg.m^{-3}$ neutral density contour, indicating the boundary between SICW and STSW, extends shoreward between East London and Port Alfred and Figure 4.32 illustrates how Ekman veering resulted in the 300 m uplift of SICW, from 350 m to 50 m. The general south-westward flow that existed on the shelf (discussed in section 4.1.1) resulted in the downstream transport of the uplifted low temperature non-shelf water into the vicinity of site C. It cannot be confirmed that this occurred in July/August cruise because a cyclonic eddy was located in that region, likely overshadowing uplift associated with Ekman veering or the inherent inclined density structure of WBCs.

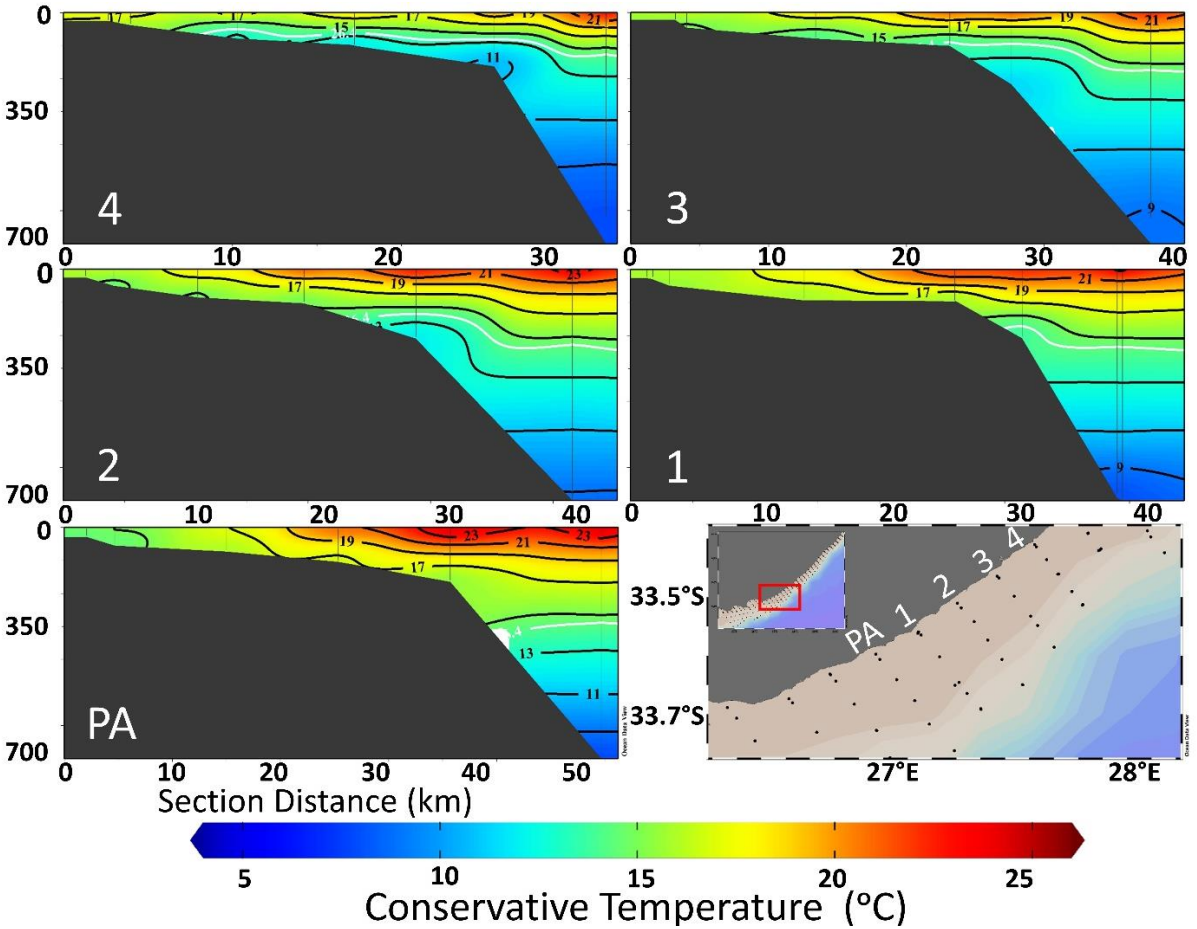

Figure 4.32 Vertical temperature sections, overlaid with the 26.4 kg.m^{-3} neutral density contour (white) representative of the upper limit of South Indian Central Water, depict possible Ekman veering in the bottom boundary layer upstream of Port Alfred and subsequent southward advection of this upwelled water to the location off Port Alfred. The map indicates the location of the five plotted transects as well as their location within the study area.

5. Discussion

The results presented in this thesis have provided an insight into the physical oceanography of the southeast African shelf and slope. The use of both satellite and *in situ* data has allowed for a more comprehensive analysis of the larger and smaller scale processes as well as the features present on the shelf and slope during January/February and July/August 2017. In order to fulfil the aim of this study, which seeks to describe the physical processes and oceanographic conditions of the southeast African shelf, the previously posed key questions are discussed and answered below.

5.1 What are the physical oceanographic processes occurring in January/February and July/August 2017 on the southeast African shelf and how do they differ?

5.1.1 Upwelling

Kämpf and Chapman (2016) and Schumann et al. (1982) have described upwelling as the upward movement of water parcels within the water column, resulting in the presence of relatively colder water in the surface layers where relatively warmer water generally exists. The satellite and *in situ* data, investigated in section 4, have allowed for the identification of four different types of upwelling during the January/February and July/August 2017 cruises which took place along the southeast African shelf and slope. The four different types of upwelling, all of which will be discussed in the subsections below, have been categorized as: Ekman pumping, wind-driven upwelling, Ekman veering in the bottom layers and divergence.

5.1.1.1 Ekman Pumping associated with the observed cyclonic eddies

The upwelling or downwelling observed at the centre of cyclonic and anticyclonic eddies respectively, is known as Ekman pumping (Gaube et al., 2015). While the Ekman pumping observed at the centre of anticyclonic eddies results in a deepening of the thermocline, the Ekman pumping observed at the centre of cyclonic eddies results in the uplift of the thermocline resulting in the uplift of cold, deep, nutrient-rich water seen in Figure 2.6 (Goble et al., 2014, Krug et al., 2014).

5.1.1.1.1 Ekman Pumping in the Upper Layers

This study observed the presence of a cyclonic eddy along the inshore edge of the Agulhas Current during both the January/February (Figure 4.1b) and July/August cruises (Figure 4.3b). The passage of cyclonic eddies on the inshore edge of the Agulhas Current is not uncommon (Lutjeharms, 2006a). Two types of cyclonic eddies are known to propagate downstream along the inshore edge of the Agulhas Current and they are the Natal Pulse and the Durban Eddy (Lutjeharms and Roberts, 1988, Lutjeharms, 2006a, Roberts, 2010). The Natal Pulse originates at the KwaZulu-Natal (KZN) Bight and its formation has been found occasionally to be complimented by the absorption of deep-sea eddies along the offshore edge of the Agulhas Current (Lutjeharms and Roberts, 1988, Lutjeharms, 2006a). Durban Eddies form at the southern extreme of the KZN Bight at a smaller subsurface bight near Durban (Roberts et al., 2010).

As Natal Pulses and Durban Eddies propagate downstream, they have been found to evolve differently. While Natal Pulses grow to up to 200 km in a seaward extent (Lutjeharms, 2006a), Durban Eddies have been found to flatten and become elongated against the shelf (Roberts et al., 2010). As discussed in the results in section 4.1, the characteristics of the two eddies observed in this study, in Figure 4.1b and Figure 4.3b, resemble those of Natal Pulses. The tracking of these eddies represented in (Figure A.1 and Figure A.2) confirm that they indeed are Natal Pulses as they originated at the KZN Bight. The formation of both the January/February and July/August cyclonic eddies was complimented by the interaction of deep-sea anticyclonic eddies along the offshore edge of the Agulhas Current near the KwaZulu-Natal (KZN) Bight, similar to the observations of Lutjeharms and Roberts (1988). While this study considers both the January/February and July/August cyclonic eddies to be Natal Pulses, if the criteria given by Rouault and Penven (2011) for the detection of Natal Pulses was used, only the July/August eddy would have been considered to be a Natal Pulse. The January/February cyclonic eddy would not have been considered as a Natal Pulse because it did not meet one of the two criterion given by Rouault and Penven (2011), such that it did not result in the 30 km meander of the Agulhas Current from its mean position at the KZN Bight.

As a result of the cyclonic eddy presence during both the January/February and July/August cruises, the effect of Ekman pumping was observed. During the January/February cruise, the cyclonic eddy resulted in the uplift of cold and less saline non-shelf water onto the shelf, between St Francis Bay and Algoa Bay. This

is illustrated by the location of the 10 ^{o}C isotherm inshore, in Figure 4.5b and Figure 4.18b, and by the 34.9 g/kg isohaline in Figure 4.6b. The absence of a cyclonic eddy, between St Francis Bay and Algoa Bay, during the July/August cruise, resulted in the observation of relatively higher temperatures (15 ^{o}C; Figure 4.5d) and salinities (35.3 g/kg; Figure 4.6d) close to the coast, while the 10 ^{o}C isotherm was observed further offshore, between 500-600 db (Figure A.5a-b). In contrast to the January/February eddy, the influence of the July/August cyclonic eddy on temperature and salinity was not as obvious but nevertheless it still resulted in cooling. This is illustrated by the inshore location of relatively lower temperatures (<15 ^{o}C; Figure 4.5d and Figure 4.20b) and salinities (35.3 g/kg; Figure 4.6d) between Port Alfred and East London and is also confirmed by the bottom neutral densities (Figure A.4).

Since cyclonic eddies are associated with the uplift of nutrient-rich central waters (Bakun, 2017, Pivan et al., 2016), it can be expected that the waters present on the shelf regions influenced by the cyclonic eddies, are central waters with elevated nutrient concentrations and relatively lower dissolved oxygen (DO) levels. This was the situation during both January/February and July/August cruises, where South Indian Central Water (SICW) was observed on the shelf in the regions impacted by the January/February and July/August eddies, respectively (Figure A.4a-b). During January/February, the central water that was uplifted onto the shelf by the eddy, between St Francis Bay and Algoa Bay, was colder, had relatively low DO levels and had a higher nutrient content than the surrounding waters and this is well represented by the silicate, nitrate, phosphate and nitrite concentrations seen in Figure 4.10b, Figure 4.11b, Figure 4.12b and Figure 4.13b respectively. The water uplifted onto the shelf by the July/August cyclonic eddy was also colder, with relatively low DO levels and an elevated nutrient content with regards to the surrounding waters but to a lesser extent than those influenced by the January/February cyclonic eddy as can be seen in Figure 4.10d, Figure 4.11d and Figure 4.12d. While the DO levels were lower than the surrounding waters during both January/February and July/August, according to the criteria given by Monteiro and van der Plas (2006) for the ecological consequences of different oxygen states, the DO levels on the shelf were found to be in the range where the biological response is insignificant which suggests that the DO levels were adequate in facilitating the survival of the existing shelf biology. The difference in the temperature, DO levels and nutrient content of the water that was upwelled onto the shelf by the January/February and July/August eddies, can likely be attributed to the

difference in depth from which the water was upwelled, with the January/February eddy uplifting SICW from a deeper depth than the July/August eddy. Elevated nutrient concentrations of the inshore shelf waters associated with the presence of a cyclonic eddy, have been similarly documented in other western boundary currents, like the Brazil Current (Brandini, 1990) and the East Australian Current (Doblin et al., 2016).

The results from this study indicate that the January/February cyclonic eddy had a more intense impact on the shelf waters than the July/August cyclonic eddy with regards to the effect on temperature, salinity and nutrients, as previously discussed. Since cyclonic eddies are upwelling favourable at their core, as a result of Ekman Pumping (Roughan et al., 2017), the location of the core of the cyclonic eddy with regards to the shelf-edge is suggested to be the cause for the differing impact that these eddies had on the shelf waters during the two cruises. The near-slope position of the January/February eddy core resulted in stronger uplift between St Francis Bay and Algoa Bay (depicted by the shoreward sloping 10 ^{o}C isotherm in Figure 4.25a), in comparison to the relatively weaker uplift observed during July/August, along the shelf between Cape Padrone and East London (depicted by the shoreward sloping 15 ^{o}C isotherm in Figure 4.27b). Leber and Beal (2015) investigated a Natal Pulse during April 2010, in the similar region as the July/August eddy of this current study which was also a similar size to the July/August eddy (Figure A.6). Unlike the July/August eddy, the Leber and Beal (2015) eddy was situated closer to the slope and coast, with its core located along the 2000 m isobath (Figure A.6). The near-slope position of the Leber and Beal (2015) eddy was found to have a similar impact on the shelf waters much like that of the January/February eddy of this study, as it also resulted in the uplift of 10 to 12 ^{o}C water onto the shelf. Pivan et al. (2016) also investigated a Natal Pulse, similar in size and location to both the July/August eddy and the Leber and Beal (2015) eddy. The Pivan et al. (2016) eddy was also positioned against the slope and close to the coast, with its core located along the 2000 m isobath (Figure A.6), which had a similar but more intense influence on the shelf waters than the January/February eddy and the Leber and Beal (2015) eddy, such that it had uplifted 9 to 10 ^{o}C water onto the shelf. Thus, the limited influence of the July/August eddy on the shelf in this study was probably due to its location further offshore.

5.1.1.1.2 Ekman Pumping in the Intermediate Layers

In addition to the influencing the upper waters, the cyclonic eddies were also found to influence intermediate waters. Red Sea Water (RSW) is generally located along the inshore edge of the Agulhas Current while Antarctic Intermediate Water (AAIW) is generally located along the offshore edge of the Agulhas Current (Beal et al., 2006). Unlike Beal et al. (2006), AAIW was observed at the stations located along the 1000 m isobath, in the region impacted by the January/February cyclonic eddy, between St Francis Bay and Algoa Bay, whereas RSW was observed at the 1000 m isobath stations, not impacted by the cyclonic eddy (Figure 4.21a-c). Similarly, AAIW was observed during the July/August cruise at the 1000 m isobath stations which were impacted by the cyclonic eddy and RSW was observed at the stations which were not impacted by the eddy, which can be seen in Figure 4.22a-c. A study investigating a Natal Pulse, during June/July 1988, along the southeast African shelf, carried out by Pivan et al. (2016), similarly observed the presence of AAIW along the inshore edge of the Agulhas Current. Although Pivan et al. (2016) had similar findings to this study, they were unable to definitively explain the reason behind the presence of AAIW along the inshore edge of the Agulhas Current and suggested that it was due to seasonality of the inshore/offshore extent of AAIW. Pivan et al. (2016) observed an eddy during the austral winter and this study observed an eddy during the austral summer and another during the austral winter. Since all three eddies were found to have a similar influence on the AAIW, regardless of season, it is unlikely that seasonality is the cause of the presence of AAIW along the inshore edge of the Agulhas Current. Furthermore, the current study found that the AAIW on the inshore edge of the Agulhas Current was confined to the stations impacted by the cyclonic eddy.

Ekman pumping is expected to impact the intermediate layers due to the deep reaching influence of cyclonic eddies as described by Lutjeharms et al. (2001). Since Ekman pumping is responsible for uplift in the water column (Goble et al., 2014, Krug et al., 2014), resulting in the presence of central waters in the usual depth of surface waters, the uplift of intermediate water masses can also be expected, which would result in the presence of deeper waters at the usual depth of the intermediate waters. In this regard, it is unlikely that Ekman pumping is responsible for the absence/presence of RSW/AAIW along the inshore edge of the Agulhas Current, since both of these water masses are located within the same density range (see Table 2.1).Therefore Ekman pumping within the intermediate layer does not fully

explain the presence of the AAIW at the stations impacted by the eddies. Beal et al. (2006) suggested that the position of the kinematic steering level (KSL) within the water column of the Agulhas Current is responsible for either inhibiting or promoting the movement and mixing of intermediate water masses within the intermediate layer. The KSL is found at the depth in the water column where the speed of the current is equal to the phase speed of a passing meander/eddy (Beal et al., 2006). In the absence of an eddy, intermediate water masses would remain on their respective sides of the Agulhas Current because the KSL is essentially situated at the bottom of the water column as a result of the phase speed of the eddy being equal to zero (Leber and Beal, 2015). The KSL in the Agulhas Current is typically found between 1200 and 2500 m, thus allowing for the free movement and mixing of the deep water masses only (Beal et al., 2006). The passage of meanders results in the uplift of the KSL into the intermediate layer allowing for the free movement and mixing of the intermediate water masses, such as RSW and AAIW, from either side of the Agulhas Current (Leber and Beal, 2015). Applying the reasoning of Beal et al. (2006) and Leber and Beal (2015) to this current study, it can be suggested that the KSL was uplifted within the intermediate layer during both January/February and July/August cruises, which allowed for the movement and mixing of the intermediate water masses within the intermediate layer which explains the presence of more AAIW than RSW at the stations impacted by the eddies.

5.1.1.2 Wind-Driven Upwelling on the southeast African shelf

The interaction of the wind stress, imposed by the overlying winds, with the ocean surface results in the cooling of the surface waters (Leber et al., 2017) in two ways. The first is via offshore Ekman transport of the surface water, which is the 90^{o} deflection of the net surface transport to the left of the overlying wind in the southern hemisphere (Kämpf and Chapman, 2016). The offshore Ekman transport results in divergence along the coast that is compensated for by the upwelling of colder lower layer water (Kämpf and Chapman, 2016, Leber et al., 2017). The second way is via the generation of turbulence by the overlying winds within the water column which induces the vertical mixing of water masses (Xing and Davies, 2002). Both of these processes result in the uplift of subsurface water with a higher nutrient content into the euphotic zone fuelling primary production which is essential for the survival of aquatic food webs (Kämpf, 2017).

5.1.1.2.1 Offshore Ekman Transport

As a result of the northeast/southwest orientation of the coastline between Port Shepstone and Port Alfred and the east/west orientation of the coastline between Port Alfred and Cape St Francis, north-easterly and easterly longshore winds, respectively, are considered as upwelling favourable (Schumann et al., 1982, Leber et al., 2017). As a result of the seasonal migration of the atmospheric high pressure systems (Taljaard, 1972), westerly component winds are dominant during the austral winter whereas upwelling favourable, north-easterly and easterly winds, are dominant during the austral summer (Schumann et al., 1982). Therefore, the frequency of upwelling driven by offshore Ekman transport along this coastline can be expected to be higher during the austral summer than during the austral winter.

Since this study investigated one cruise during the austral summer and another during the austral winter, the seasonality of the upwelling was expected to have been clearly observed but this was not the case. Two sites of upwelling, induced by offshore Ekman transport, were observed during each of the cruises (Figure 4.23a and c). As described in the results (sections 4.2 and 4.8), upwelling was observed at sites A (Cape Recife) and C (Port Alfred) during the January/February cruise (Figure 4.5a and Figure 4.23a) and at sites E (Port Alfred) and F (west of East London) during the July/August cruise (Figure 4.5c and Figure 4.23b). Upwelling favourable winds were present at all of the sites prior to and on the days of sampling which resulted in the cooler and relatively less saline lower layer water breaking the surface. Surface temperatures at sites C and E were 15.3 ^{o}C and 14.5 ^{o}C (Table 4.1), respectively, while those at sites A and F were substantially lower (10.7 ^{o}C and 13.7 ^{o}C respectively; Table 4.1). These temperatures differences were as a result of the upwelling of two different water masses at the various sites. STSW, generally found in the lower layers of the shelf (Lutjeharms, 2006a), was upwelled at sites C and E, while SICW, generally found along the slope between 150 and 800 m depth (Lutjeharms, 2006a), was upwelled at sites A and F. As discussed in the previous section, Ekman pumping associated with the cyclonic eddies, resulted in the uplift and advection of central waters onto the shelf and into the vicinities of sites A and F. The temperature of the SICW upwelled at site A was lower than that of site F, as a result of the near-slope location of the January/February eddy's core, which upwelled SICW from deeper depths onto the shelf, as opposed to the July/August eddy's core which was located further offshore, which upwelled SICW onto the shelf from shallower depths (discussed in section 5.1.1.1).

The water upwelled at all four of the sites is considered to be newly upwelled, as a result of the observed upwelling favourable longshore winds prior to and on the day of sampling (Figure 4.24a-f and Figure 4.26a-d). While the nutrient concentrations at all of the four sites were relatively higher than the surrounding waters (Figure 4.10a and c, Figure 4.11a and c, Figure 4.12a and c, Figure 4.13a and c), no biological response was observed with regards to chlorophyll-a (chl-a) concentrations (Figure 4.17a-d). While the biological response (chl-a concentrations) to upwelled water that breaks the surface is generally large (Kämpf and Chapman, 2016), that within newly upwelled water is generally low (Silulwane et al., 2001). Low biological responses at sites of newly upwelled water are either as a result of the upwelled phytoplankton community originating from below the euphotic zone that have not yet had time to respond to the higher light levels at the surface and photosynthesize, or strong and persistent winds inducing rapid offshore transport and subduction of the phytoplankton community (Evans et al., 2015). The most likely reason behind the low chl-a concentrations at all four sites in this study, is that the upwelled phytoplankton community originated form below the euphotic zone and had not yet had time to respond to the higher light levels at the surface and photosynthesize.

5.1.1.2.2 Vertical Mixing

One site of upwelling induced by vertical mixing was identified in this study. As described in the results (sections 4.2 and 4.8), this type of wind-driven upwelling was observed at site B, located west of Cape Padrone in the mid-shelf region during the January/February cruise. Varying winds were present prior to and on the day of sampling at site B (Figure 4.24a-f), which through turbulence-induced vertical mixing resulted in the upward doming of the isotherms within the water column, with 15.3 ^{o}C illustrating STSW breaking the surface (Figure 4.25b). Unlike all of the other upwelling sites (sites A, C, E and F), relatively lower levels of nutrients were observed at the surface at site B. Similar to the other upwelling sites, the dissolved oxygen concentration and subsequent biological response were also relatively low. Turbulence gives rise to the need for the upwelled phytoplankton community to adapt to the varying light conditions in the upper mixed layer which could result in the delay of the biological response (Falkowski and Wirick, 1981). This is most likely the situation that occurred at site B.

5.1.1.3 Ekman veering along the southeast African slope

The upslope and shoreward advection of cold nutrient-rich water that occurs along the shelf-edge is known as Ekman veering in the bottom boundary layer which is governed by the interaction of the current with the slope topography (Leber et al., 2017). Ekman veering in the bottom boundary layer is another type of subsurface upwelling, like the Ekman pumping which is associated with cyclonic eddies, that primes the lower levels of the shelf with cold nutrient-rich water.

This study observed the presence of Ekman veering during the January/February cruise but not during the July/August cruise. It is possible that signal from the Ekman veering during July/August was overshadowed by the signal of the Ekman pumping, associated with the presence of the July/August cyclonic eddy. During January/February, Ekman veering was observed along the slope between Port Alfred and East London which is illustrated by the shoreward sloping subsurface isotherms in Figure 4.32. The Ekman veering observed in the current study was found to have uplifted the SICW by approximately 300 m from below 350 m to 50 m below the surface (Figure 4.32). Although, the sloping of the isotherms could be linked to either the inherent inclined density structure of WBCs or could be a result of Ekman veering, it is suggested that the sloping of the isotherms, described in this study, were as a result of Ekman veering as opposed to the inclined density structures of WBCs.

Similar observations of Ekman veering have been made in the Agulhas Current by Leber et al. (2017) and in the East Australia Current by Roughan and Middleton (2002). As described by Roughan and Middleton (2002), the onshore movement of a WBC accentuates the alongshore current speed and uplifts the isotherms by shifting the inclined density structure shoreward, both of which enhance Ekman veering in the BBL. Enhanced Ekman veering has also been observed as a WBC translates from flowing along a wider shelf to flowing along a narrower shelf, due to the acceleration of the current (Roughan and Middleton, 2002).

In contrast to what was observed in the current study, Goschen et al. (2012) suggested that Ekman veering was a consistent feature that occurred along the entire south-east region. It is possible that the resolution of the data along the shelf-edge in this study was not sufficient to capture the Ekman veering process occurring further north as a result of the changing slope configuration.

The encroachment of a current and its inherent inclined density structure preconditions the isotherms for upwelling and can enhance the process of Ekman veering (Roughan and Middleton, 2002). Given the nearshore presence of the Agulhas Current near East London in January/February (Figure 4.1a and 4.2), it is suggested that the isotherms in the vicinity (Figure 4.32) were preconditioned for upwelling and that the enhancement of Ekman veering in the bottom boundary layer took place.

The Ekman veering that was observed in this study, during January/February, was found to bring relatively colder water onto the shelf which was advected, with the general flow of the Agulhas Current, downstream toward Port Alfred, where the wind-driven upwelling resulted in it breaking the surface. This is confirmed by observations of the currents at the shelf break where shoreward movement was observed only at the fourth transect north of Port Alfred and not at Port Alfred itself (Figure A.8). This scenario effectively illustrates how the wind-driven upwelling was a ‘secondary pump’ to the Ekman veering that occurred subsurface along the shelf which has been similarly described by Lutjeharms (2006a) and (Leber et al., 2017).

5.1.1.4 Divergence-induced upwelling driven by Agulhas Current

Upwelling can also be as a result of the interaction of a current with the underlying bathymetry (Kämpf and Chapman, 2016). As a coastal jet, like a western boundary current (WBC), flows from a narrow shelf to a wider shelf, it gets deflected offshore which induces divergence that results in enhanced upwelling along the inshore edge of the current (Gill and Schumann, 1979, Lutjeharms et al., 2000a). This type of upwelling, independent of the overlying winds (Lutjeharms et al., 1989a), has been observed along the inshore edge of WBCs such as the Gulf Stream (Blanton et al., 1981), the Kuroshio Current (Lutjeharms et al., 1993), the East Australia Current (Oke and Middleton, 2001), as well as the Agulhas Current (Lutjeharms et al., 2000a). There are two locations along the Agulhas Current where this divergence-induced upwelling occurs as a result of the widening shelf: at the northern end of the KZN Bight (Lamont et al., 2016) and off East London (Lutjeharms et al., 2000a).

This study observed the presence of divergence-induced upwelling, as a result of the offshore deflection of the Agulhas Current, at East London. This upwelling was

clearly observed in the satellite sea surface temperature (SST) data during both January/February (Figure 4.4) and July/August (Figure 4.7) 2017 but was less visible (yet still evident) in the *in situ* surface temperature data (Figure 4.5a and c). The influence of the cyclonic eddies in each cruise resulted in either the dampening or enhancement of the effects of the divergence-induced upwelling. The influence of the January/February cyclonic eddy dampened the effect of the divergence-driven upwelling, such that it resulted in the presence of relatively warmer surface temperatures between Cape Recife and Cape St Francis (Figure 4.5a) due to the eddy advecting warm surface Agulhas Current water onto the shelf. In contrast, the earlier offshore deflection of the Agulhas Current associated with the July/August eddy, resulted in the enhancement of the divergence-driven upwelling, such that it was observed to occur closer to Port St Johns than East London (Figure 4.5c). While the influence of this type of upwelling on the biology of the shelf was not determined in this study, previous studies, particularly of the KZN Bight, have found it to have a considerable influence on both the nutrient content as well as the biology of the region (Carter and d'Aubrey, 1988).

5.1.2 Freshwater Input

Oceanic surface salinity modifications in coastal regions occur as a result of high rainfall and subsequent increased river outflow into the upper layers of the coastal ocean (Simpson, 2012, Schumann, 2013). Since the southeast African coast falls within a summer rainfall region (Landman and Goddard, 2002), surface salinities are expected to be relatively low during the austral summer, as a result of the high rainfall and the consequently stronger river outflow (Schumann, 2013). In contrast, during the austral winter, the relatively lower rainfall and subsequently weaker river outflow, have a much smaller influence the surface salinities of the coastal ocean.

A similar surface salinity difference was observed during this study. During January/February, relatively low surface salinities (33.7-35.5 g/kg; Figure 4.6a) were observed. These were much lower than published ranges for oceanic surface water masses (35.3-35.6 psu, Lutjeharms et al., 1996). In contrast, during July/August, a smaller surface salinity range (35.2-35.5 g/kg; Figure 4.6c) was observed, where the minimum value was much higher than that in January/February. The surface salinity values in July/August were well within the ranges reported for TSW and STSW (Lutjeharms and De Ruijter, 1996).

As expected, based on knowledge from previous studies, the relatively higher rainfall during January/February (Figure 4.29a-c), in conjunction with stronger river outflows (Figure 4.30a-d) resulted in relatively low surface salinities (Figure 4.6a). In contrast, the relatively lower rainfall during July/August (Figure 4.29d-f), combined with weaker river outflows (Figure 4.30a-d) which had no obvious impact on the coastal waters, resulted in higher surface salinity values being observed. While the river outflows were overall stronger in January/February than in July/August (Figure 4.30a-d), only one of the six rivers in the study area was found to have had an obvious impact on the surface salinity at the coast. The Mzimvubu River had the highest outflow (14-24 $m^3.s^{-1}$; Figure 4.30d) during January/February which resulted in the freshening of the coastal surface salinities to a minimum of 33.7 g/kg in the vicinity of the river mouth (Figure 4.6a and Figure 4.31). Goschen and Schumann (2011) noted that the influence of river outflow on coastal waters was limited with regards to depth and distance, such that it is confined to the upper few meters of the water column and disperses within 2 km of the outflow. Similarly, the current study found the influence of the river outflow from the Mzimvubu River to be confined to the upper 11 m of the water column (Figure 4.28b) and dispersed within approximately 2.8 km from the coast (Figure 4.28b).

Similar to this study, Lamont et al. (2016) also observed seasonal river outflow and salinity differences in the KwaZulu-Natal (KZN) Bight, during January and July 2010. During January 2010, the Thukela River was found to have an average flow rate greater than 450 $m^3.s^{-1}$, which was found to have influenced the upper 10 m of the water column and dispersed within approximately 27 km from the river mouth (Lamont et al., 2016). The influence of the Thukela River (Lamont et al., 2016) on the coastal waters, extends further offshore than that of the Mzimvubu River (Figure 4.28b) identified in this study. This is likely as a result of the substantially stronger river flow rate of the Thukela River during January 2010, in comparison to that of the Mzimvubu River during January/February 2017. During July 2010, Lamont et al. (2016) found the average river flow rate to be substantially lower, (< 13 m^3s^{-1}) with no apparent influence on the coastal waters. This was also the situation with the river outflow and influence during July/August 2017 in the current study.

Previous studies have shown that surface salinity modifications associated with river outflow, also result in the nutrient loading of the coastal surface waters due to anthropogenic influences of fertilizer seepage and sewage input into rivers (Emmerson, 1989, Nyamangara et al., 2013). Emmerson (1989) observed high

nutrient levels (specifically nitrogen) in the coastal waters near the Sundays River mouth in Algoa Bay, which were as a result of the seepage of fertilizer from the upstream citrus farming. The outflow of nutrient-rich water from rivers into the coastal waters can lead to increased plant biomass which is represented by high chl-a concentrations (Golterman and De Oude, 1991). Elevated nutrient levels were expected to be observed at the Mzimvubu River mouth during January/February 2017 but this was not the case. The nutrient levels of the coastal waters near the river mouth were similar to those of the surrounding oceanic waters (Figure 4.10a, Figure 4.11a, Figure 4.12a and Figure 4.13a). Similarly, van Niekerk et al. (2013) also observed lower than expected nutrient levels in the coastal waters near the Orange River mouth which they attributed to the possible overshadowing by the natural nutrient content of the coastal environment. This is unlikely to be the reason for the low nutrient content near the Mzimvubu River mouth, as the coastal waters in this region are considered to be mesotrophic. Differences in the urban activities and land usage in Mzimvubu River catchment area, as opposed to those within the Sundays and Orange River catchment areas, could most likely be the reason behind the low nutrient input from the Mzimvubu River.

A study of phytoplankton production along the south-east coast of South Africa (Barlow et al., 2010) found low chl-a concentrations in the coastal waters near the Kei River mouth. These low chl-a values were attributed to the significant light attenuation caused by the high sediment load in the water, which stemmed from the Kei River discharge (Barlow et al., 2010). Similarly, the current study observed low chl-a concentrations in the coastal waters near the Mzimvubu River mouth, during January/February (Figure 4.17a-b). Relatively high backscatter readings in the surface layers of the water column near the Mzimvubu River mouth (Figure A.7) suggested high levels of suspended sediment, which following the reasoning of Barlow et al. (2010), could result in the low chl-a concentrations due to the significant light attenuation.

5.1.3 Seasonality along the southeast African shelf

The austral summer months (December, January and February) along the southeast African coast are characterized by high levels of solar insolation and higher rainfall, resulting in relatively high sea surface temperatures and low surface salinities (Schumann, 2013). In contrast, the austral winter months (June, July and August) are characterized by lower levels of solar insolation and rainfall, resulting in lower sea surface temperatures and higher surface salinities (Schumann, 2013). As

previously mentioned, the January/February cruise took place in the austral summer and the July/August cruise took place during the austral winter. The *in situ* data acquired from the two cruises are not fully representative of the seasons during which they took place but rather offer a glimpse of seasonality.

Indications of seasonality were observed in the *in situ* temperature and salinity data of the upper waters (TSW and STSW). This is represented by a 4 ^{o}C difference in surface temperatures between January/February and July/August which was observed in both the *in situ* (Figure 4.5a and c) and satellite (Figure 4.4 and Figure 4.7) data, where higher temperatures were observed during January/February and lower temperatures were observed during July/August. Similar seasonal temperature differences of 4 and 5 ^{o}C were observed in the waters off of the KwaZulu-Natal coast by Schumann (2013) and Lamont et al. (2016), respectively. This study also observed a difference in the surface salinities between the January/February and July/August cruises, where lower salinities were observed in January/February (Figure 4.6a) and higher salinities were observed in July/August (Figure 4.6c), as a response to the seasonal effects of rainfall and river outflow, discussed in the previous section. This study showed no clear indication of seasonality within the lower water masses (SICW, AAIW and RSW). This is most likely due to the fact that unlike the upper waters, which are or have been in recent contact with the atmosphere and its associated seasonal processes (Shillington et al., 2006), the lower waters are not and are thus less likely to be affected by it. While seasonal differences in upwelling favourable winds (Schumann et al., 1982) and subsequent wind-driven upwelling were expected to have been observed between the two cruises, with more upwelling in January/February and less in July/August, as discussed in section 5.1.1.2, no clear indication of this seasonality was observed.

While upwelling favourable winds are dominant during the austral summer (Schumann et al., 1982), stronger winds are dominant during the austral winter which result in deeper mixing (Lutjeharms, 2006a, Lutjeharms et al., 2000a). The results of this study (see Table 4.2), observed stronger (upwelling favourable) winds during the austral summer than during the austral winter. The stronger winds observed during the austral summer resulted in the calculation of deeper Ekman Layer Depths (see Table 4.2) during the austral summer than during the austral winter. It is suggested that the difference between the results of this study and that which has been described Lutjeharms et al. (2000a) is due to the fact that the current study solely focussed on upwelling favourable winds.

While no discernible seasonal variation has been found with respect to the current speeds and volume transport (Lutjeharms, 2006a, Beal et al., 2015), this study was not able to investigate the possible seasonal differences in current speed and volume flux because S-ADCP data was only available for January/February.

While there was little variation in the silicate, nitrate and phosphate concentrations (Figure 4.10, Figure 4.11 and Figure 4.12) between the two cruises, higher nitrite was observed in January/February than in July/August (Figure 4.13). The minimum concentration of nitrite was higher in January/February than in July/August (Figure 4.14d and Figure 4.15d). The difference in nitrite concentrations between the two cruises could be seasonal but as a result of the cruise data only offering snapshots, it cannot be definitively attributed to seasonality. The relatively higher nitrite concentrations observed in January/February could be linked to the biological history of the water (Parsons et al., 2013), rather than to the influence of seasonality.

Differences in chl-a concentrations between the two cruises were observed such that the levels of chl-a were higher in January/February (austral summer) than in July/August (austral winter). Seasonality of chl-a concentrations has been studied by Lamont et al. (2018), who observed chl-a concentrations to peak during the austral autumn and spring, on the southeast African shelf. The chl-a values were slightly higher in the austral winter than in the austral summer (Lamont et al., 2018). In contrast, the opposite pattern was observed in the current study, where higher values were seen in the austral summer than in the austral winter. The presence of the January/February cyclonic eddy, which was responsible for the uplift of nutrient-rich SICW onto the shelf and stimulating phytoplankton growth may have obscured the expected seasonal signal. Lamont et al. (2018) noted a similar dampening of the seasonal chl-a signal as a result of multiple chl-a peaks throughout the year, in response to the rapidly changing hydrographic pattern on the shelf associated with the Agulhas Current and its meanders.

5.2 How are the southeast African shelf and slope influenced by the adjacent Agulhas Current?

Western boundary currents (WBCs) have been found to have a considerable influence on their adjacent shelf systems (Schaeffer and Roughan, 2015, Allen et al., 1983). The Agulhas Current is no exception. The oceanographic conditions on

the southeast African shelf and slope are strongly influenced by the adjacent Agulhas Current (Lutjeharms, 2006a, Beckley and van Ballegooyen, 1992). The changing shelf and slope configuration along the southeast coast of South Africa result in the dominance of varying processes in the specific regions.

The inshore edge of the Agulhas Current was observed in close proximity to the shelf-edge and coast along the narrow shelf, between Port Shepstone and East London, during both the January/February and July/August cruises (Figure 4.1a, Figure 4.2 and Figure 4.3a). This study found the Agulhas Current to have had a considerable influence on the circulation and water properties on the narrow shelf which has been similarly noted in previous literature (Lutjeharms, 2006a). As discussed in section 4.1, the circulation on the narrow shelf mirrored that of the adjacent south-westward flowing Agulhas Current and the waters on the shelf comprised of the upper water masses (TSW and STSW) of the Agulhas Current which had a relatively low nutrient content.

The Agulhas Current flows along the shelf-edge, and off East London, it becomes located at an increasingly further distance offshore (Roberts et al., 2010). This study observed the deflection of the Agulhas Current from the coast, where the shelf begins to widen, near East London, during both the January/February and July/August cruises (Figure 4.1a, Figure 4.2 and Figure 4.3a). This deflection resulted in divergence-induced upwelling that saw the presence of relatively cooler waters along the inshore edge of the Agulhas Current west of East London (Figure 4.4a-l, Figure 4.5a and c, and Figure 4.7a-i). Subsurface upwelling does not necessarily result only in a local response, its effects can be observed further downstream. As discussed in section 5.1.1.3, the presence of Ekman veering, west of East London, resulted in the uplift of cold nutrient-rich central water which was advected downstream toward Port Alfred, with the general south-westward flow of the Agulhas Current, where it broke the surface as a result of offshore Ekman transport (Figure 4.32).

When the Agulhas Current veers from its general trajectory, as a result of a passing cyclonic eddy embedded within a meander (Lutjeharms, 2006a), other dominant processes, such as Ekman pumping and inshore current reversals, are found to influence the shelf. The current study observed the offshore relocation of the Agulhas Current in response to a passing meander during each cruise (Figure 4.1a and Figure 4.3a). As discussed in section 5.1.1.1, the Ekman pumping associated with the passing cyclonic eddies resulted in the uplift of cold and nutrient-rich SICW

onto the shelf. The degree to which the shelf waters were influenced by the passing eddies, discussed in section 5.1.1.1, was found to be related to the size and location of the cyclonic eddies. Temporary inshore counter currents (Roberts et al., 2010), in addition to the Ekman pumping, have been observed with the passage of cyclonic eddies. This study also observed the presence of these inshore counter currents in the vicinity of the cyclonic eddies during the January/February (Figure 4.2) and July/August (Figure 4.3a) cruises. While the influence of these counter currents on the biology was not investigated in this study, previous work (Roberts, 2010) has established that they have a considerable biological influence, specifically with regards to the northward migration of the sardines.

While the peak period of the sardine run typically occurs during the winter period from May to late June, it is possible for it to persist later on in the year, as late as September (Fréon et al., 2010, O'Donoghue et al., 2010). Therefore, the combination of the lower sea surface temperatures in winter (Figure 4.5c) and the northward flowing counter currents associated with the July/August cyclonic eddy (Figure 4.3b) could have been conducive in assisting the northward migration of the sardine in 2017. The knowledge gained from this study provides a baseline of the environmental conditions present on the shelf which can be applied to investigations focussing on the shelf biology. It possible that the presence of sardine eggs in the region during January months (Fennessy et al., 2010) could be as a result of the downstream propagating cyclonic eddies present at those times. These eddies, like the January/February eddy observed in this study, could possibly assist the sardine throughout the year.

The observations from this study showed that organisms within MPAs along the shelf were likely to be subjected to large ranges in temperature, from high bottom temperatures (>17 °C) when the Agulhas Current is in its usual position, impinging on the shelf (Figure 4.1 and 4.5), to very low temperatures (<10°C) associated with upwelling during the passage of cyclonic eddies (Figure 4.1 and 4.5). While the exposure of the organisms to low temperatures is short-lived, on the order of only a few days as the eddies propagate southward, variations in temperature can cause compositional changes of the zooplankton community, effecting marine life in the higher trophic levels (Ozaki et al., 2004). Temperature variations have also been shown to influence the dispersal of marine larval species, where lower temperatures result in greater dispersal distances (O'Connor et al., 2007). While temperature is important for both pelagic and demersal spices within the MPA regions, variations

in bottom oxygen concentrations are particularly relevant for demersal species. These bottom oxygen variations can affect the structure and composition of the demersal community, as well as limit individual growth and population productivity, as has been shown for the west coast (Abelló and Macpherson, 1990).

5.3 What water masses are present on the southeast African shelf and slope in January/February and July/August 2017 and what are their properties?

The waters of the southeast African shelf have been characterized by a mixture of TSW and STSW (Lutjeharms et al., 2000a) which has been similarly observed during both the January/February and July/August cruises of this study. Similar to what has been observed in previous studies (Goschen et al., 2012, Bakun, 2017, Pivan et al., 2016, Leber and Beal, 2015), the current study observed subsurface upwelling processes such as Ekman veering in the bottom layers (5.1.1.3) and Ekman pumping associated with cyclonic eddies (section 5.1.1.1), to be responsible for the uplift and advection of the cold nutrient-rich SICW from the slope, onto the shelf. The waters along the southeast African slope comprise of SICW and RSW (Leber and Beal, 2015) which was similarly observed in the current study. As discussed in section 5.1.1.1, passing eddies have been found to enhance the movement of AAIW from the offshore edge of the Agulhas Current to the inshore edge, explaining its presence along the slope during both cruises.

The water masses observed during the two cruises were identified using a combination of water mass characteristics such as temperature, salinity and neutral density ranges seen in Table 2.1. The TSW identified in the current study was found to have a lower temperature minimum (19 ^{o}C) and higher salinity maximum (35.73 g/kg) than those defined by previous studies (Lutjeharms, 2006a, Beal et al., 2006). The STSW observed in this study was found to have a lower temperature minimum (14 ^{o}C) and lower salinity minimum (35.19 g/kg) than those defined by previous studies (Lutjeharms et al., 1996). The difference in temperature and salinity characteristics between the current and previous studies are likely due to differences in prevailing oceanographic conditions at the time of sampling. TSW and STSW during the January/February cruise were found to have relatively higher temperatures and lower salinities, as a result of increased solar insolation and increased freshwater input (see section 5.1.3), which has been similarly observed by Lutjeharms (2006a). In comparison to previous literature (Lutjeharms et al., 1996), the current study observed TSW to have a relatively smaller nutrient

concentration range (0 and 9 µM of silicate, 0 and 11 µM of nitrate, 0 and 2 µM of phosphate and 0.05 and 0.7 µM of nitrite), with lower maximum concentrations and observed STSW to have a relatively larger nutrient concentration range (0 and 13 µM of silicate, 0 and 15 µM of nitrate, 0.05 and 1.75 µM of phosphate and 0 and 0.8 µM of nitrite) with considerably higher maximum values.

The SICW identified in the current study was found within the temperature and salinity ranges given by Lutjeharms (2006a) and Emery and Meincke (1986). The SICW identified in this study was found to have relatively larger nutrient concentration ranges (2 and 24 µM of silicate, 3 and 26 µM of nitrate, 0.2 and 2.2 µM of phosphate and 0 and 0.75 µM of nitrite) with considerably higher maximum concentrations than has been observed in previous studies (Lutjeharms et al., 1996). As mentioned above, subsurface upwelling processes were found to be responsible for the uplift and advection of the nutrient-rich SICW, which is usually found below 400 m (Schumann, 1998, Lutjeharms, 2006a), onto the shelf, above 200 m, during both cruises. The introduction of deeper water masses onto the shelf, as observed in the current study, can have significant impact on the nutrient concentrations and biology of the shelf environment (Carter and d'Aubrey, 1988, Meyer et al., 2002).

RSW and AAIW were observed to have similar temperature and salinity ranges as those given by Lutjeharms (2006a) and Emery and Meincke (1986). As discussed in section 4.4.3, the two intermediate water masses (RSW and AAIW) were found to have the highest nutrient content of all the other observed water masses. The uplift of the kinematic steering level (KSL) associated with the January/February and July/August cyclonic eddies resulted in the uplift of the nutrient-rich RSW and AAIW along the slope but not onto the shelf. Perhaps if a stronger eddy was present, the RSW and AAIW (water masses with the observed highest nutrient content) could be upwelled onto the shelf. While this could be a possibility, there has been no record in the published literature of intermediate water masses on the southeast African shelf.

6. Conclusion and Future Recommendations

The aim of this study was to identify and describe the physical oceanographic processes occurring on the southeast African shelf and slope, as well as the influence that the Agulhas Current has on the shelf waters. This was achieved using high resolution *in situ* data, collected during two hydrographic surveys of the southeast African shelf and slope in January/February and July/August 2017, which was complemented with courser resolution satellite wind, sea surface temperature and altimetry data. The combination of the high resolution *in situ* data with the coarser resolution satellite data used in this study was found to adequately identify both large and smaller scale processes and features present on the southeast African shelf and slope. The results of this study have confirmed previous observations (Leber and Beal, 2015, Goschen et al., 2012, Lutjeharms, 2006a, Lamont et al., 2016) and extended the knowledge of the area by identifying new processes, in particular the influence of cyclonic eddies on intermediate water masses which has not been previously described for this region. This study describes the first high resolution shelf wide hydrographic surveys of the region and provides a baseline of oceanographic conditions during the austral summer and winter (even though they are considered as snapshots). The knowledge gained from this study can be used to influence economic activities linked to fisheries and ecotourism as well as aid the scientific community with future studies of the shelf biology, from identifying favourable conditions that could assist possible sardine runs to investigating how the effects of temperature changes influence the dispersal of demersal and pelagic larvae. The use of the knowledge gained from this study combined with the collaborative effort of the scientific community with governmental departments can result in the better planning and implementation of conservation regulations regarding the Marine Protected Areas (MPAs) of the region.

Insights gained from this study, suggest three ways in which future investigations can enhance knowledge of the area. Firstly the addition of austral spring and autumn *in situ* data (hydrographic surveys), would allow for a more detailed understanding of the processes during the different seasons of the year. Secondly, in addition to the existing river outflow monitors that exist along the southeast coast, the implementation of water quality monitors at the river mouths, as well as in the nearby coastal waters, could aid in determining the influence that river outflow has on the coastal region year round thus contributing to the monitoring of the possible

influence of river outflow on MPAs. Lastly, to further investigate the influence of cyclonic eddies on intermediate water masses, specialised ‘eddy-hunting’ hydrographic surveys could be implemented, which could aid in determining whether all cyclonic eddies result in the presence of Antarctic intermediate water (AAIW) along the inshore edge of the Agulhas Current.

7. Reference List

ABELLÓ, P. & MACPHERSON, E. 1990. Influence of environmental conditions on the distribution of Pterygosquilla armata capensis (Crustacea: Stomatopoda) off Namibia. *South African Journal of Marine Science,* 9**,** 169-175.

ALLEN, J. S., BEARDSLEY, R. C., BLANTON, J., BOICOURT, W. C., BUTMAN, B., COACHMAN, L., HUYER, A., KINDER, T. H., ROYER, T. C. & SCHUMACHER, J. D. 1983. Physical oceanography of continental shelves. *Reviews of Geophysics,* 21**,** 1149-1181.

ASCLME. 2012. *National Marine Ecosystem Diagnostic Analysis. South Africa. Contribution to the Agulhas and Somali Current Large Marine Ecosystems Project (supported by UNDP with GEF grant financing)* [Online]. Available: http://www.asclme.org/MEDA/ZA/South_Africa_MEDA_FINAL-Electronic.pdf [Accessed 5 March 2018].

AVISO, U. H. 1996. Merged topex/poseidon products. *Romonville St-Agne, France***,** 201.

BAKUN, A. 2006. Fronts and eddies as key structures in the habitat of marine fish larvae: opportunity, adaptive response and competitive advantage. *Scientia Marina,* 70**,** 105-122.

BAKUN, A. 2017. Climate change and ocean deoxygenation within intensified surface-driven upwelling circulations. *Philosophical Transactions of the Royal Society A,* 375**,** 20160327.

BARLOW, R. G., LAMONT, T., KYEWALYANGA, M., SESSIONS, H. & MORRIS, T. 2010. Phytoplankton production and physiological adaptation on the southeastern shelf of the Agulhas ecosystem. *Continental Shelf Research,* 30**,** 1472-1486.

BEAL, L. M., CHERESKIN, T. K., LENN, Y. D. & ELIPOT, S. 2006. The sources and mixing characteristics of the Agulhas Current. *Journal of Physical Oceanography,* 36**,** 2060-2074.

BEAL, L. M., DE RUIJTER, W. P. M., BIASTOCH, A., ZAHN, R. & SCOR WCRP IAPSO WORKING GROUP 2011. On the role of the Agulhas system in ocean circulation and climate. *Nature,* 472**,** 429.

BEAL, L. M., ELIPOT, S., HOUK, A. & LEBER, G. M. 2015. Capturing the transport variability of a western boundary jet: Results from the Agulhas Current Time-Series Experiment (ACT). *Journal of Physical Oceanography,* 45**,** 1302-1324.

BEAL, L. M., FFIELD, A. & GORDON, A. L. 2000. Spreading of Red Sea overflow waters in the Indian Ocean. *Journal of Geophysical Research: Oceans,* 105**,** 8549-8564.

BECKLEY, L. E. & VAN BALLEGOOYEN, R. C. 1992. Oceanographic conditions during three ichthyoplankton surveys of the Agulhas Current in 1990/91. *South African Journal of Marine Science,* 12**,** 83-93.

BLANTON, J., ATKINSON, L., PIETRAFESA, L. & LEE, T. 1981. The intrusion of Gulf Stream water across the continental shelf due to topographically-induced upwelling. *Deep Sea Research Part A. Oceanographic Research Papers,* 28**,** 393-405.

BRANDINI, F. P. 1990. Hydrography and characteristics of the phytoplankton in shelf and oceanic waters off southeastern Brazil during winter (July/August 1982) and summer (February/March 1984). *Hydrobiologia,* 196**,** 111-148.

BRYAN, K. & LEWIS, L. 1979. A water mass model of the world ocean. *Journal of Geophysical Research: Oceans,* 84**,** 2503-2517.

BRYDEN, H. L., BEAL, L. M. & DUNCAN, L. M. 2005a. Structure and Transport of the Agulhas Current and Its Temporal Variability. *Journal of Oceanography,* 61**,** 479-492.

BRYDEN, H. L., LONGWORTH, H. R. & CUNNINGHAM, S. A. 2005b. Slowing of the Atlantic meridional overturning circulation at 25 N. *Nature,* 438**,** 655-657.

CAMPOS, E. J. D., VELHOTE, D. & DA SILVEIRA, I. C. A. 2000. Shelf break upwelling driven by Brazil Current cyclonic meanders. *Geophysical Research Letters,* 27**,** 751-754.

CARPENTER, J. H. 1965. The Chesapeake Bay Institute technique for the Winkler dissolved oxygen method. *Limnology and Oceanography,* 10**,** 141-143.

CARRIT, D. E. & CARPENTER, J. H. 1966. Comparison and evaluation of currently employed modifications of the Winkler method for determining oxygen in seawater. A NASCO Report. *Journal of Marine Research,* 24**,** 286-318.

CARTER, R. & D'AUBREY, J. 1988. Inorganic nutrients in Natal continental shelf waters. *In:* SCHUMANN, E. (ed.) *Coastal Ocean Studies off Natal, South Africa.* Berlin: Springer.

CSIR & DEAT. 2005. *Monitoring the State of the Coast in South Africa Towards the State of the Coast Report - A Summary. CSIR Division of Water, Environment and Forestry Technology, Durban. Produced on behalf of the Department Evnironmental Affairs and Tourism, Cape Town. Compiled by C. Will and E. Muller. CSIR Report No. ENV-D-C 2005-037* [Online]. Available: http://41.185.19.82/soer/ckeditor/UserUploadedDocsorImages/State_of_the_Coast_nQOy0_BLVDJ.pdf [Accessed 28 May 2018].

DE RUIJTER, W. P. M., VAN LEEUWEN, P. J. & LUTJEHARMS, J. R. E. 1999. Generation and evolution of Natal Pulses: solitary meanders in the Agulhas Current. *Journal of Physical Oceanography,* 29**,** 3043-3055.

DEPARTMENT OF ENVIRONMENTAL AFFAIRS 2017. Transkei Oceanography Cruise Report, January - February 2017. Cape Town: National Department of Environmental Affairs, African Coelacanth Ecosystems Programme.

DOBLIN, M. A., PETROU, K., SINUTOK, S., SEYMOUR, J. R., MESSER, L. F., BROWN, M. V., NORMAN, L., EVERETT, J. D., MCINNES, A. S., RALPH, P. J., THOMPSON, P. A. & HASSLER, C. S. 2016. Nutrient uplift in a cyclonic eddy increases diversity, primary productivity and iron demand of microbial communities relative to a western boundary current. *PeerJ,* 4**,** e1973.

DUNCOMBE RAE, C. 1991. Agulhas retroflection rings in the South Atlantic Ocean: an overview. *South African Journal of Marine Science,* 11**,** 327-344.

EMERY, W. & MEINCKE, J. 1986. Global water masses-summary and review. *Oceanologica Acta,* 9**,** 383-391.

EMMERSON, W. 1989. The nutrient status of the Sundays River estuary South Africa. *Water Research,* 23**,** 1059-1067.

EVANS, W., HALES, B., STRUTTON, P. G., SHEARMAN, R. K. & BARTH, J. A. 2015. Failure to bloom: Intense upwelling results in negligible phytoplankton response and prolonged CO2 outgassing over the Oregon shelf. *Journal of Geophysical Research: Oceans,* 120**,** 1446-1461.

FALKOWSKI, P. & WIRICK, C. 1981. A simulation model of the effects of vertical mixing on primary productivity. *Marine Biology,* 65**,** 69-75.

FENNESSY, S., PRADERVAND, P. & DE BRUYN, P. 2010. Influence of the sardine run on selected nearshore predatory teleosts in KwaZulu-Natal. *African Journal of Marine Science,* 32**,** 375-382.

FLUHARTY, D., CHRISTIE, P. & MURRAY, M. 2016. Inside Operation Phakisa, South Africa's blue growth initiative that is fast-tracking a new MPA network. *MPA news,* 17**,** 1-8.

FRÉON, P., COETZEE, J., VAN DER LINGEN, C., CONNELL, A., O'DONOGHUE, S., ROBERTS, M., DEMARCQ, H., ATTWOOD, C., LAMBERTH, S. & HUTCHINGS, L. 2010. A review and tests of hypotheses about causes of the KwaZulu-Natal sardine run. *African Journal of Marine Science,* 32**,** 449-479.

GAUBE, P., CHELTON, D. B., SAMELSON, R. M., SCHLAX, M. G. & O'NEILL, L. W. 2015. Satellite observations of mesoscale eddy-induced Ekman pumping. *Journal of Physical Oceanography,* 45**,** 104-132.

GILL, A. 1982. Atmospheric-ocean dynamics. *International Geophysics Series,* 30**,** 662.

GILL, A. & SCHUMANN, E. 1979. Topographically induced changes in the structure of an inertial coastal jet: application to the Agulhas Current. *Journal of Physical Oceanography,* 9**,** 975-991.

GOBLE, B., VAN DER ELST, R. & OELLERMANN, L. 2014. Ugu Lwethu e Our Coast. *A Profile of Coastal KwaZulu-Natal. KwaZulu-Natal Department of Agriculture and Environmental Affairs and the Oceanographic Research Institute, Cedara***,** 202.

GOLTERMAN, H. & DE OUDE, N. 1991. Eutrophication of lakes, rivers and coastal seas. *Water Pollution.* Springer.

GORDON, A. L. 1985. Indian-Atlantic transfer of thermocline water at the Agulhas retroflection. *Science,* 227**,** 1030-1033.

GORDON, A. L., LUTJEHARMS, J. R. & GRÜNDLINGH, M. L. 1987. Stratification and circulation at the Agulhas Retroflection. *Deep Sea Research Part A. Oceanographic Research Papers,* 34**,** 565-599.

GOSCHEN, W. S. & SCHUMANN, E. 2011. The physical oceanographic processes of Algoa Bay, with emphasis on the western coastal region. South African Environmental Observation Network (SAEON).

GOSCHEN, W. S., SCHUMANN, E. H., BERNARD, K. S., BAILEY, S. E. & DEYZEL, S. H. P. 2012. Upwelling and ocean structures off Algoa Bay and the south-east coast of South Africa. *African Journal of Marine Science,* 34**,** 525-536.

GRASSHOFF, K., EHRHARDT, M. & KREMLING, K. 1983. *Methods of seawater analysis,* Weinheim, Germany.

GRÜNDLINGH, M. L. 1980. On the volume transport of the Agulhas Current. *Deep Sea Research Part A. Oceanographic Research Papers,* 27**,** 557-563.

GUASTELLA, L. & ROBERTS, M. 2016. Dynamics and role of the Durban cyclonic eddy in the KwaZulu-Natal Bight ecosystem. *African Journal of Marine Science,* 38**,** S23-S42.

GUPTA, R. S. & DESA, E. 2001. *The Indian Ocean: A Perspective*, CRC Press.

HARRIS, J., LIVINGSTONE, T., PHADIMA, J., SINK, K., FASHEUN, T., BOYD, A. & MFEKA, X. 2014. *Phakisa Initiative : fast-tracking establishment of an effective and representative network of Marine Protected Areas for South Africa*.

HEILEMAN, S., LUTJEHARMS, J. & SCOTT, L. 2008. II-4 Agulhas Current: LME# 30. *In:* SHERMAN, K. & HEMPEL, G. (eds.).

HERZFELD, M. & TOMCZAK, M. 1999. Bottom-driven upwelling generated by eastern intensification in closed and semi-closed basins with a sloping bottom. *Marine and Freshwater Research,* 50**,** 613-627.

HUTCHINGS, L. 1994. The Agulhas Bank: a synthesis of available information and a brief comparison with other east-coast shelf regions. *South African Journal of Science,* 90**,** 179-185.

HUTCHINGS, L., MORRIS, T., VAN DER LINGEN, C., LAMBERTH, S., CONNELL, A., TALJAARD, S. & VAN NIEKERK, L. 2010. Ecosystem considerations of the KwaZulu-Natal sardine run. *African Journal of Marine Science,* 32**,** 413-421.

IMAWAKI, S., BOWER, A. S., BEAL, L. & QIU, B. 2013. Western Boundary Currents. *Ocean Circulation and Climate.* Elsevier.

IOC, SCOR & IAPSO 2010. The international thermodynamic equation of seawater – 2010: Calculation and use of thermodynamic properties. *Intergovernmental Oceanographic Commission* Manuals and Guides No. 56**,** 196.

JACKETT, D. R. & MCDOUGALL, T. J. 1997. A neutral density variable for the world's oceans. *Journal of Physical Oceanography,* 27**,** 237-263.

KALNAY, E., KANAMITSU, M., KISTLER, R., COLLINS, W., DEAVEN, D., GANDIN, L., IREDELL, M., SAHA, S., WHITE, G. & WOOLLEN, J. 1996. The NCEP/NCAR 40-year reanalysis project. *Bulletin of the American meteorological Society,* 77**,** 437-471.

KÄMPF, J. 2017. Wind-Driven Overturning, Mixing and Upwelling in Shallow Water: A Nonhydrostatic Modeling Study. *Journal of Marine Science and Engineering,* 5**,** 47.

KÄMPF, J. & CHAPMAN, P. 2016. The Functioning of Coastal Upwelling Systems. *Upwelling Systems of the World.* Springer.

KRUG, M. & TOURNADRE, J. 2012. Satellite observations of an annual cycle in the Agulhas Current. *Geophysical Research Letters,* 39.

KRUG, M., TOURNADRE, J. & DUFOIS, F. 2014. Interactions between the Agulhas Current and the eastern margin of the Agulhas Bank. *Continental Shelf Research,* 81**,** 67-79.

LACHAT INSTRUMENTS 2012. Methods list for automated ion analyzers (flow injection analyses, ion chromatography). Loveland, CO: Lachat Instruments.

LAMONT, T. 2017. *A cyclonic eddy sampled by MOCCA floats in the Transkei shelf ecosystem of South Africa* [Online]. Available: http://www.euro-argo.eu/News-Meetings/News/Latest-News/MOCCA-floats-in-the-Transkei-shelf-ecosystem-of-South-Africa [Accessed 23 February 2018].

LAMONT, T., BREWIN, R. J. W. & BARLOW, R. G. 2018. Seasonal variation in remotely-sensed phytoplankton size structure around southern Africa. *Remote Sensing of Environment,* 204**,** 617-631.

LAMONT, T., VAN DEN BERG, M. A. & BARLOW, R. G. 2016. Agulhas Current Influence on the Shelf Dynamics of the KwaZulu-Natal Bight. *Journal of Physical Oceanography,* 46**,** 1323-1338.

LANDMAN, W. A. & GODDARD, L. 2002. Statistical recalibration of GCM forecasts over southern Africa using model output statistics. *Journal of Climate,* 15**,** 2038-2055.

LEBER, G. M. & BEAL, L. M. 2014. Evidence that Agulhas Current transport is maintained during a meander. *Journal of Geophysical Research: Oceans,* 119**,** 3806-3817.

LEBER, G. M. & BEAL, L. M. 2015. Local water mass modifications by a solitary meander in the Agulhas Current. *Journal of Geophysical Research: Oceans,* 120**,** 4503-4515.

LEBER, G. M., BEAL, L. M. & ELIPOT, S. 2017. Wind and current forcing combine to drive strong upwelling in the Agulhas Current. *Journal of Physical Oceanography,* 47**,** 123-134.

LEEUWEN, P. J., RUIJTER, W. P. M. & LUTJEHARMS, J. R. E. 2000. Natal pulses and the formation of Agulhas rings. *Journal of Geophysical Research: Oceans,* 105**,** 6425-6436.

LUDWIG, W. J., NAFE, J. E., SIMPSON, E. S. W. & SACKS, S. 1968. Seismic-refraction measurements on the Southeast African Continental Margin. *Journal of Geophysical Research,* 73**,** 3707-3719.

LUTJEHARMS, J., GRUNDLINGH, M. & CARTER, R. 1989a. Topographically induced upwelling in the Natal Bight. *South African Journal of Science,* 85**,** 310-316.

LUTJEHARMS, J., PENVEN, P. & ROY, C. 2003. Modelling the shear edge eddies of the southern Agulhas Current. *Continental Shelf Research,* 23**,** 1099-1115.

LUTJEHARMS, J. R. E. 2006a. *The Agulhas Current*, Springer Science & Business Media.

LUTJEHARMS, J. R. E. 2006b. The coastal oceans of south-eastern Africa (15 °W). *In:* ROBINSON, A. R. & BRINK, K. H. (eds.) *The Sea.* Cambridge, MA: Harvard University Press.

LUTJEHARMS, J. R. E. 2007. Three decades of research on the greater Agulhas Current. *Ocean Science,* 3**,** 129-147.

LUTJEHARMS, J. R. E. & ANSORGE, I. J. 2001. The Agulhas Return Current. *Journal of Marine Systems,* 30**,** 115-138.

LUTJEHARMS, J. R. E., BOEBEL, O., VAART, P. C. F., RUIJTER, W. P. M., ROSSBY, T. & BRYDEN, H. L. 2001. Evidence that the Natal Pulse involves the Agulhas Current to its full depth. *Geophysical Research Letters,* 28**,** 3449-3452.

LUTJEHARMS, J. R. E., CATZEL, R. & VALENTINE, H. R. 1989b. Eddies and other boundary phenomena of the Agulhas Current. *Continental Shelf Research,* 9**,** 597-616.

LUTJEHARMS, J. R. E., COOPER, J. & ROBERTS, M. 2000a. Upwelling at the inshore edge of the Agulhas Current. *Continental Shelf Research,* 20**,** 737-761.

LUTJEHARMS, J. R. E. & DE RUIJTER, W. P. M. 1996. The influence of the Agulhas Current on the adjacent coastal ocean: possible impacts of climate change. *Journal of Marine Systems,* 7**,** 321-336.

LUTJEHARMS, J. R. E., DURGADOO, J. V., SCHAPIRA, M. & MCQUAID, C. D. 2010. First oceanographic survey of the entire continental shelf adjacent to the northern Agulhas Current. *South African Journal of Science,* 106**,** 1-3.

LUTJEHARMS, J. R. E., LIU, C.-T., CHUAN, W.-S. & SHYU, C.-Z. 1993. On some similarities between the oceanic circulations off Southern Africa and off Taiwan. *South African Journal of Science,* 89**,** 367-371.

LUTJEHARMS, J. R. E., MEYER, A. A., ANSORGE, I. J., EAGLE, G. A. & ORREN, M. J. 1996. The nutrient characteristics of the Agulhas Bank. *South African Journal of Marine Science,* 17**,** 253-274.

LUTJEHARMS, J. R. E. & ROBERTS, H. R. 1988. The Natal pulse: An extreme transient on the Agulhas Current. *Journal of Geophysical Research: Oceans,* 93**,** 631-645.

LUTJEHARMS, J. R. E., VALENTINE, H. R. & VAN BALLEGOOYEN, R. C. 2000b. The hydrography and water masses of the Natal Bight, South Africa. *Continental Shelf Research,* 20**,** 1907-1939.

LUTJEHARMS, J. R. E. & VAN BALLEGOOYEN, R. C. 1988. The retroflection of the Agulhas Current. *Journal of Physical Oceanography,* 18**,** 1570-1583.

MATANO, R., BEIER, E., STRUB, P. & TOKMAKIAN, R. 2002. Large-scale forcing of the Agulhas variability: The seasonal cycle. *Journal of Physical Oceanography,* 32**,** 1228-1241.

MCCARTHY, T. S. 2011. The impact of acid mine drainage in South Africa. *South African Journal of Science,* 107**,** 01-07.

MCDOUGALL, T. J. & BARKER, P. M. 2011. Getting started with TEOS-10 and the Gibbs Seawater (GSW) oceanographic toolbox. *SCOR/IAPSO WG,* 127**,** 1-28.

MCDOUGALL, T. J., FEISTEL, R., MILLERO, F. J., JACKETT, D. R., WRIGHT, D. G., KING, B. A., MARION, G. M., CHEN, C., SPITZER, P. & SEITZ, S. 2009. The International Thermodynamic Equation Of Seawater 2010 (TEOS-10): Calculation and Use of Thermodynamic Properties. *Global Ship-based Repeat Hydrography Manual, IOCCP Report No,* 14.

MERTZ, F., PUJOL, M.-I. & FAUGÈRE, Y. 2018. Product User Manual for Sea Level SLA products 4.

MEYER, A. A., LUTJEHARMS, J. R. E. & DE VILLIERS, S. 2002. The nutrient characteristics of the Natal Bight, South Africa. *Journal of Marine Systems,* 35**,** 11-37.

MONTEIRO, P. M. S. & VAN DER PLAS, A. K. 2006. 5 Low oxygen water (LOW) variability in the Benguela system: Key processes and forcing scales relevant to forecasting. *Large Marine Ecosystems.* Elsevier.

MORRIS, T., HERMES, J., BEAL, L. M., DU PLESSIS, M., DUNCOMBE RAE, C., GULEKANA, M., LAMONT, T., SPEICH, S., ROBERTS, M. & ANSORGE, I. J. 2017. The importance of monitoring the Greater Agulhas Current and its inter-ocean exchanges using large mooring arrays. *South African Journal of Science,* 113**,** 1-7.

MURPHY, J. & RILEY, J. P. 1962. A modified single solution method for the determination of phosphate in natural waters. *Analytica Chimica Acta,* 27**,** 31-36.

NYAMANGARA, J., JEKE, N. & RURINDA, J. 2013. Long-term nitrate and phosphate loading of river water in the Upper Manyame Catchment, Zimbabwe. *Water SA,* 39**,** 637-642.

O'CONNOR, M. I., BRUNO, J. F., GAINES, S. D., HALPERN, B. S., LESTER, S. E., KINLAN, B. P. & WEISS, J. M. 2007. Temperature control of larval dispersal and the implications for marine ecology, evolution, and conservation. *Proceedings of the National Academy of Sciences,* 104**,** 1266-1271.

O'DONOGHUE, S., DRAPEAU, L. & PEDDEMORS, V. 2010. Broad-scale distribution patterns of sardine and their predators in relation to remotely sensed environmental conditions during the KwaZulu-Natal sardine run. *African Journal of Marine Science,* 32**,** 279-291.

OKE, P. R. & MIDDLETON, J. H. 2001. Nutrient enrichment off Port Stephens: the role of the East Australian Current. *Continental Shelf Research,* 21**,** 587-606.

OZAKI, K., UYE, S. I., KUSUMOTO, T. & HAGINO, T. 2004. Interannual variability of the ecosystem of the Kii Channel, the Inland Sea of Japan, as influenced by bottom intrusion of cold and nutrient-rich water from the Pacific Ocean, and a recent trend of warming and oligotrophication. *Fisheries Oceanography,* 13**,** 65-79.

PARSONS, T. R., TAKAHASHI, M. & HARGRAVE, B. 2013. *Biological oceanographic processes*, Elsevier.

PAWLOWICZ, R. 2010. What every oceanographer needs to know about TEOS-10 (The TEOS-10 Primer). *Unpublished manuscript. Available at www. TEOS-10. org*.

PAWLOWICZ, R. 2013. Key physical variables in the ocean: temperature, salinity, and density. *Nature Education Knowledge,* 4**,** 13.

PEARCE, A. 1977. Some features of the upper 500 m of the Agulhas Current. *Journal of Marine Research,* 34**,** 731-753.

PEARCE, A. 1978. Seasonal variations of temperature and salinity on the northern Natal continental shelf. *South African Geographical Journal,* 60**,** 135-143.

PIOLLÉ, J. F. & AUTRET, E. 2011. MyOcean Product User Manual For Level 3 and 4 ODYSSEA SST products over the global ocean and north western shelves. *MYO-MED-PUM-001-006-a-v2. 0.*

PIVAN, X., KRUG, M. & HERBETTE, S. 2016. Observations of the vertical and temporal evolution of a Natal Pulse along the Eastern Agulhas Bank. *Journal of Geophysical Research: Oceans,* 121**,** 7108-7122.

RIO, M., MULET, S. & PICOT, N. New global Mean Dynamic Topography from a GOCE geoid model, altimeter measurements and oceanographic in-situ data. Proceedings of the ESA living planet symposium, Edinburgh, 2013.

ROBERTS, M. J. 2010. Coastal currents and temperatures along the eastern region of Algoa Bay, South Africa, with implications for transport and shelf-bay water exchange. *African Journal of Marine Science,* 32**,** 145-161.

ROBERTS, M. J., NIEUWENHUYS, C. & GUASTELLA, L. A. 2016. Circulation of shelf waters in the KwaZulu-Natal Bight, South Africa. *African Journal of Marine Science,* 38**,** S7-S21.

ROBERTS, M. J., RIBBINK, A. J., MORRIS, T., VAN DEN BERG, M. A., ENGELBRECHT, D. C. & HARDING, R. T. 2006. Oceanographic environment of the Sodwana Bay coelacanths (Latimeria chalumnae), South Africa: coelacanth research. *South African Journal of Science,* 102**,** 435-443.

ROBERTS, M. J., VAN DER LINGEN, C. D., WHITTLE, C. & VAN DEN BERG, M. A. 2010. Shelf currents, lee-trapped and transient eddies on the inshore boundary of the Agulhas Current, South Africa: their relevance to the KwaZulu-Natal sardine run. *African Journal of Marine Science,* 32**,** 423-447.

ROUAULT, M. J., MOUCHE, A., COLLARD, F., JOHANNESSEN, J. A. & CHAPRON, B. 2010. Mapping the Agulhas Current from space: An assessment of ASAR surface current velocities. *Journal of Geophysical Research: Oceans,* 115**,** n/a-n/a.

ROUAULT, M. J. & PENVEN, P. 2011. New perspectives on Natal Pulses from satellite observations. *Journal of Geophysical Research: Oceans,* 116.

ROUGHAN, M., KEATING, S. R., SCHAEFFER, A., CETINA, H. P., ROCHA, C., GRIFFIN, D., ROBERTSON, R. & SUTHERS, C. I. M. 2017. A tale of two eddies: The biophysical characteristics of two contrasting cyclonic eddies in the East Australian Current System. *Journal of Geophysical Research: Oceans,* 122**,** 2494-2518.

ROUGHAN, M. & MIDDLETON, J. H. 2002. A comparison of observed upwelling mechanisms off the east coast of Australia. *Continental Shelf Research,* 22**,** 2551-2572.

ROYER, T. C. 1982. Coastal fresh water discharge in the northeast Pacific. *Journal of Geophysical Research: Oceans,* 87**,** 2017-2021.

SÆTRE, R. & DA SILVA, A. J. 1984. The circulation of the Mozambique Channel. *Deep Sea Research Part A. Oceanographic Research Papers,* 31**,** 485-508.

SCHAEFFER, A. & ROUGHAN, M. 2015. Influence of a western boundary current on shelf dynamics and upwelling from repeat glider deployments. *Geophysical Research Letters,* 42**,** 121-128.

SCHAEFFER, A., ROUGHAN, M. & MORRIS, B. D. 2013. Cross-shelf dynamics in a western boundary current regime: Implications for upwelling. *Journal of Physical Oceanography,* 43**,** 1042-1059.

SCHOUTEN, M. W., DE RUIJTER, W. P. M. & VAN LEEUWEN, P. J. 2002. Upstream control of Agulhas Ring shedding. *Journal of Geophysical Research: Oceans,* 107.

SCHUMANN, E. H. 1981. Low frequency fluctuations off the Natal coast. *Journal of Geophysical Research: Oceans,* 86**,** 6499-6508.

SCHUMANN, E. H. 1986. The bottom boundary layer inshore of the Agulhas Current off Natal in August 1975. *South African Journal of Marine Science,* 4**,** 93-102.

SCHUMANN, E. H. 1998. The coastal ocean off southeast Africa, including Madagascar. *The Sea,* 11**,** 557-581.

SCHUMANN, E. H. 1999. Wind-driven mixed layer and coastal upwelling processes off the south coast of South Africa. *Journal of Marine Research,* 57**,** 671-691.

SCHUMANN, E. H. 2013. Physical Oceanography Off Natal. *In:* SCHUMANN, E. (ed.) *Coastal Ocean Studies off Natal, South Africa.*

SCHUMANN, E. H. & BRINK, K. H. 1990. Coastal-trapped waves off the coast of South Africa: generation, propagation and current structures. *Journal of Physical Oceanography,* 20**,** 1206-1218.

SCHUMANN, E. H., PERRINS, L. A. & HUNTER, I. T. 1982. Upwelling along the south coast of the Cape Province, South Africa. *South African Journal of Science,* 78**,** 238-242.

SCHUMANN, E. H. & VAN HEERDEN, I. L. 1988. Observations of Agulhas Current frontal features south of Africa, October 1983. *Deep Sea Research Part A. Oceanographic Research Papers,* 35**,** 1355-1362.

SEA-BIRD SCIENTIFIC 2017. Software Manual - Seasoft V2: SBE Data Processing. Sea-Bird Scientific.

SEA-BIRD SCIENTIFIC. 2018. *SBE 911 plus CTD* [Online]. Available: http://www.seabird.com/sbe911plus-ctd [Accessed 19 March 2018].

SHILLINGTON, F. A., REASON, C. J. C., DUNCOMBE RAE, C. M., FLORENCHIE, P. & PENVEN, P. 2006. 4 Large scale physical variability of the Benguela Current Large Marine Ecosystem (BCLME). *Large Marine Ecosystems.* Elsevier.

SILULWANE, N. F., RICHARDSON, A. J., SHILLINGTON, F. A. & MITCHELL-INNES, B. A. 2001. Identification and classification of vertical chlorophyll patterns in the Benguela

upwelling system and Angola-Benguela front using an artificial neural network. *South African Journal of Marine Science,* 23**,** 37-51.

SIMPSON, J. 2012. *Introduction to the physical and biological oceanography of shelf seas,* Cambridge, Cambridge University Press.

SINK, K., HOLNESS, S., HARRIS, L., MAJIEDT, P., ATKINSON, L., ROBINSON, T., KIRKMAN, S., HUTCHINGS, L., LESLIE, R. & LAMBERTH, S. 2012. National biodiversity assessment 2011: Technical report. *Volume,* 4**,** 325.

SMITH, R. 1994. The physical processes of coastal ocean upwelling systems. *Upwelling in the ocean: Modern processes and ancient records***,** 39-64.

STEWART, R. H. 2008. *Introduction to physical oceanography*, Texas A & M University.

STRAMMA, L., JOHNSON, G. C., SPRINTALL, J. & MOHRHOLZ, V. 2008. Expanding Oxygen-Minimum Zones in the Tropical Oceans. *Science,* 320**,** 655-658.

TALJAARD, J. 1972. Synoptic meteorology of the Southern Hemisphere. *Meteorology of the Southern Hemisphere.* Springer.

TALLEY, L. D. 2013. *Hydrographic Atlas of the World Ocean Circulation Experiment (WOCE): Volume 4: Indian Ocean*, International WOCE Project Office.

TALLEY, L. D., PICKARD, G. L., EMERY, W. J. & SWIFT, J. H. 2011. *Descriptive Physical Oceanography: An Introduction*, Academic Press.

TONG, Y., ZHAO, Y., ZHEN, G., CHI, J., LIU, X., LU, Y., WANG, X., YAO, R., CHEN, J. & ZHANG, W. 2015. Nutrient Loads Flowing into Coastal Waters from the Main Rivers of China (2006–2012). *Scientific Reports,* 5**,** 16678.

TSUGAWA, M. & HASUMI, H. 2010. Generation and growth mechanism of the Natal Pulse. *Journal of Physical Oceanography,* 40**,** 1597-1612.

VAN DER LINGEN, C., COETZEE, J. & HUTCHINGS, L. 2010. Overview of the KwaZulu-Natal sardine run. *African Journal of Marine Science,* 32**,** 271-277.

VAN DER VAART, P. C. F. & DE RUIJTER, W. P. M. 2001. Stability of Western Boundary Currents with an Application to Pulselike Behavior of the Agulhas Current. *Journal of Physical Oceanography,* 31**,** 2625-2644.

VAN NIEKERK, L., LAMBERTH, S., HUIZINGA, P., LUCK-VOGEL, M., MEYER, A. A., PULFRICH, A., TALJAARD, S., THERON, A., VAN BALLEGOOYEN, R. C., HUTCHINGS, L. & LAMONT, T. 2013. Assessment of the role of freshwater inflows in the coastal marine ecosystem. *In:* VAN NIEKERK, L. & LAMBERTH, S. (eds.) *Estuary and Marine EFR assessment.* Pretoria, South Africa: UNDP-GEF.

VINAYACHANDRAN, P. N., JAHFER, S. & NANJUNDIAH, R. S. 2015. Impact of river runoff into the ocean on Indian summer monsoon. *Environmental Research Letters,* 10**,** 054008.

VOLPE, G., SANTOLERI, S. C., FORNERIS, V., BRANDO, V., GARNESSON, P., TAYLOR, B. & GRANT, M. 2017. PRODUCT USER MANUAL.

WELSCHMEYER, N., GOERICKE, R., STROM, S. & PETERSON, W. 1991. Phytoplankton growth and herbivory in the subarctic Pacific: A chemotaxonomic analysis. *Limnology and Oceanography,* 36**,** 1631-1649.

XING, J. & DAVIES, A. M. 2002. Influence of wind direction, wind waves, and density stratification upon sediment transport in shelf edge regions: The Iberian shelf. *Journal of Geophysical Research: Oceans,* 107.

ZUMA, J. 2014. *Address by His Excellency President Zuma. Operation Phakisa: Unlocking the Economic Potential of the Ocean Economy, Open Day* [Online]. International Convention Centre (ICC): The South African Government. Available: http://www.gov.za/speeches/view.php [Accessed 16 June 2018].

Appendices

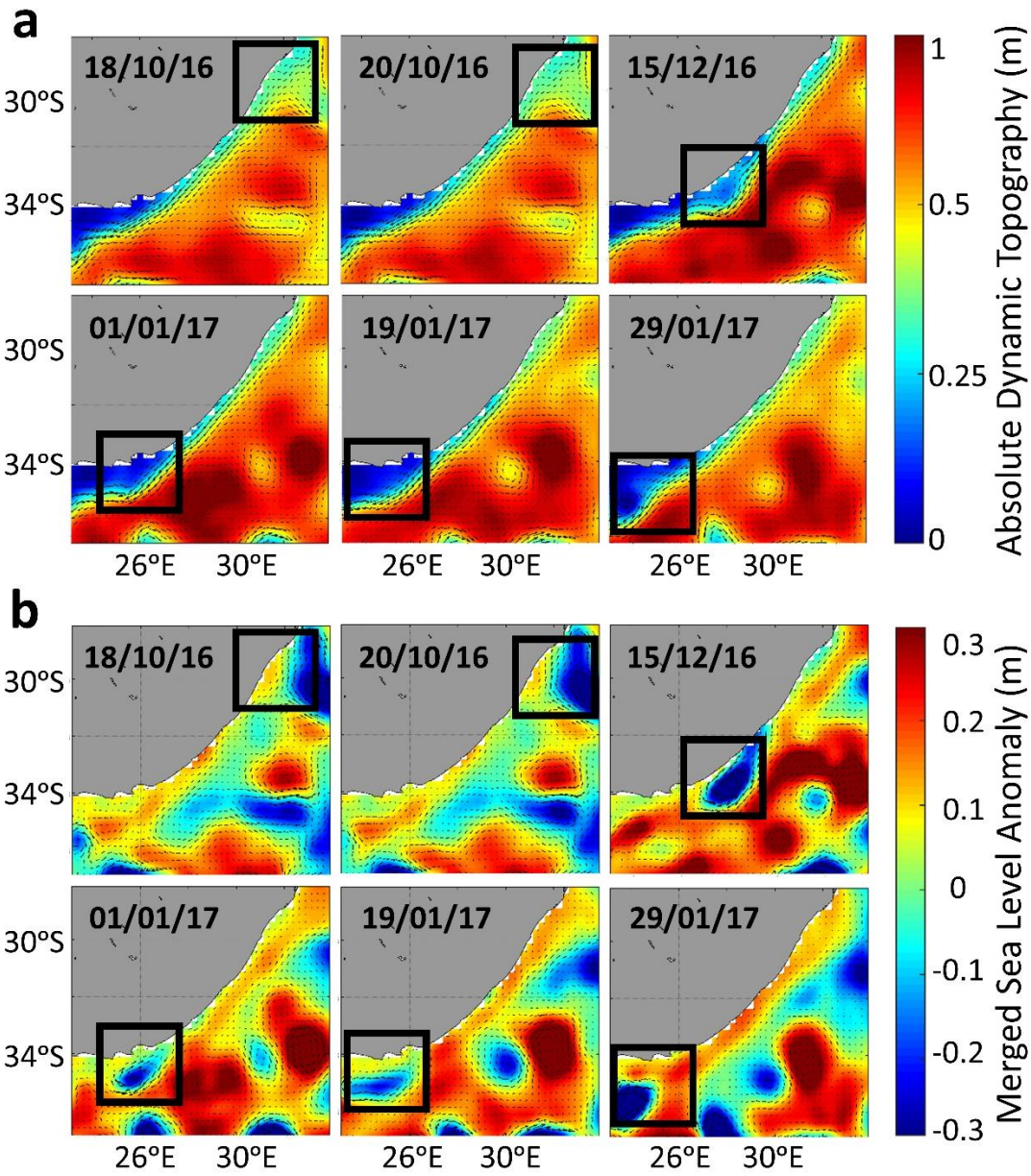

Figure A.1 Tracking of the January/February cyclonic eddy (highlighted in the black box) from the KwaZulu-Natal Bight to the location of sampling. a.) Time series of absolute dynamic topography depicting the meander caused by the cyclonic eddy. b.) Time series of sea level anomaly depicting the eddy.

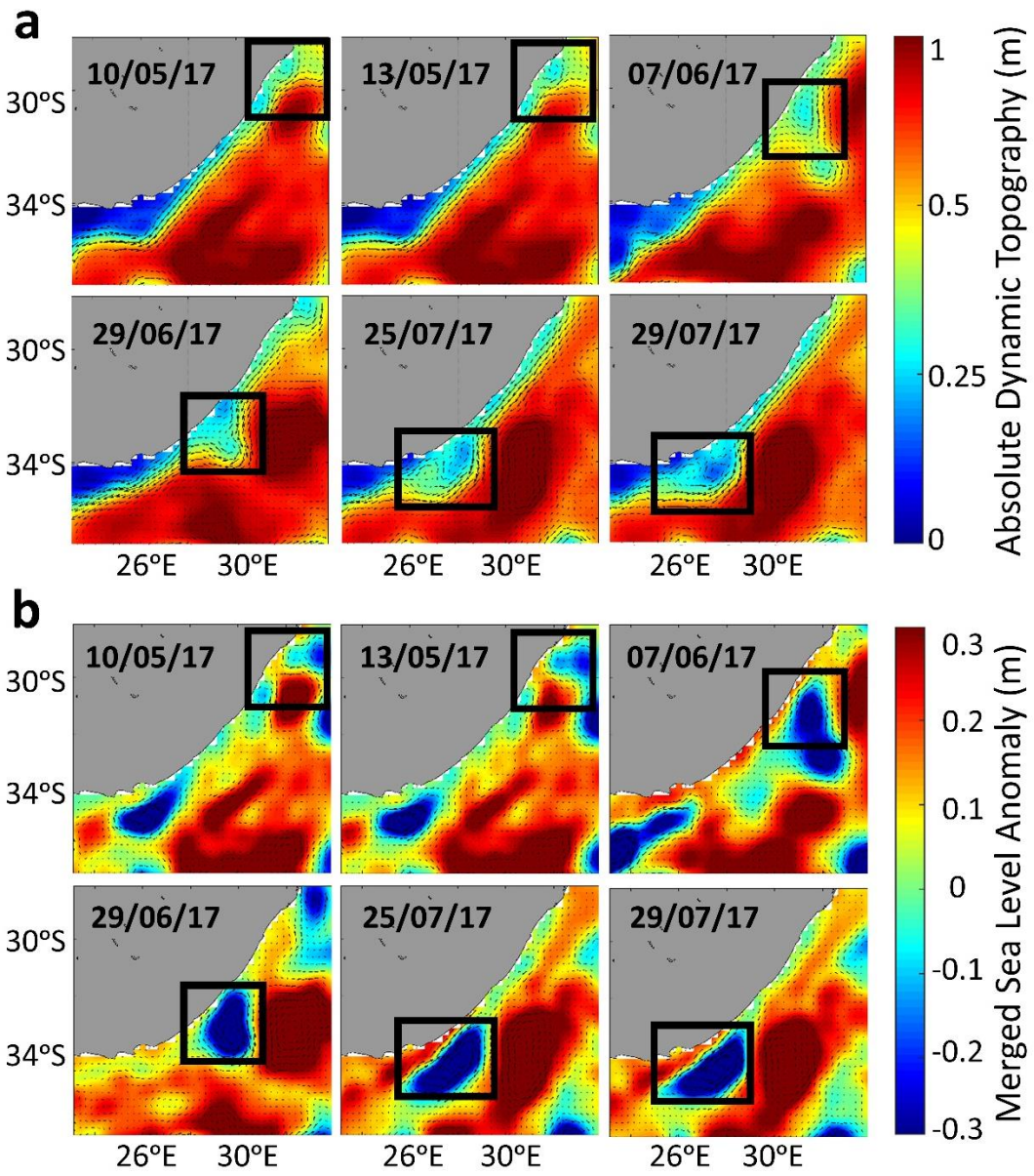

Figure A.2 Tracking of the July/August cyclonic eddy (highlighted in the black box) from the KwaZulu-Natal Bight to the location of sampling. a.) Time series of absolute dynamic topography depicting the meander caused by the cyclonic eddy. b.) Time series of sea level anomaly depicting the eddy.

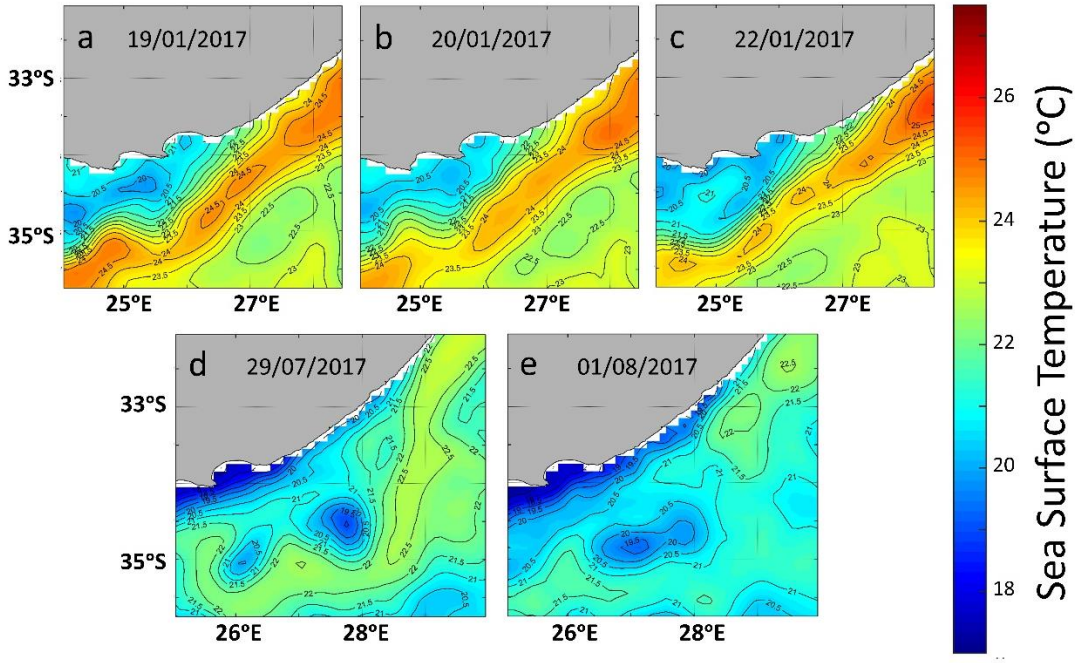

Figure A.3 Zoomed ODYSSEA sea surface temperature maps illustrating the ineffectiveness of the satellite data in capturing the low surface temperatures observed during the January/February and July/August 2017 cruises.

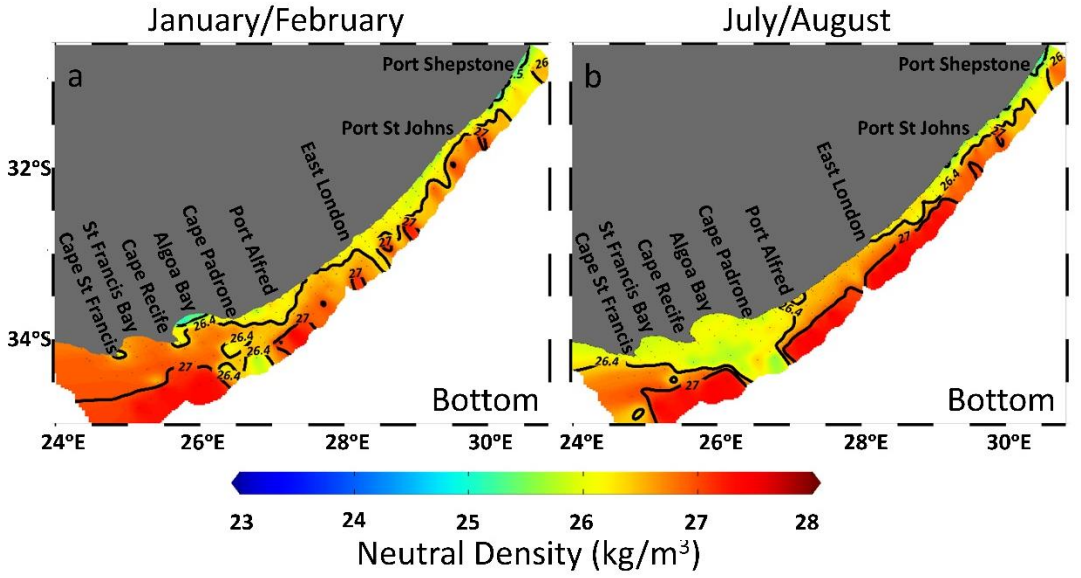

Figure A.4 Bottom neutral density maps for the a.) January/February and b.) July/August 2017 cruises, overlain with neutral density contours given by Beal et al. (2006) for Tropical and Subtropical Surface Water, South Indian Central Water, Red Sea Water and Antarctic Intermediate Water.

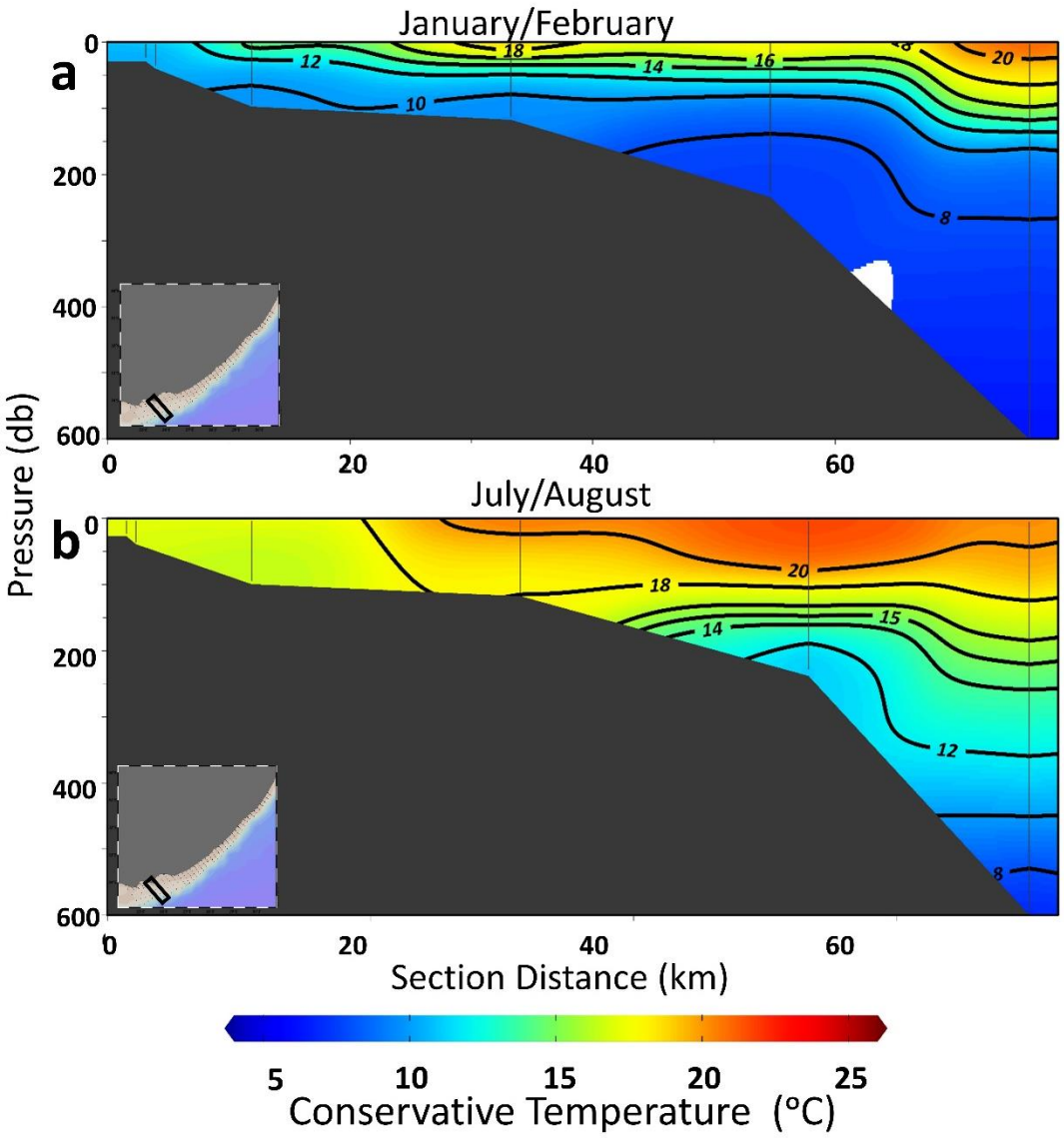

Figure A.5 Vertical cross-shelf temperatures sections for the transect off Cape Recife during the a.) January/February and b.) July/August 2017 cruise, highlighting the influence of Ekman pumping associated with the January/February cyclonic eddy as well as the state of the water column in July/August, in the absence of an eddy.

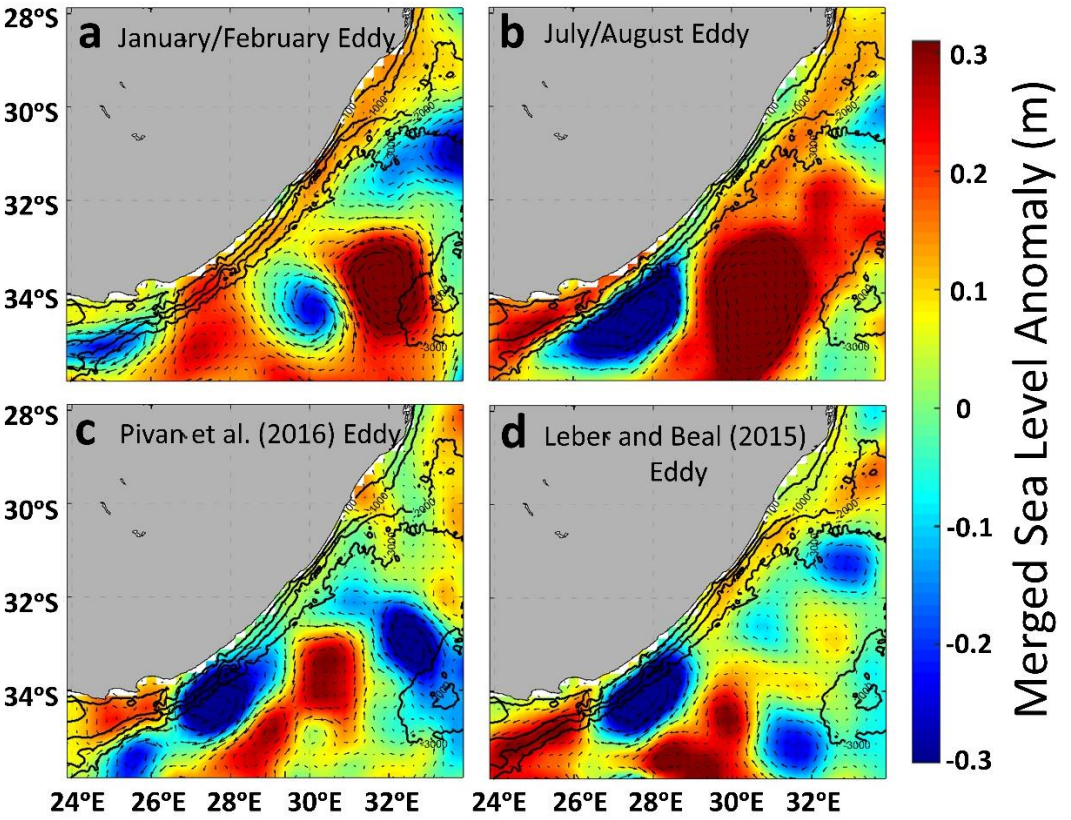

Figure A.6 AVISO altimetry data illustrating four different cyclonic eddies, represented by sea level anomaly maps overlain with geostrophic velocity anomaly vectors, as well as ETOPO2 bathymetric contours (100, 1000, 2000 and 3000 m). a.) January/February 2017 eddy, b.) July/August 2017 eddy, Pivan et al. (2016) eddy and d.) Leber and Beal (2015) eddy.

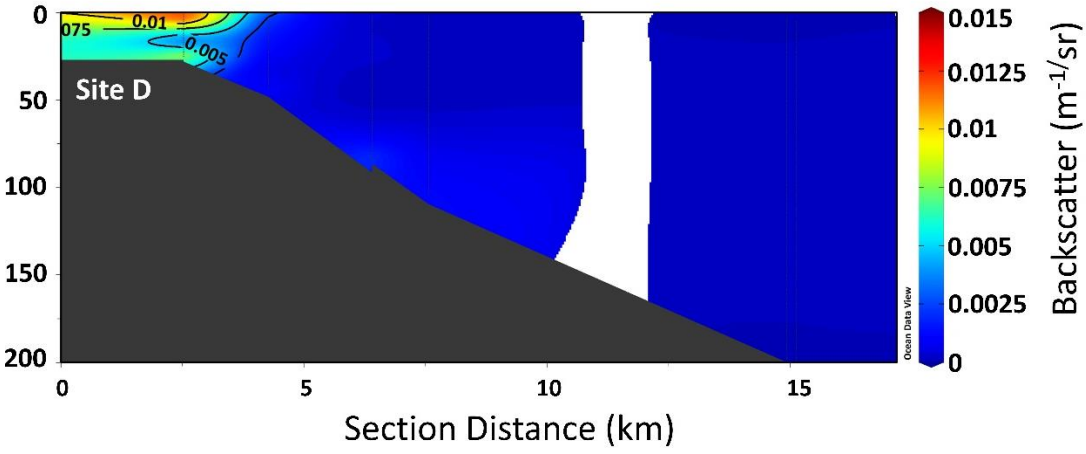

Figure A.7 Vertical cross-shelf backscatter section of the Mzimvubu River transect, highlighting high suspended sediment in the coastal waters near the Mzimvubu River mouth.

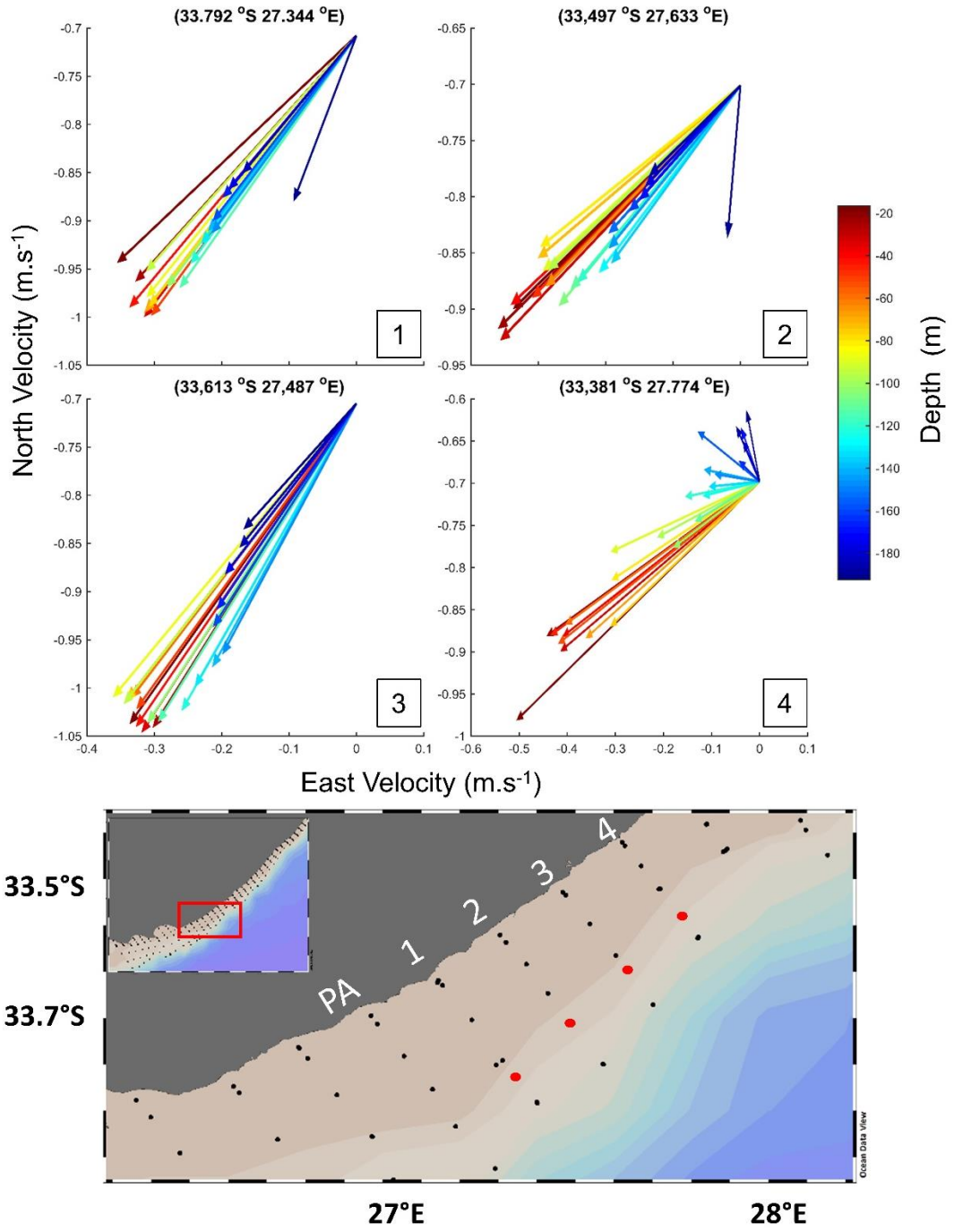

Figure A.8 Ekman veering in the bottom boundary layer, depicted by S-ADCP current spirals, from the surface to the bottom of the water column, at the stations positioned along the shelf break (depicted in red), at the four transects upstream of Port Alfred. The length of the arrows indicate the magnitude of the velocities, their orientation indicates their direction of flow in relation to a bearing (north is up) and the colours, indicated by the colour bar, represent their depth in the water column.